The Role of Chaos and Magnetic Fields in the Cosmic Ray Anisotropy

by

Vanessa López-Barquero

A dissertation submitted in partial fulfillment of

the requirements for the degree of

Doctor of Philosophy

(Physics)

at the

UNIVERSITY OF WISCONSIN–MADISON

2021

Date of final oral examination: 4/27/2021

The dissertation is approved by the following members of the Final Oral Committee:

Paolo Desiati, Senior Scientist, WIPAC
Francis Halzen, Professor, Physics
Amy Barger, Professor, Astronomy
Elena D'Onghia, Professor, Astronomy
Juan Carlos Díaz Vélez, Production Simulation Programmer, WIPAC

THE ROLE OF CHAOS AND MAGNETIC FIELDS IN THE
COSMIC RAY ANISOTROPY

Vanessa López-Barquero

Under the supervision of Doctor Paolo Desiati and Professor Francis Halzen

At the University of Wisconsin-Madison

Abstract

Cosmic rays are detected on Earth with an energy-dependent anisotropy in their arrival direction. Recent experimental results of this arrival distribution of high-energy cosmic rays (CRs) have motivated studies aimed at improving our understanding of the cosmic ray transport and their propagating media. This arrival distribution involves a convolution of the distribution of sources and the effects of the magnetic field properties through which particles propagate. Nonetheless, no comprehensive explanation has been put forth to date. Understanding what causes this cosmic-ray anisotropy and how we can use it to learn about the characteristics of the media they traverse are the central questions of this thesis.

More specifically, this dissertation will explore the effects of magnetic fields and various magnetic structures on the anisotropy of arriving CRs from TeV to PeV scales. These contributions can impact the largest angular scale to the medium- and small-scale angular structures. This investigation centers around the effects of three physical processes: one on the chaotic behavior in coherent magnetic structures, another one on magnetic turbulence, and a third on heliospheric effects

First, we detail the effects of chaos and trapping in coherent structures on the CR propagation. We apply a new method to characterize chaotic trajectories in bound systems. This method is based on the Finite-Time Lyapunov Exponent (FTLE), which determines the degree of chaos in the particles' trajectories. Furthermore, we model a coherent magnetic structure with time-perturbations that can be used to describe distinct magnetic systems and processes. Our results show that the FTLE, i.e., the level of chaos, is related to the CRs

escape time from the system by a power-law relation. Additionally, this power law persists even if perturbations act on the system, pointing to the idea that this specific power law could be an essential parameter of the system. We also find that CRs can be divided into different categories according to their chaotic behavior. Moreover, these categories are distributed in specific regions in the arrival distribution maps. This means that various regions on the map could develop differently from one to another in time. Therefore, this result can provide the basis for time-variability in the CR arrival direction maps.

We also discuss how turbulence in the interstellar medium can modify CR trajectories. To investigate this idea, we perform numerical integration of particle trajectories in compressible magnetohydrodynamic turbulence to study how the CRs arrival direction distribution is perturbed when streamed along the local turbulent magnetic field. We found that this inhomogeneous and turbulent interstellar magnetic field can imprint its structure on the CR maps.

Another aspect explored is the heliospheric influence on particles with rigidities in the range of 1-10 TV. We test if anisotropies may arise from the interaction with the heliosphere. We employed a magnetic field model of the heliosphere for this goal and performed forward-propagating numerical calculations of particle trajectories. Our results show that the heliosphere can strongly redistribute the particles' directions, making it an indispensable component for the anisotropy.

Finally, through these magnetic structures and mechanisms, we can learn about how CRs propagate and their arrival distribution. However, these particles can also act as probes for the properties of the different media they traverse and their places of origin. Therefore, the study of cosmic rays opens multiple doors for a better understanding of the universe.

A mi familia.

"I would venture to guess that Anon, who wrote so many poems without signing them, was often a woman."

— Virginia Woolf, *A Room of One's Own*

Acknowledgments

First and foremost, I am deeply grateful to Paolo Desiati. He never failed to help and encourage me. Paolo, you are a fantastic person and a true example of how people in academia should be. I would also like to acknowledge my gratitude to Francis Halzen. His support has been instrumental during my time in graduate school. He is a role model for being an outstanding scholar and a great human being.

I would like to thank my thesis committee members, Juan Carlos Díaz-Vélez, Amy Barger, and Elena D'Onghia. Amy and Elena are amazing and an inspiration for women in science. Juan Carlos, I have truly enjoyed the time that we have worked together, and I will never forget all the Kanopy shows. I would also like to thank my collaborators, especially Nikolai Pogorelov for his help during the postdoc application process.

The friendships I made in the physics department have been essential to me all these years, and I cherish them deeply. Mohamed Abou Dbai, you have always been there for me since my first semester in Madison. I treasure your advice immensely. Your perseverance is genuinely inspirational. Emily Lichko, you are an exceptional physicist and someone I know I can trust forever. Erin Middlemas, thank you for always being a great friend and reminding me that we need to fight for women in STEM. James Sebald, thanks for all your advice and for being a true friend to me over the years. Obioma Ohia, you are one of the nicest people I know, and I value your kindness tremendously. I would like to thank Diptaranjan Das, Justin Walker, Andrew Loveridge, and Achim Stoessl for their precious friendships.

I would also like to thank my amazing Madison friends: Becca Meldman, Austin Hannah, Nadya Ponce, and Estrella Chávez. You have made my time in Madison one that is memorable,

and I value you and your friendships deeply. Becca, thank you for sharing your incredible perspective on life with me; I know your students have the best teacher ever. Austin, you are one of the funniest people I know. I cannot tell you how much I have enjoyed our conversations, lunches, and Terrace time. Special thanks to the Mediterranean Café, and Fice in particular. You have made me feel like family, and your food has fueled most, if not all, of these thesis chapters.

A very special thanks to my UCR amigos: Lizdenia Arce, Rafael Oreamuno, Ireth García, and Mónica Sánchez. Particularly for all your feedback on my work and support for more than a decade now. Thank you for all the help these past months, Grupo de Estudio!

I would also like to extend my gratitude to my best friends: Monserrat Monge, Alejandro Madrigal, and Melvin Agüero. Monse, you are the best friend one can have. We have grown so much, and even though we are still trying to figure out who we are, I know that you will always be there with me. Ale, you have been my unconditional friend since my first year as a physics student. You have been with me in all my academic and personal journeys. I cannot imagine where life will take us, but I know we will continue to support each other's dreams. Mel, thank you for your friendship. You always know what advice to give me. I admire your perspective on life and the happiness that you always transmit to me. More than friends, you guys are family to me.

Quiero agradecer a las personas más importantes de mi vida: Ivonne Barquero, Marco Vinicio López and José Pablo López Barquero. Ma, Pa, y Jose, gracias por su apoyo incondicional. Les dedico esta tesis a ustedes.

Definitions and Abbreviations

CRA   Cosmic-Ray Anisotropy - measured anisotropy in the arrival direction distribution of cosmic rays at Earth.

ISM   Interstellar Medium

MHD   Magnetohydrodynamics - a fluid model description of plasma dynamics.

Table of Contents

List of Figures

Chapter 1

Introduction

What are cosmic rays? What is the cosmic ray
anisotropy?

Cosmic rays are particles that are accelerated to the highest energies found in the Universe. The study of cosmic rays is fundamental to understanding various environments at a wide range of scales. These scales could range from the heliosphere's size to the interstellar medium and even Mpc dimensions in clusters of galaxies. Cosmic rays are also involved in crucial processes, such as the death of stars, energy injection into the Galaxy, or turbulence.

The most critical characteristic of cosmic rays that we will be exploiting in this work is that they are charged particles[1]. Consequently, they interact with magnetic fields. Here, we will explore how magnetic fields in the Galaxy and basic magnetic processes can alter how cosmic rays arrive at the Earth.

Cosmic rays with energies between TeV and PeV have their origin in the Galaxy. Therefore, we can use them as a vessel for collecting information about these sources. Furthermore, we can gain vital knowledge about the environment they traverse before being detected on Earth. This latter idea is what sparked the motivation for this thesis. We will explore the different components that can affect cosmic rays and how they can help us understand CR

---

[1]It is important to note that there are multiple definitions of what cosmic rays are. We will use in this thesis the more restricted definition of them as "charged particles" instead of the broader one of solely "relativistic particles."

propagation. Specifically, we will ground these efforts in building a comprehensive picture of the cosmic ray anisotropy observed on Earth.

Galactic cosmic rays display an anisotropy in their arrival direction. This anisotropy has a relative intensity on the order of 10^{-3}. It also has a rich angular structure, with high multipole moments bearing power. On this basis, we can make a distinction between large-scale and small-scale anisotropy. Another essential characteristic is that this arrival distribution is energy dependent. Later, we will see that these components will be crucial when finding answers to why this anisotropy exists.

In the quest for a complete understanding of CRs, we consider questions on their energy spectrum, composition, propagation, and-the essential aspect for this thesis-their arrival-direction distribution. These different aspects are all interconnected. Therefore, we need to link all the pieces of this non-linear puzzle to have a comprehensive perspective on the problem at hand.

This thesis details the contributions that magnetic fields and various magnetic structures can have on CR propagation and the repercussions on their subsequent detection. Specifically, we will study the effects of turbulent magnetic fields in the interstellar medium, the heliospheric system, particle trapping, and chaos. The most important results of this thesis are: (1) magnetic fields are crucial to the study of CR anisotropy, (2) the heliosphere can modify the overall CR distribution for particles between 1 TV and 10 TV, (3) turbulent magnetic fields in the ISM can imprint their structure in the CR arrival direction maps, (4) the chaotic behavior of trapped cosmic rays can cause significant variation in the CR arrival maps.

1.1   Overview of the Work Presented in this Thesis

Chapter 2 will go through the basic concepts related to cosmic rays. We will talk about the different mysteries surrounding CRs, such as their composition, origin, and propagation. We will also discuss the observed CR anisotropy. Chapter 3 will be devoted to the study of the chaotic behavior of trapped cosmic rays. In Chapter 4, we will discuss how the heliosphere

plays a role in the cosmic ray anisotropy. Chapter 5 will detail the influence of the local interstellar medium. Finally, in Chapter 6, we will present our conclusions, outlook, and future work. Chapter 7 is dedicated to a summary of this dissertation tailored to the general public. Its aim is to explain the research in this thesis to a non-specialist audience.

Chapter 2

Background

What are the mysteries behind cosmic rays? How do cosmic rays
propagate throughout the Galaxy?

This chapter introduces the basic concepts that we will use throughout the subsequent chapters. The main objective is to establish the different observable quantities and mechanisms that will be explored later. First we introduce the history and the main questions surrounding cosmic rays.

2.1 Cosmic Rays and Their Fundamental Questions

Between the years 1911 and 1912, Victor Hess conducted a series of experiments in balloon flights (see Figure 7.1). Initially, he climbed to 1000 meters and measured the radiation using an electroscope. Hess noticed no relevant changes in the levels there compared to the ground level. Later, in 1912, he rose to altitudes of 5000 meters. He did those ascents at night and also during an almost total solar eclipse to avoid having his results affected by the Sun. He noticed, at first, that the ionization decreased as the altitude increased, but then, the ionization started increasing. Therefore, he concluded that the radiation must be coming from a source other than the Earth–a cosmic origin. This simple yet significant observation

would become the beginning of the study of cosmic rays. [1]
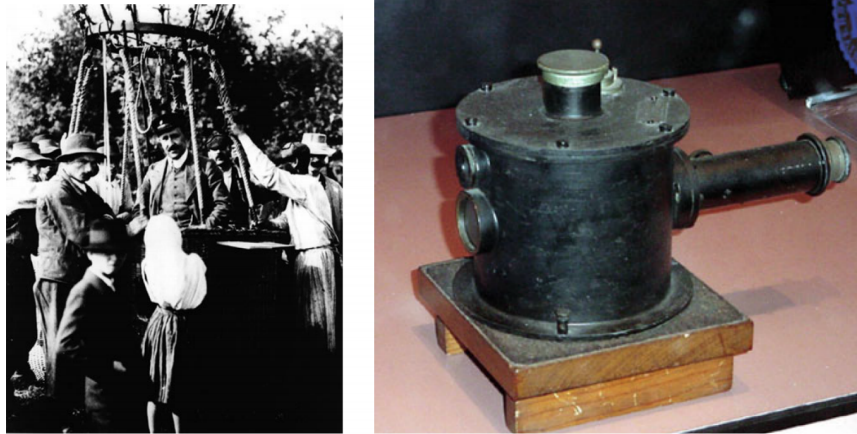
Figure 2.1: Left: Canonical photo of Victor Hess' balloon flight. Right: Electrometer used by Hess (Smithsonian National Air and Science Museum). Photos taken from: A. De Angelis and C. Arcaro b. Schultz, 2018 [4].

2.1.1 Definition, Composition, and Spectrum

Cosmic rays are mainly protons, helium, heavy nuclei, and electrons accelerated to high energies. At the high end, they have been measured at more than 10^{20} eV. Initially, it was thought that cosmic rays were a form of electromagnetic radiation; that is why their name is a misnomer. Nonetheless, their exact composition varies depending on energy, as we can see in Fig. 2.2 [5]. In this work, we will focus on the particles with energies between TeV and PeV. We can see that protons are the principal component in that range, but then helium and heavier elements, such as carbon and oxygen, obtain prevalence in the flux at higher energies.[2]

An overview of the energy spectrum is given in Fig. 2.3. This spectrum is almost a perfect power law that spans more than twelve orders of magnitude. The overall index for the power law is approximately 2.8. There is basic terminology that is used to describe certain

---

[1]Victor Hess published his results in the *Physikalische Zeitschrift* [1, 2, 3]. Translation to English and historical commentary by A. De Angelis and C. Arcaro b. Schultz [4].

[2]In Chapter 4, this distribution will become central to our discussion of the observed anisotropy in the arrival distribution of cosmic rays at rigidities between 1 TV and 10 TV.
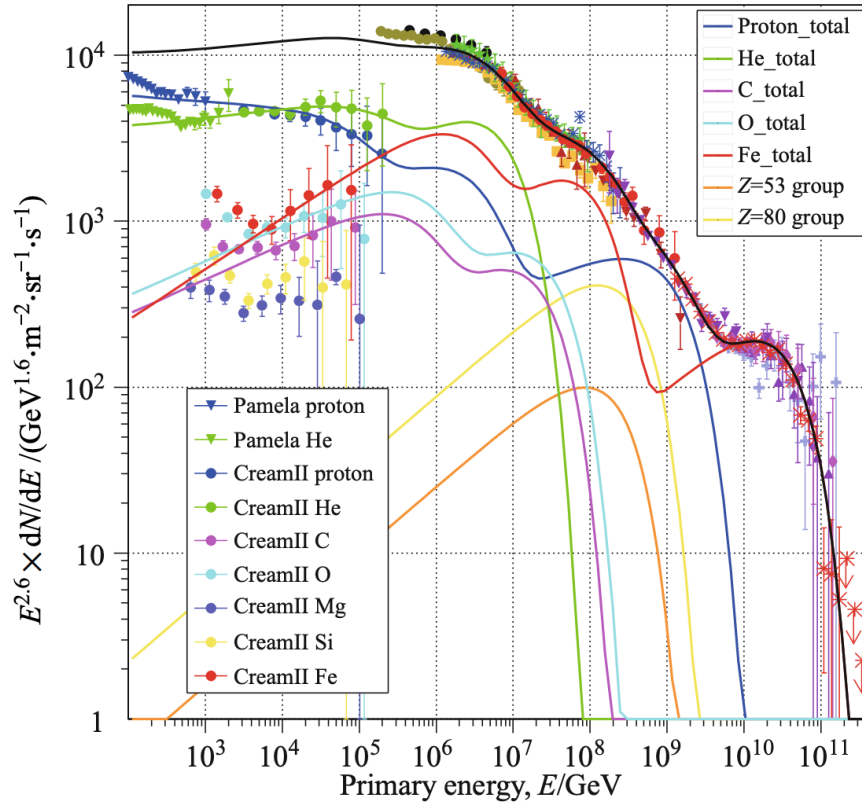
Figure 2.2: Overview of the cosmic ray composition according to their energy (Gaisser et al. [5]). It plots flux (defined as the flux of particles reaching the Earth per unit time, surface and solid angle) against primary energy. Note that protons are dominant at lower energies, although, at higher energies, a shift to heavier elements is observed.

features of the spectrum. The areas where the slope changes slightly are referred to as the knee and the ankle. The knee occupies a span around 10^{15} eV and the ankle around 10^{18} eV. Where the knee is located, there is a steepening of the slope. This feature is most likely because supernovae are limited in the acceleration of particles at those energies and chemical composition cutoffs [6][3]. On the other hand, in the ankle, we can observe a small flattening of the spectrum, which points to a possible transition to extragalactic sources.

Cosmic rays can be classified based on their origin: solar, galactic, or extragalactic. The transition between galactic and extragalactic CRs is expected to be in the interval between 10^{17} and 10^{19} eV. We will be working with galactic CRs in the upcoming chapters. At the

---

[3]This is a simplified explanation to a possibly very complex phenomena. There could be a rare type of source that accelerates particles and another reason for the existence of the knee can arise.
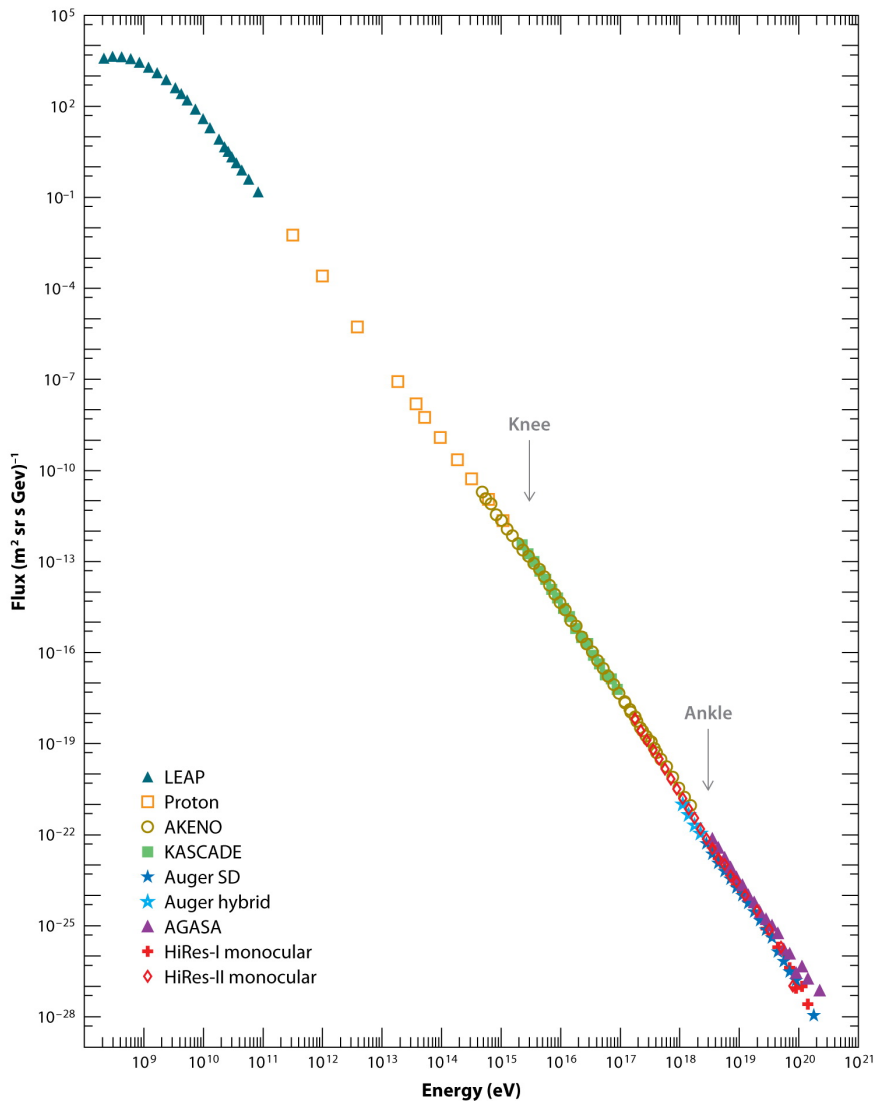
Figure 2.3: Overview of the cosmic ray spectrum. (J. Beatty & S. Westerhoff (2009) [12]). Note that the knee is located at PeV energies and the ankle at 10^{18} eV.

moment, an exact place of origin for these CRs has not been pinpointed; however, there are staple candidates that are able to accelerate particles to these energies in the Galaxy. Supernova remnants are without doubt the perfect site for CR acceleration [6][4]. This evidence is circumstantial but has been confirmed by different independent methods [8, 9, 10, 11].

---

[4]Supernovae as sources of cosmic rays were first discussed by Baade and Zwicky in 1934. [7]

2.2 Propagation of Cosmic Rays

Cosmic rays are extraterrestrial charged particles. This aspect opens the door to focusing our attention on their propagation and, in particular, the dynamics and electromagnetic interactions that they experience in the process. One of the challenges concerning this problem and its captivating argument is that, since cosmic rays interact with different media in the galaxy, a multidisciplinary approach should be taken to provide a satisfactory description.

One major topic that we will consider in this thesis is how magnetic fields in the local interstellar medium affect the propagation of cosmic rays. For that reason, two key concepts to explore are turbulence and chaos.

Turbulence is everywhere in the Galaxy, and it permeates multiple scales and processes. Among these processes are the creation of structures in the ISM and CR acceleration and transport. Therefore, we need to understand how it works and the exact repercussions that it could have in a system. Unfortunately[5], "turbulence" is still an open question. The majority of astrophysical plasmas are highly ionized and possess high Reynolds numbers[6], which indicates that nonlinear mechanisms are responsible for the dynamics of the flow. Given these conditions, turbulence arises. The influence of turbulence on CR propagation is through the stochastic nature of magnetic field lines. In this case, the spatial distribution of CRs is affected by the turbulent magnetic fields within the mean free path.

2.3 Cosmic Ray Anisotropy

As we mentioned in the previous chapter, when Galactic cosmic rays arrive at Earth, they do so in an anisotropic manner. This anisotropy has an amplitude on the order of 10^{-3}. An exact explanation for this anisotropy still eludes us. However, it is expected that the origin is due to a synthesis of factors such as the distribution and nature of sources, properties of

---

[5]Or perhaps, fortunately, since it is an intriguing problem.

[6]The Reynolds number is defined as $R_e = VL/\nu$, where V is the speed of the flow, L the characteristic length, and ν the viscosity.

the magnetic fields, and overall cosmic-ray propagation. Nonetheless, from this anisotropy, we can distill crucial information about the propagation of CRs in nearby magnetic fields.

Figure 2.4 shows an all-sky map of the anisotropy at median energy of 10 TeV from the HAWC and IceCube observatories[7]. In this figure, the relative intensity of cosmic rays is plotted as a function of the arrival direction on Earth. The red color indicates that the relative intensity is higher than the all-sky mean intensity. On the other hand, the blue color denotes a lower relative intensity. This figure has the large-scale distribution in the top panel and small scales in the bottom panel. The residual map in panel B represents a subtraction of the dipole, quadrupole, and octupole from panel A, and therefore shows the structure that is obscured in the overall map. The angular power spectrum in Figure 2.5 is a spherical harmonic decomposition of the all-sky map. It shows how much power each harmonic l has. Consequently, this angular power spectrum constitutes a tool for calculating the importance of structures at various angular scales.

Another relevant characteristic of these observations is that the CR arrival distribution varies depending on the particles' energy. We can see this feature in Fig. 2.6. The anisotropy distribution changes drastically in its morphology at 13 TeV compared to 1.4 PeV. This property is a clear indication that different mechanisms and structures are at play when dealing with cosmic rays arriving at Earth. For instance, it could transition from the effects of specific magnetic structures to other ones within the last mean free path or even a dominant local sources.

In the following chapters, we will explore different explanations for this anisotropy, which will shine a light on specific mechanisms behind the behavior of CRs with energies between 1 TeV and 30 PeV. More generally, we will also examine magnetic processes that apply from microscales to intercluster dimensions.

---

[7]The HAWC observatory is located in the Northern Hemisphere at a latitude of 19°N. The IceCube observatory is in the Southern Hemisphere at a latitude of 90°S.
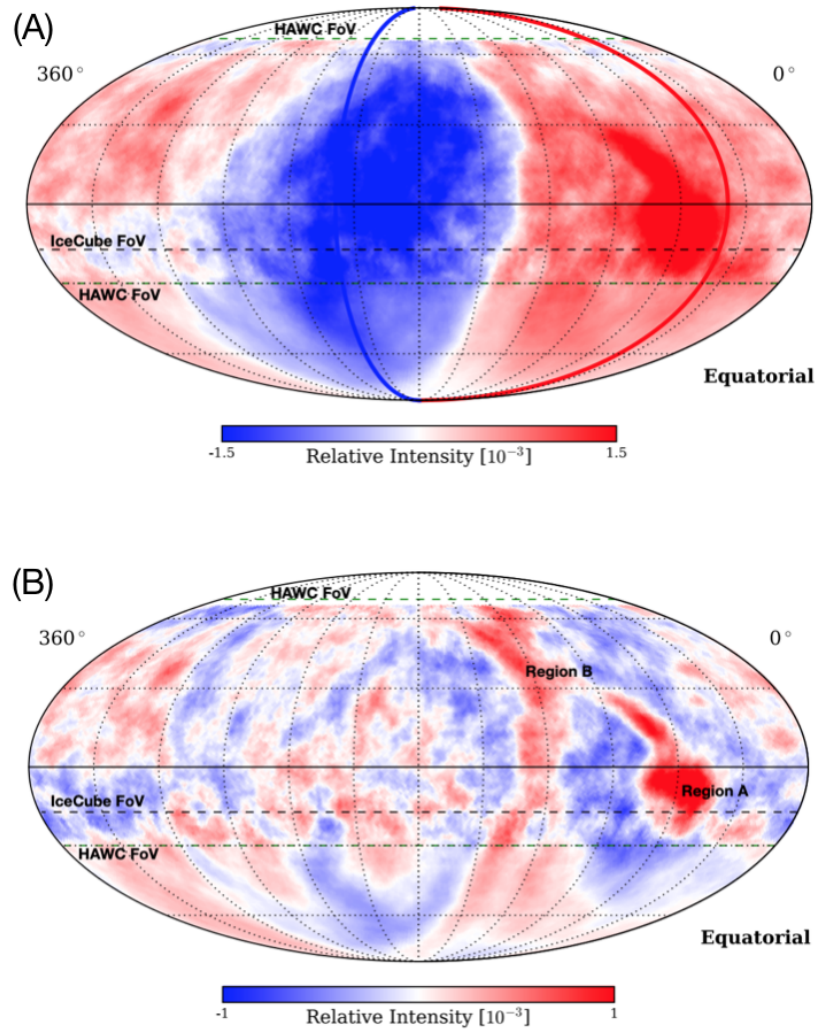
Figure 2.4: All-Sky anisotropy of cosmic rays at 10 TeV. (Abeysekara et al.(2019) [13]). Mollweide projection sky maps of relative intensity of cosmic rays at 10 TeV median energy. Panel A: Large-scale map. Panel B: Small-scale map after subtracting the fitted multipole from the spherical harmonic expansion with $l \leqslant 3$ from the large-scale map. Data by the High-Altitude Water Cherenkov and IceCube observatories in the Northern and Southern Hemispheres
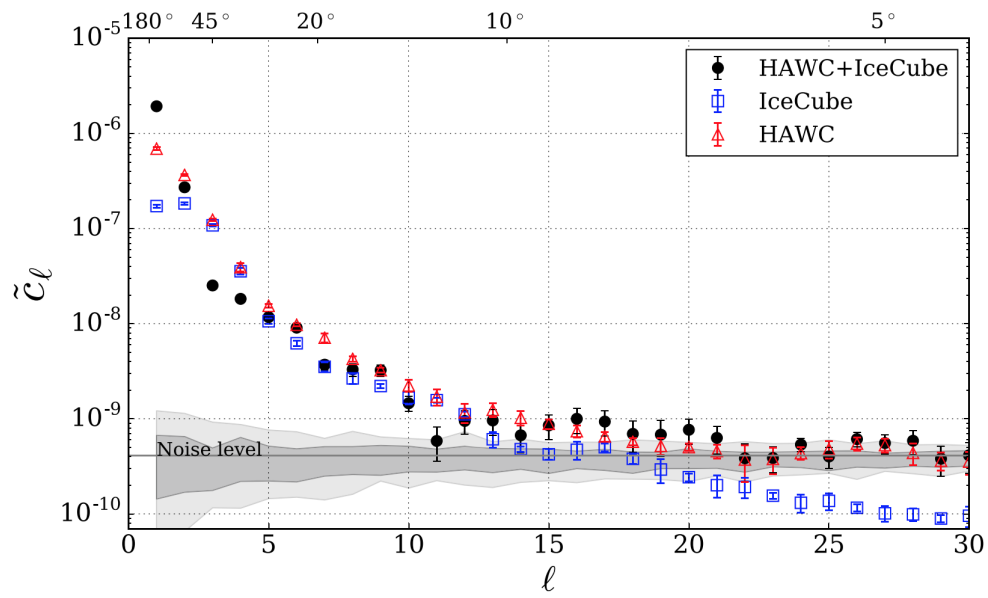
Figure 2.5: Angular power spectrum of the cosmic ray anisotropy at 10 TeV. (Abeysekara et al.(2019) [13]). The black dots represent the HAWC and IceCube data combined. The blue squares: IceCube. Red triangles: HAWC. The gray band shows the 90% confidence level around the level of statistical fluctuations for isotropic maps.
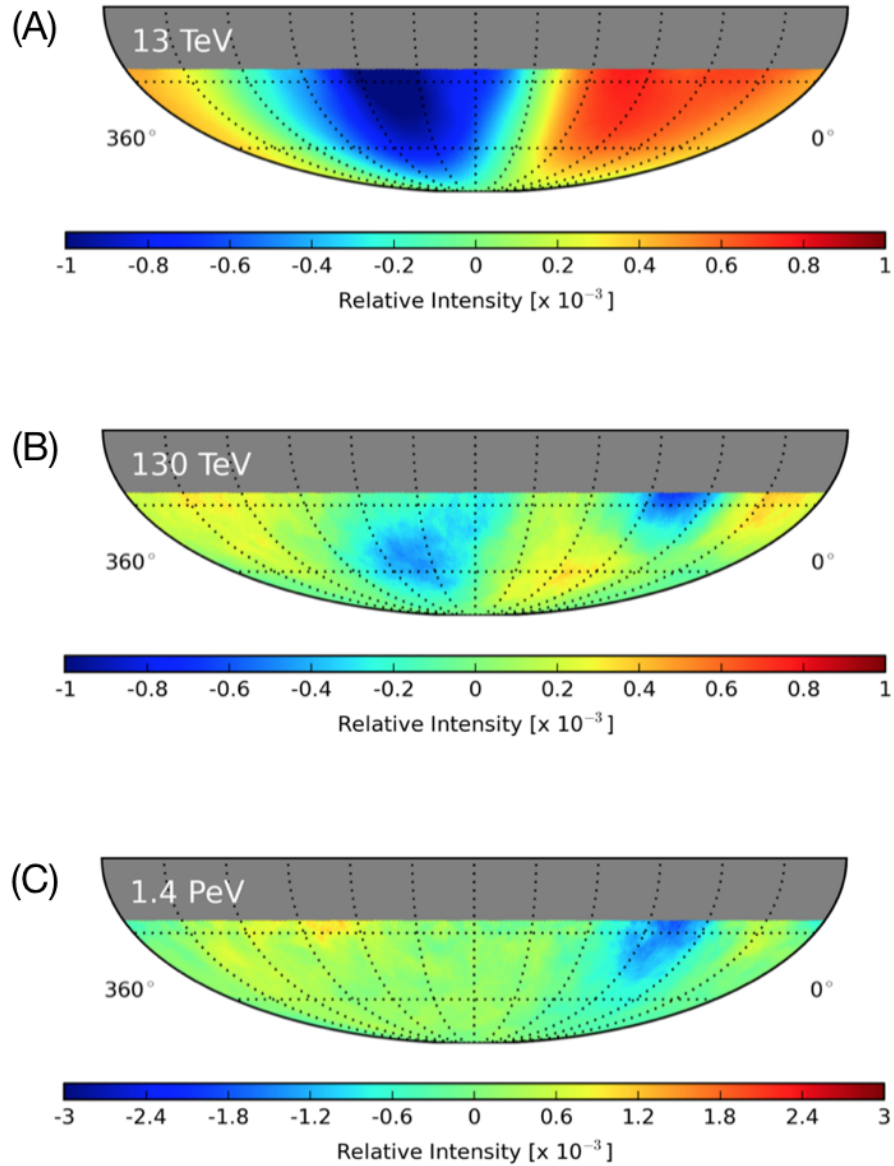
Figure 2.6: Maps of relative intensity in equatorial coordinates for different energy bins (Aartsen et al.(2016) [14]). IceCube data. Panel A: Median energy 13 TeV. Panel B: 130 TeV. Panel C: 1.4 PeV.

Bibliography

[1] V. Hess, Phys. Zeit. 13 (1912) 1084

[2] V. Hess, Phys. Zeit. 12 (1911) 998

[3] V. Hess, Phys. Zeit. 14 (1913) 612

[4] Hess, V. 2018, arXiv:1808.02927

[5] Gaisser, T. K., Stanev, T., & Tilav, S. 2013, Frontiers of Physics, 8, 748. doi:10.1007/s11467-013-0319-7

[6] Blasi, P. 2013, A& A Rev., 21, 70. doi:10.1007/s00159-013-0070-7

[7] Baade, W. & Zwicky, F. 1934, Physical Review, 46, 76. doi:10.1103/PhysRev.46.76.2

[8] Ackermann, M., Ajello, M., Allafort, A., et al. 2013, Science, 339, 807. doi:10.1126/science.1231160

[9] Giordano, F., Naumann-Godo, M., Ballet, J., et al. 2012, ApJL, 744, L2. doi:10.1088/2041-8205/744/1/L2

[10] Berezhko, E. G., Ksenofontov, L. T., & Völk, H. J. 2013, ApJ, 763, 14. doi:10.1088/0004-637X/763/1/14

[11] Vink, J. 2012, A& A Rev., 20, 49. doi:10.1007/s00159-011-0049-1

[12] Beatty, J., & Westerhoff, S. Annual Review of Nuclear and Particle Science 2009 59:1, 319-345

[13] Abeysekara, A. U., Alfaro, R., Alvarez, C., et al. 2019, ApJ, 871, 96. doi:10.3847/1538-4357/aaf5cc

[14] Aartsen, M. G., Abraham, K., Ackermann, M., et al. 2016, ApJ, 826, 220. doi:10.3847/0004-637X/826/2/220

Chapter 3

Chaotic Behavior of Trapped Cosmic Rays

How does the chaotic behavior of trapped cosmic rays affect the CR anisotropy?

Recent experimental results on the arrival direction distribution of high-energy cosmic rays have motivated studies aimed at improving our understanding of the environment through which they propagate. The observed anisotropy of these cosmic rays is intrinsically coupled with their origin, as their source distribution may provide the initial density gradient. However, the interstellar magnetic fields are responsible for the actual arrival distribution shape. In any coherent magnetic structure, such as the heliosphere or the Local Bubble, magnetic mirroring may cause trapping of particles, which may lead to their chaotic behavior. Mirroring can occur in magnetohydrodynamic turbulence as well, where subsequent trapping and release within local magnetic cells affect particles' large-scale diffusion properties. Even in an ideal magnetic system and in the absence of chaotic magnetic field lines, a break of an adiabatic invariant leads to chaos. This chapter will explore a method that we develop to characterize cosmic rays' chaotic behavior in magnetic systems based on the Finite-Time Lyapunov Exponents, used to quantify the degree of chaos. We study particle trajectory behavior in an ideal axial-symmetric magnetic bottle to highlight the basic properties of mirroring effects.

In order to study the dependency of external influences on chaotic behavior, we introduce time-dependent magnetic perturbations. We found that the Finite-Time Lyapunov exponent is correlated to the particles' escape time from the system. This relation is given by a power law that persists even if additional perturbations act on it. This specific power law could prove to be an intrinsic characteristic of the system. The maps of arrival distribution in these systems display areas where the chaotic characteristics vary significantly. This work lays down the framework that will be used to study the effects of magnetic mirroring of TeV cosmic rays within the heliosphere and the role that time variability induced by solar cycles may have on the anisotropy observed on Earth.

3.1   Introduction

The origin of the cosmic ray anisotropy observed over a wide range of energies [1, 2] is still largely unknown. However, it is likely caused by a combination of factors. These factors include the spatial distribution of sources of cosmic rays in the Galaxy and the complex geometry and properties of the magnetic fields through which particles propagate. The processes shaping the distribution of cosmic rays are interconnected. Therefore, it is not trivial to unfold them [21].

It has been speculated that the observed cosmic ray anisotropy in the 1-10 TV rigidity range may be explained in the context of homogeneous and uniform diffusion in the interstellar medium (ISM) [32, 21, 67, 66, 77, 72]. Nearby and recent sources are more likely to shape the cosmic rays' arrival direction distribution on Earth. On the other hand, the nonuniform pitch-angle distribution of the cosmic rays [31, 60] in magnetohydrodynamic (MHD) turbulence [39] and the heterogeneous nature of the ISM affect the diffusion significantly in time and space. Therefore, the standard diffusion scenario cannot explain the complex angular structure of the observed anisotropy. Besides, nondiffusive stochastic scattering processes within the mean free path are likely to play an important role [39, 10, 11, 85]. The presence of coherent magnetic structures, such as superbubbles, magnetized clouds, or the heliosphere, can also

cause a significant redistribution of the particle arrival directions.

From a dimensional standpoint, cosmic rays with rigidity of $\sim$10 TV have a gyroradius of about $R_L \sim$500–800 AU in a 3–5 μG magnetic field, which is comparable to the transverse size of the heliosphere [94]. In fact, while low-rigidity cosmic rays are influenced by the inner heliospheric structure, 10 TV scale particles are shaped by the boundary region with the ISM [28, 75, 82, 59].

Therefore, it is evident that to determine the cosmic rays' distribution in the interstellar medium, it is necessary to account for the heliospheric influence [82, 20, 21]. Currently, we seem to know more about the inner heliosphere, while little is understood about the interface between the solar wind and the local ISM. Various questions arise: how wide and long is the heliosphere? Are the flanks characterized by magnetic instabilities? Does turbulence play a relevant role? Therefore, a careful analysis of experimental observations, along with the most up-to-date heliosphere models, may help account for the heliospheric effects on arriving cosmic rays. The recent full-sky combined observation of the 10-TeV cosmic ray anisotropy by the HAWC gamma-ray and the IceCube neutrino observatories [1] provides the first view of TeV cosmic ray anisotropy with minimal experimental bias [20].

In López-Barquero et al. (2017) [59], protons, helium, and iron nuclei trajectories between 1 TV and 10 TV were numerically integrated in a heliospheric magnetic field model by [94]. There is no turbulence or stochastic magnetic field in the model. However, despite that, the initial uniform arrival direction distribution from the local interstellar magnetic field is broken down into medium and small angular scales by the effects of the heliospheric magnetic bubble. The corresponding angular power spectrum is not different from that generated by scattering processes off compressible MHD turbulence [85]. It turns out that cosmic ray particles with rigidities of 1–10 TV may be temporarily trapped in the magnetic mirror formed by the interstellar magnetic fieldlines draping around the heliosphere flanks.

Magnetic mirrors are present in a vast variety of astrophysical environments over a wide range of scales. Besides the heliosphere, coherent magnetic structures such as planetary magnetospheres, the Local Bubble, superbubbles, and likely galactic halos have a strong

influence in trapping and redistributing cosmic rays. Spatial magnetic field intermittency, which plays a role in the formation of coherent structures [32, 31] and is involved in the transport and acceleration of charged particles, is consequently an important candidate to study when dealing with magnetic-bottle structures. Cosmic ray trapping in localized magnetic cells, or mirrors, may significantly contribute to the energy dependency of the diffusion coefficient. In particular, compressible modes in MHD turbulence generate the conditions for trapping cosmic ray particles, which leads to smaller and weaker energy dependency of diffusion parallel to the magnetic fieldlines [22].

To study the fundamental processes occurring when particles are trapped in a magnetic mirror, we employ an idealized toy magnetic field system represented by an axially symmetric magnetic bottle (see Section 3.2). Although this is an idealized system, it is known to cause complex particle trajectory topologies, and it serves the purpose of studying their properties. Particles may be permanently trapped within the magnetic bottle as long as their gyration frequency around magnetic field lines is sufficiently higher than the bouncing frequency between the mirror points. In such conditions, the magnetic field acting on particles does not significantly change within each gyration period. In other words, the motion is "adiabatic." As soon as magnetic variations over each gyro-period start to become significant, the adiabatic limit breaks down and the particles' motion becomes increasingly complex. Trajectories may develop chaotic behavior, meaning that their deterministic geometry strongly depends on the initial conditions. All trajectories are deterministic and can be exactly determined as long as all aspects of the magnetic system as well as the particles' coordinates are known with infinite accuracy. Even the slightest amount of inaccuracy makes any trajectory prediction impossible. Chaotic trajectories with similar initial conditions diverge from each other to very different trajectories. The rate of divergence depends on the actual initial conditions and the magnetic system, which determines the dynamic conditions to which trajectories are subjected. The degree to which similar trajectories diverge from each other can be assessed using the Lyapunov exponents. The variability of such exponents in the particles' phase space highlights the global properties of how a chaotic system is structured, and it may provide
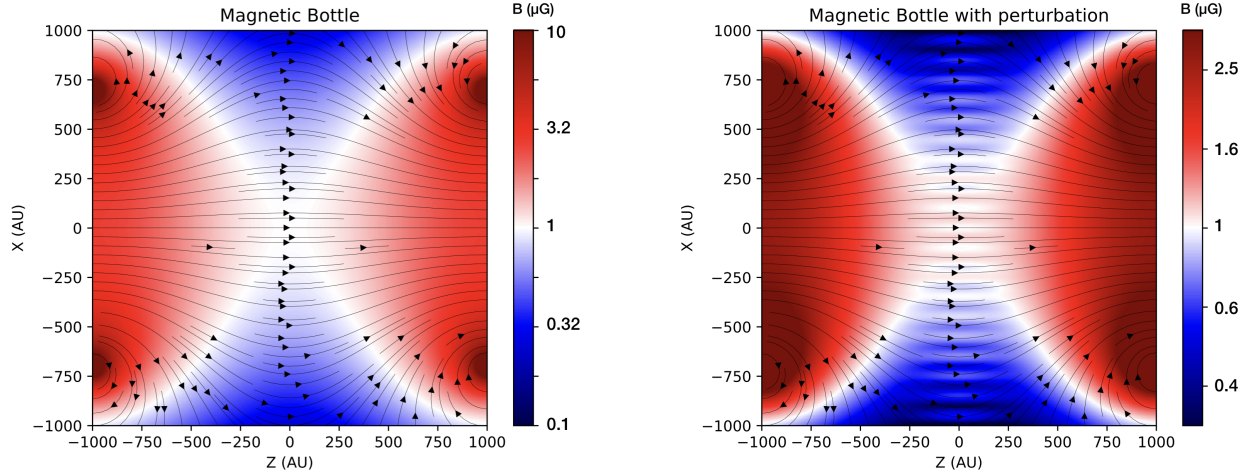
Figure 3.1: The magnetic bottle field geometry used as toy model to study the behavior of particles trapped by the interstellar magnetic field draping around the heliosphere. On the left, the static magnetic field and on the right, with the additional perturbation imitating the effects of solar cycles on the heliospheric magnetic field along its tail.

hints toward understanding how cosmic ray particles' arrival direction distribution on Earth is influenced by the heliosphere.

In Section 3.2, we present the physical contexts where the studies of particles in a magnetic bottle are laid down. Section 3.3 describes how particle trajectories are numerically calculated. Section 3.4 introduces the aspects about chaos theory that are relevant for this work, with Section 3.4.1 describing the Lyapunov exponents as an estimate of the degree of chaos in a system. Results are presented in Section 3.6 and discussed in Section 3.7. The outlook is given in Section 3.8, and conclusions in Section 3.9.

3.2 The Magnetic Bottle Field

An axial-symmetric magnetic bottle is used as a toy model to study how cosmic rays are trapped and under which conditions their trajectories' chaotic behavior arises and develops. This artificial magnetic field is generated by two circular coils with electric currents running in the same direction. Although the purpose of using this toy model goes beyond the investigation of TeV cosmic rays in the heliosphere, we tailor the study on this system and

Table 3.1: Parameters for the Magnetic Bottle

Radius (R)	700 AU
Current (I)	4×10^{10} A
Distance (D)	2000 AU
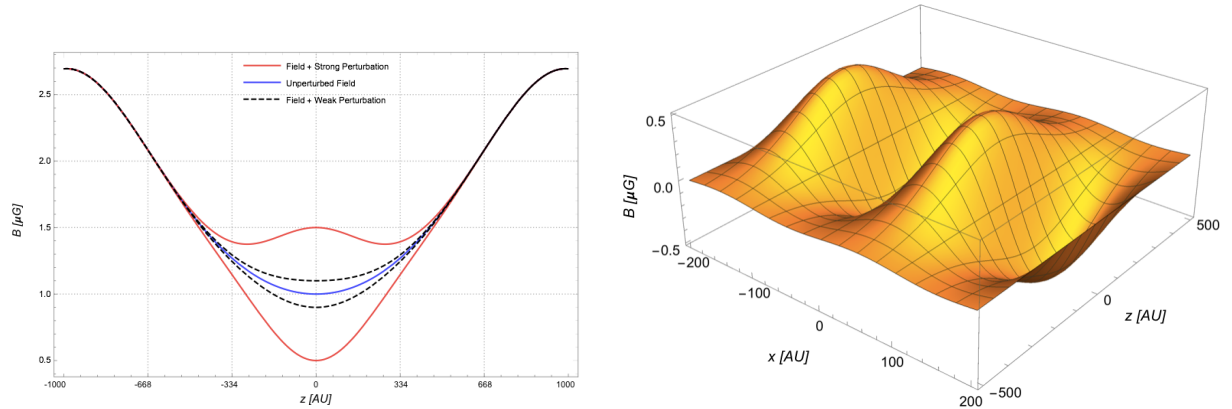
Figure 3.2: On the left, the field profile along the axis of the magnetic bottle with the *weak* and *strong* perturbations at their maximum amplitude. On the right, the 3D view of a snapshot of the magnetic perturbation.

assume that its spatial scale is comparable with the approximate size of the heliosphere. In this regard, we pick the distance between the coils as 2000 AU, which is the scale at which the local interstellar magnetic field lines drape around the heliosphere [94]. The coils' radius and currents are selected so that the magnetic field is approximately 3 μG at the center of each coil (corresponding to the mirror points of the magnetic bottle) and the lowest possible at the center between the two coils. Such a condition is satisfied with the geometric parameters listed in Table 3.1. With these parameters, the magnetic field is about 2.7 μG at the center of the coils and about 1 μG at the point between the coils. A cross section representation of the resulting field is shown on the left in Figure 3.1, where the magnetic field intensity is shown in color scale and the magnetic field line shows the shape of the magnetic bottle.

With the heliospheric system as inspiration, we introduce time modulations that mimic the effects of magnetic field reversals induced by the 11-year solar cycles. To do so in our toy model, we add a time-dependent component propagating transversely through the magnetic bottle (along the x-axis) with periodic modulations along the y-axis and a Gaussian

Table 3.2: Parameters for the Time-Perturbation

	Weak	Weak + E	Strong
$\frac{\Delta B}{B}$ (μG)	0.1	0.1	0.5
v_p (AU/yr)	2	2	20

dependency along the magnetic bottle axis (the z-axis) so that the largest perturbation is located at the center of the magnetic system. Such magnetic perturbation, shown on the right of Figure 3.1, is represented by the function

$$B_y = \frac{\Delta B}{B} \, \sin(k_p x - \omega_p t) \, e^{-\frac{1}{2}\left(\frac{z}{\sigma_p}\right)^2}, \tag{3.1}$$

where $k_p = \frac{2\pi}{L_p}$ and $\omega = \frac{2\pi v_p}{L_p}$ with $L_p = 200$ AU the spatial scale of the magnetic polarity regions, $\sigma = 200$ AU the width of the Gaussian modulation of the perturbation (see Figure 3.2). The relative amplitude $\frac{\Delta B}{B}$ and velocity v_p depend on the strength and type of magnetic perturbation, as shown in Table 3.2. The *weak* perturbation approximately represents the variability of solar wind properties along the heliosphere beyond the termination shock (see [24]). The parameters for the *strong* perturbation are chosen to amplify the effects of magnetic field time-modulations on the properties of particle trajectories.

When a magnetic field changes in time, an induced electric field $\boldsymbol{E} = -\boldsymbol{v} \times \boldsymbol{B}$ is produced. However, in plasmas, the induced electric fields are typically very small because the high conductivity makes it possible for electric charges to rearrange and screen electric fields over distances larger than the Debye length. The Debye length is the distance over which the screening caused by the collective charge rearrangement is effective, and shielding can occur only if the Debye length is much larger than the average distance of particles in the plasma. The heliospheric plasma has a wide variability of its properties, and it is difficult to pinpoint specific numbers that represent the global heliospheric behavior. In this work, we assume the extreme scenario where electric fields induced by the *weak* magnetic perturbations are not screened. With the parameters described in Table 3.2, the magnitude of the force produced by the electric field compared to the one from the magnetic field is approximately three

orders of magnitude smaller. Consequently, no significant effects from the electric field's presence are expected. The possibility for the occurrence of electric fields and its effects on the observed anisotropy is also studied in [26].

3.3   Calculating particle trajectories

Particle trajectories are calculated by numerically integrating the equation of motion

$$
\begin{cases}
\frac{d\boldsymbol{p}}{dt} = q\left(\boldsymbol{E} + \frac{\boldsymbol{v}\times\boldsymbol{B}}{c}\right) \\
\frac{d\boldsymbol{x}}{dt} = \boldsymbol{v}
\end{cases}, \tag{3.2}
$$

describing the force exerted by an electric field $\boldsymbol{E}$ and magnetic field $\boldsymbol{B}$ on a particle with velocity $\boldsymbol{v}$ and momentum $\boldsymbol{p}$. Like in Desiati & Zweibel (2014) [29], a dimensionless version of Eq. (3.2) is used in this work, where we introduce a magnetic field scale B_0,

$$
\begin{cases}
\frac{d\hat{\boldsymbol{p}}}{ds} = \hat{\boldsymbol{E}} + \frac{\hat{\boldsymbol{p}}}{\gamma} \times \hat{\boldsymbol{B}} \\
\frac{d\hat{\boldsymbol{x}}}{ds} = \frac{\hat{\boldsymbol{p}}}{\gamma}.
\end{cases}, \tag{3.3}
$$

where $\hat{\boldsymbol{B}} \equiv \boldsymbol{B}/B_0$ and $\hat{\boldsymbol{E}} \equiv \boldsymbol{E}/cB_0$ are the normalized magnetic and electric fields, respectively, and $\omega_0 \equiv eB_0/m_p$ is the proton gyro-frequency scale, which defines the dimensionless time $\hat{t} \equiv \omega_0 t$. The gyroradius scale $r_0 \equiv c/\omega_0$ defines the dimensionless spatial coordinates $\hat{\boldsymbol{x}} \equiv \boldsymbol{x}/r_0$, while the dimensionless momentum is defined as $\hat{\boldsymbol{p}} \equiv \boldsymbol{p}/mc$. The particle velocity $\boldsymbol{v}$ is related to $\hat{\boldsymbol{p}}$ by $\boldsymbol{v} = \hat{\boldsymbol{p}}/\gamma$ and its Lorentz factor $\gamma = \sqrt{1 + \hat{p}^2}$. In these units, the dimensionless particle gyroradius is $\hat{r}_g = \hat{p}_\perp$, and the dimensionless gyro-frequency is $\hat{\omega}_g = 1/\gamma$. Normalized variables are written with hats.

The Eqs. (3.3) are numerically solved using the fourth order Runge-Kutta integration method, with an adaptive time step size algorithm that keeps relative truncation errors within a tolerance level of $\epsilon = 10^{-10}$ (see Desiati & Zweibel 2014 [29] for more discussion on numerical accuracy). The maximum integration time used in this work was set to $\hat{t}_{max} = 10^8$

in code units (corresponding to about 10^{10} seconds, or 330 years). Under these conditions, the accuracy of the numerical integration is sufficient and does not affect the results. The magnetic field configurations described in Section 3.2 are used to calculate antiproton trajectories propagating back in time from their final location, at coordinates $(\hat{x}_0, \hat{y}_0, \hat{z}_0) = (100, 100, 500)$ in code units, away from the symmetry point of the magnetic system geometry. Integration stops either when integration time reaches the maximum value of $\hat{t}_{max} = 10^8$ or when the trajectories cross a sphere centered on $(\hat{x}, \hat{y}, \hat{z}) = (0, 0, 0)$ with radius $r_{max} = 12500$ in code units, corresponding to 2500 AU. Four sets of trajectories were calculated: one with the static magnetic bottle configuration shown on the left of Figure 3.1, one with the addition of the *weak* magnetic perturbation of Eq. 3.1, one with the *strong* magnetic perturbation, and the last using the weak magnetic field perturbation and the induced electric field $\boldsymbol{E} = -\boldsymbol{v}_p \times \boldsymbol{B}$. For each set, a total of 768 antiproton trajectories were integrated, with momentum vector direction corresponding to each pixel in a HealPix grid [43] with $nside = 8$.

To study the onset of chaotic behavior, i.e., how trajectories with infinitesimally close initial conditions diverge from each other, we produce, for each of the 768 *reference* trajectories of the four sets, ten additional sets of trajectories with the same initial momentum and with initial position randomly distributed around $(\hat{x}_0, \hat{y}_0, \hat{z}_0) = (100, 100, 500)$ on a sphere of radius $\hat{r}_0 = 0.01$.

3.4 Chaotic Trajectories

All physical systems that are conservative can be described as Hamiltonian systems, where the total energy and phase-space volume are conserved. One of the properties of Hamiltonian systems is that their state is governed by deterministic laws that can be highly sensitive to initial conditions, which is what defines chaotic systems. Even the smallest differences in the initial conditions, whether they originate from measurement uncertainties or from rounding errors of numerical calculations, may lead to vastly different trajectories. The limited knowledge of the properties of a physical system, in addition to experimental or

numerical resolution and accuracy, makes long-term prediction of its state evolution generally impossible, despite their deterministic nature. In a chaotic system, for an arbitrarily small solid angle in the sky, the origin of the particles coming from it can be highly uncertain and unpredictable. In the classical approximation, chaos can explain the origin and mechanisms of apparently stochastic processes, and this deterministic randomness can occur even in a very limited number of degrees of freedom.

A known chaotic system is the axis-symmetric magnetic bottle [38, 39]. Particles trapped in a magnetic bottle are characterized by their gyration frequency around the magnetic fieldlines and their bouncing frequency between the mirror points. As long as gyration frequency is sufficiently higher than bouncing frequency, the magnetic force on the particles changes very slowly within each gyration. In this condition, the magnetic moment $\mu = \frac{1}{2}\frac{p_\perp^2}{B}$ is an approximate constant of motion. In the limit of perfect conservation of the magnetic moment (also known as first adiabatic invariant), particles are indefinitely trapped inside the magnetic bottle and bounce back and forth between the mirror points. In reality, since the the adiabatic invariant is never exact in a realistic magnetic field system, after a sufficient time, particles eventually escape from the system. When the gyration and bouncing frequencies, which slowly drift from their initial values, assume comparable values, the changes in the magnetic field during one gyration may no longer be negligible and the adiabatic condition may be violated. Particles with very close but separate trajectories in phase-space experience different magnetic forces that eventually pull them apart. Under certain conditions, the rate of separations of similar trajectories can be significant so that they continue to develop with very different topologies before escaping the system. When this happens, trajectories manifest a typical chaotic behavior, which determines how long it takes before particles escape.

3.4.1 Lyapunov Exponents

One way to characterize chaotic trajectories is through the Lyapunov exponents (LE) [33, 34, 35, 36]. As particles with an initial separation propagate, they will start to get farther apart,

closer together, or remain at a constant separation; therefore, the LE will quantify the rate of divergence or convergence of the trajectories. If δZ_0 is the initial separation and $\delta Z(t)$ is the separation at time t, these two quantities can be related by the expression

$$|\delta Z(t)| \approx e^{\lambda t} |\delta Z_0| , \tag{3.4}$$

where λ is the Lyapunov exponent. Accordingly, a negative LE indicates convergence and a positive one, divergent trajectories and possibly chaos.

The number of Lyapunov exponents in the spectrum will depend on the dimensionality of the phase space. The largest exponent is referred to as the maximal Lyapunov exponent (MLE). This exponent will eventually dominate over the others due to exponential growth. Typically, the MLE is used to describe the trajectories since it is relatively simple to calculate from a time series and information can be obtained readily from it. The MLE can be expressed as

$$\lambda = \lim_{t \to \infty} \lim_{\delta Z_0 \to 0} \frac{1}{t} \ln \frac{|\delta Z(t)|}{|\delta Z_0|}, \tag{3.5}$$

where effectively the initial separation is made as small as possible and an asymptotic behavior is sought taking the limit of t to infinity.

However, problems arise when we look for such asymptotic behavior, since a trajectory may never achieve it, e.g., if the particle moves from one environment to another in a short time or it gets affected by different first-order mechanisms on its way. One way to alleviate this problem is to use the finite-time Lyapunov exponent (FTLE). Through the FTLE, a finite-time interval can be used to calculate the divergence in the trajectories without the necessity of an infinite limit.

The FTLE expression is given by

$$\lambda(t, \Delta t) = \frac{1}{\Delta t} \ln \left[\frac{d(t + \Delta t)}{d(t)} \right], \tag{3.6}$$

where Δt is the time interval for the calculation. The value for Δt is chosen depending on the intrinsic characteristics of the system and the particles traveling through it. Therefore, it is flexible and can be adapted to different scenarios.

In this work, we are dealing with a bounded system; therefore, it is imperative to use a quantity that will quantify chaos under such conditions. Since an asymptotic behavior is not achieved for particles that remain in the system for a period of time before escaping, the FTLE can adjust and describe their behavior while bounded in the system, given that an appropriate Δt is chosen.

3.5 Methodology

We introduce our reference particles starting at the point $(x_o, y_o, z_o) = (100, 100, 500)$ and with initial momentum in the direction of the 768 pixels in the map, which correspond to each pixel in the HealPix grid [43] with $nside = 8$. For each reference particle, we have a set of 10 particles that are injected randomly on a sphere of radius $\hat{r}_0 = 0.01$. The final time for the family of particles per reference particle is defined as the shortest final time for a specific particle. At each time step, the distance in phase space is calculated between each particle and the reference, given by the expression

$$d_j^2(t) = \sum_{i=1}^{3} (x_i^{ref} - x_i)^2 + (p_i^{ref} - p_i)^2. \tag{3.7}$$

With all the distances calculated, we proceed to the calculation of the finite-time Lyapunov exponent, given by the expression

$$\lambda_j = \frac{1}{\Delta T} \ln \left[\frac{d(t_j + \Delta T)}{d(t_j)} \right]. \tag{3.8}$$

The value for ΔT should be chosen depending on the characteristics of the system; for example, in this case, the bouncing time between mirrors gives us a point of reference for the value of ΔT. Also, ΔT should capture the specific features of the divergence, as shown in
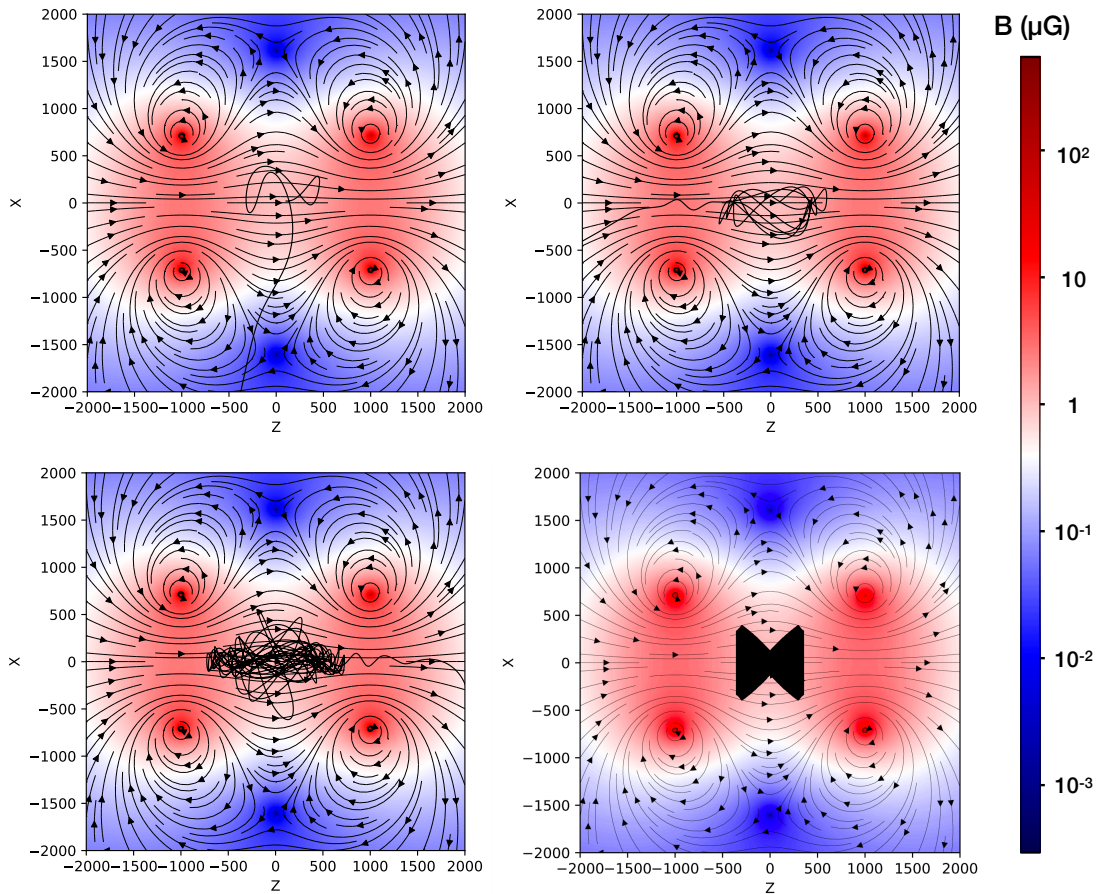
Figure 3.3: Trajectories in the unperturbed system. *Top Left*: Transient particle with a final time of 33000. *Top Right*: Intermediate particle with a final time of 75402. *Bottom Left*: Irregular particle in the power-law behavior section with a final time of 295366. *Bottom Right*: Trapped particle with the maximum integration time.

panels (a) and (d) in Figure 3.4. Here, the average value taken for ΔT is 38100 in normalized units.

Once the FTLE has been calculated for each pair of particles at each time step t_j, we proceed to calculate the average for the family of particles at each time step. Therefore, we obtain a $\bar{\lambda}$ for each time step:

$$\bar{\lambda}_j^F = \frac{1}{n} \sum_{i=1}^{n} \lambda_{ij}, \tag{3.9}$$

with n as the number of particles in the family for each reference particles; in our case, n=10.

Then, a histogram is generated with all the obtained values of λ. Panels (c) and (f) in Figure 3.4 show in light blue an example of an obtained distribution. Given that a value of λ_{FTLE} equal to zero means no divergence and that a positive value indicates divergence, we then proceed to fit two Gaussians for each distribution. As we can see from our two examples, there is a peak of the distribution around zero and another peak at a higher value. Therefore, we fit these two scenarios with the peaks of our two Gaussians. Since the second peak represents the actual divergence of the trajectories, we take this value to represent the value assigned to λ_{FTLE} for each specific family of particles.

3.6   Results

This section shows the results obtained with the numerical calculation and methodology described in Sections 3.3 and 3.5, respectively. Based on those, it is found that there is a correlation between the finite-time Lyapunov exponent (FTLE), i.e., the chaotic behavior of the set of particles, and the escape time from the system (see Fig. 3.5). This correlation follows a specific power law that persists even if perturbations are introduced in the system (see Figs. 3.6 and 3.7). If the FTLEs and escape times are plotted in arrival distribution maps, we observe that regions with different chaotic behavior emerge as well as gradients that appear between them (see Fig. 3.9).

3.6.1   Classification of Particles

Given our analysis for each set of particles, we can classify them based on the behavior of the finite-time Lyapunov exponent and its relation to the escape time, i.e., the time that the set of particles spent in the system.

In these systems, we can identify five different regimes based on the particles' behavior. The particles with the shortest final times are transient (see Fig. 3.3). These are particles that have a final time lower than 50000 (in code/normalized units) and their initial position is around the equator in the maps in Figure 3.9. They do not spend much time in the magnetic
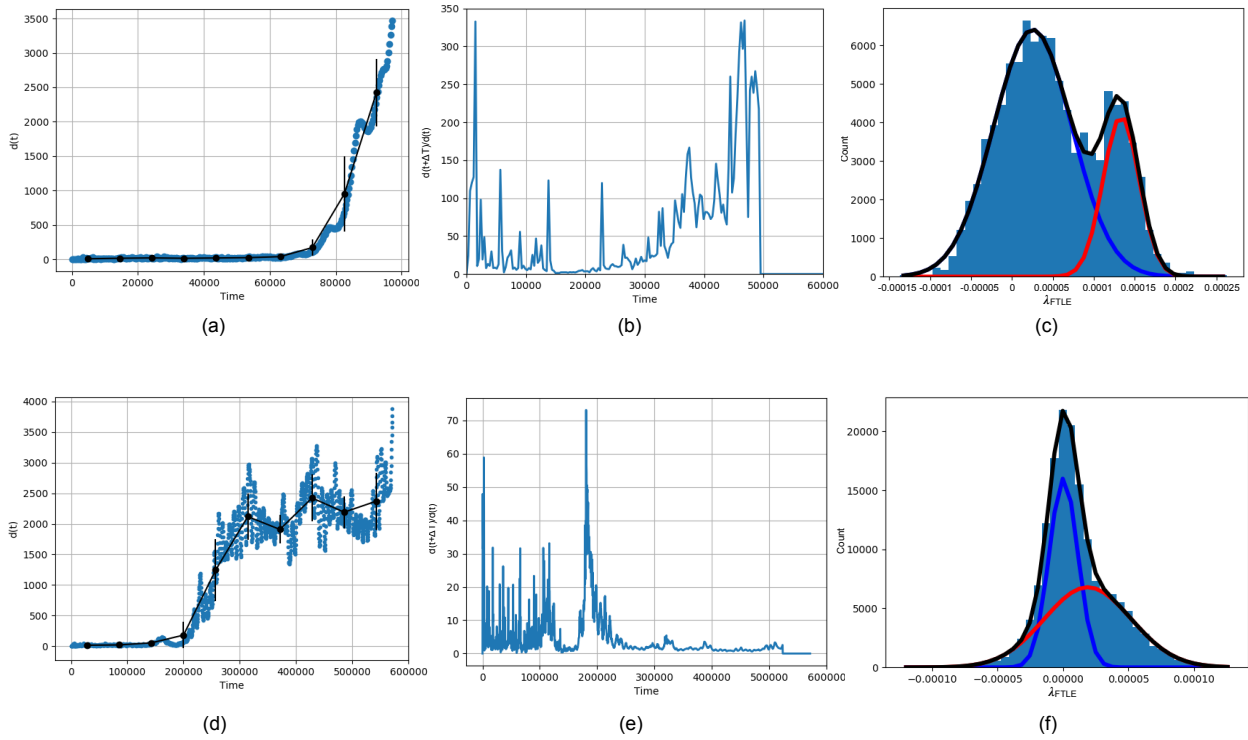
Figure 3.4: Comparison between the behavior of two particles with different escape times. *Top panels*: These correspond to a particle with an escape time $t_{esc} = 97251$. *Bottom Panels*: Particle with an escape time $t_{esc} = 5.7 \times 10^5$. (a) and (d) Distance in phase space vs. time. (b) and (e) Distance in phase space at time $t + \Delta t$ over the distance at time t as a function of time t. (c) and (f) Histogram of the finite-time Lyapunov exponent λ_{FTLE} and the corresponding fits denoted with black, red, and blue lines; see 3.5 for details on the Gaussian fits. Note that for the shorter trajectories (a), they stay with almost no separation for a short time and then diverge rapidly and leave the system right away. On the contrary, longer trajectories (d) take longer to start diverging and when they do, the process takes a longer time with intermediate periods of slower divergence before they are able to escape.

system and these trajectories pass through regions with no strong variations of magnetic field intensity that could compromise their adiabaticity. Since they escape the system very quickly, they do not have time to develop any chaos while in the system.

Particles with final times between 50000 to 10^5 are in an intermediate state (see Fig. 3.3). Particles in this intermediate state diverge so quickly that the system can not contain them, and therefore they can not reach a steady state for their chaotic behavior. The particles tend to have the highest values of λ_{FTLE}, especially in the perturbed cases.

The great majority of particles have final times between 10^5 and 10^8 (see the histogram in Figure 3.8). These trajectories are chaotic and consequently sensitive to the initial conditions. Their behavior follows a power law that correlates the escape time and the Lyapunov exponent.

The particles that fit this power law behavior can be subdivided in two categories depending on their chaotic attributes, irregular and regular. Irregular particles have final times between 10^5 and $10^{5.5}$. The divergence of these particles is sudden, and they do not experience a steady state as the regular particles do (see panel (a) in Figure 3.4).

Regular particles, with final times between $10^{5.5}$ and 10^8, start to diverge at a slower pace compared to the irregular particles. Later, after a period of divergence, they achieve a steady state. They spend most of the time in this steady state, and then they leave the system (panel (d) in Figure 3.4). These trajectories are long trajectories at the margin of the stability region in phase space.

The final category is trapped particles. These particles are only present in the unperturbed system. Their final time is our maximum value of 10^8. These trajectories occupy the stability region, which is the region in phase space where trajectories remain trapped within the integration time (here 10^8). These trajectories, despite being very long, are not sensitive to initial conditions, and they are stable. They will be permanently trapped in the magnetic mirror if there is no time-dependent perturbation. With time-dependent magnetic perturbations, these trajectories lose their adiabatic properties and escape after a relatively long bounded period. This change depends on the strength of the perturbation, as we will see in the next subsection.

3.6.2 Finite-Time Lyapunov Exponents vs. Escape Times

In Figure 3.5, the data for each set of particles is divided into eleven bins, according to their escape times t_{esc}. Then, an average for each bin is calculated and denoted by a red point in the figure. Subsequently, the red points are connected by a red line to show the trend for the profile. This profiling is also done for Figures 3.6 and 3.7 for the perturbed cases.

Given this profile, it is found in Figure 3.5 that the distribution exhibits a power-law behavior after reaching the maximum values for λ_{FTLE} at $10^{-4.0}$. The power law extends from $t_{esc} \sim 10^5$ to the maximum escape times for the system. The fit for the profile is given by the expression

$$\lambda_{FTLE} = \beta \, t_{esc}^{-1.04 \pm 0.03}. \tag{3.10}$$

This fit has an R^2 value of 0.995 and a scaling value $\beta = 10^{1.24 \pm 0.15}$.

One important feature to notice is that this slope is the same that the perturbed cases in Figures 3.6 and 3.7 exhibit. In Fig. 3.6, we can see that the data for the weak perturbation and the strong perturbation all show the same power-law behavior with a slope of approximately minus unity. This feature is even more clear in Figure 3.7. The particles denoted in blue have the same initial conditions as the others but are subjected to different perturbations. Even though these perturbations affect the final escape time that they have, their behavior is still along the same power law.

In Fig. 3.6, the different sets of particles are subjected to various magnetic field configurations, as described in Section 3.2. For each set of particles, the initial conditions for the reference trajectories are kept the same, so that any differences will arise from the various perturbations introduced in the system. From this figure, we can see that if these perturbations are present in the system, the distribution of particles in the different categories of the FTLE changes. However, the same power-law behavior remains. The most evident features that changed in this perturbed case are that there are no longer particles in the trapped category, and particles are rearranged along the power law depending on how strong
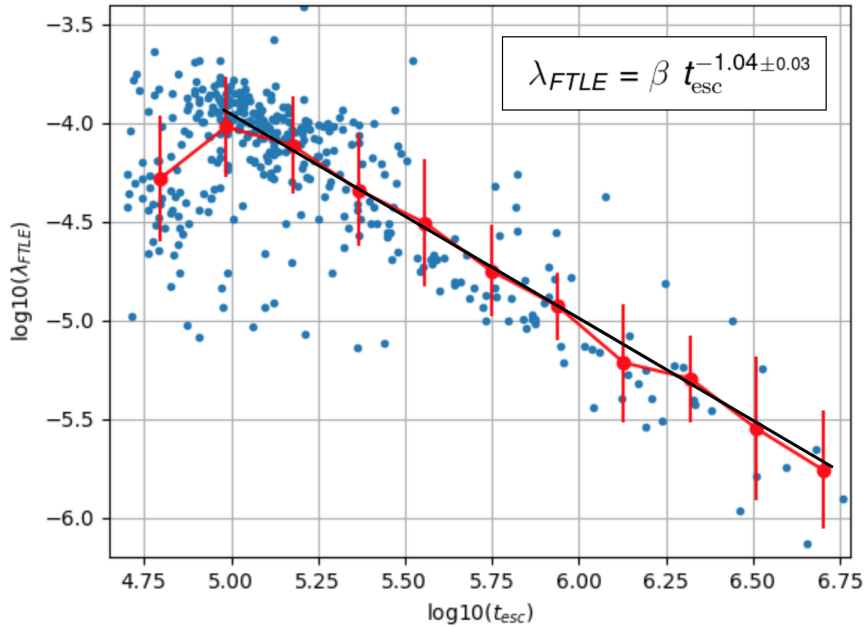
Figure 3.5: *Unperturbed system*: The finite-time Lyapunov exponent, λ_{FTLE}, vs. the escape time from the system, t_{esc}, for the unpertubed system. The blue points denote the specific values for each set of particles, which correspond to different initial conditions. The profile is denoted by the red points and the red line connecting them. The vertical red error bars correspond to one standard deviation. Note that from $t_{esc} \sim 10^5$ to the maximum escape time, the distribution follows a power-law–like behavior. The fit for the power law of the profile is given by the Eq. 3.10, which shows a power of -1.04.

the perturbation they experience is. For example, if a weak perturbation is introduced, we can still see that there are particles in the regular region. However, if a strong perturbation is present, particles tend to leave the system at a faster pace; therefore, the regular and trapped categories will be depleted of particles.

This migration of particles from one category to another one is shown in Figure 3.7. Here particles originally in the regular category of the unperturbed system (denoted in blue in the figure) were subjected to the various perturbations. The reference particles' initial momentum and position are kept the same. It is shown here that these sets of particles escape the system more quickly, moving to the irregular and intermediate categories when a weak perturbation is present. In the presence of the strong perturbation, almost all of them move to the intermediate category. Additionally, even though the particles change their
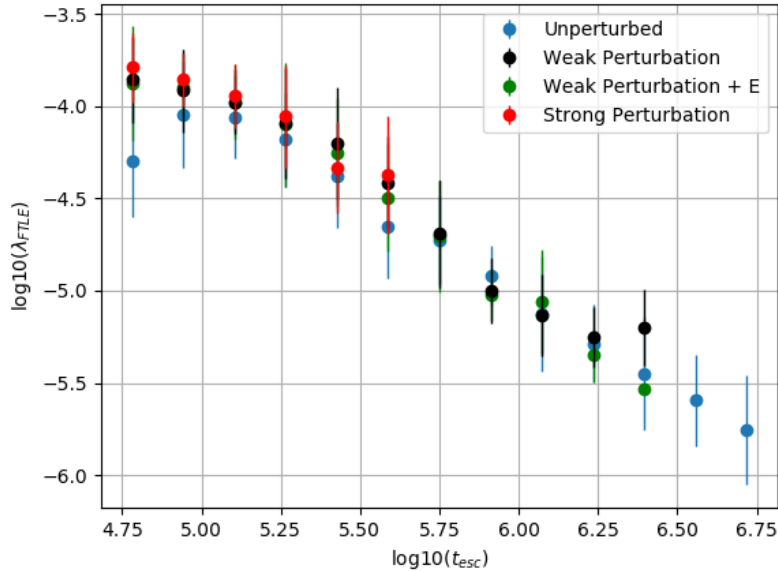
Figure 3.6: *Comparison of perturbed systems.* The finite-time Lyapunov exponent, λ_{FTLE}, vs. the escape time from the system, t_{esc}, for four different cases. The blue points represent the unperturbed system shown in Figure 3.5. The black points correspond to the profile of the weak-perturbation system, the green ones show the weak perturbation plus electric field, and the red ones the strong-perturbation system. Section 3.2 shows the description for each magnetic field configuration. Note that once perturbations are introduced in the system, the overall distribution of particles in the different categories changes; nonetheless, the power-law behavior and slope remain the same.

categories and move to shorter escape times, they do so in a manner that still complies with the power-law behavior.

The histogram depicted in Figure 3.8 shows the distribution of particles for the final escape times in the unperturbed system. This histogram can be interpreted as a probability distribution plot for escape times, where the most likely scenario is around $t_{esc} = 10^5$. This most probable case is consistent with the migration plot in Figure 3.7. In that figure, when perturbations are introduced, the particles tend to move to shorter times and accumulate around the $t_{esc} = 10^5$ range for the most extreme case. Therefore, a histogram such as the one in Figure 8 could be used as a predictor for the expected behavior of a set of particles when the system is perturbed. For example, a particle that has a long escape time will have a tendency to move to a more likely scenario when the perturbation is introduced.
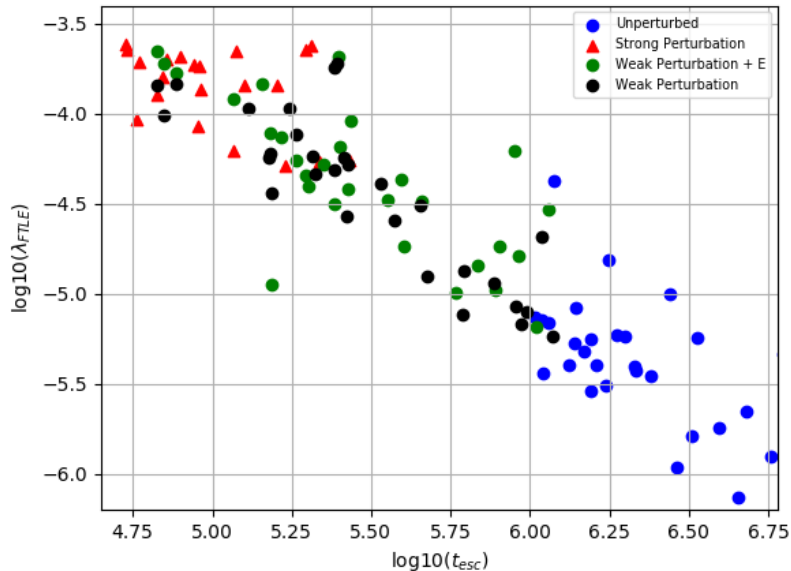
Figure 3.7: *Migration.* The finite-time Lyapunov exponent, λ_{FTLE}, vs. the escape time from the system, t_{esc}, for the same set of reference trajectories. The original set of particles in the unperturbed system is shown in blue. The black points show the same set of reference trajectories but subjected to a weak perturbation. The green points correspond to these particles in a weak perturbation plus electric field system, and the red points represent the particles affected by the strong perturbation. Note that even though the reference trajectories have the same initial conditions, these particles originally in the regular category in the perturbed system can reduce their escape times by a factor of two if affected by a strong perturbation. But in doing so, they still show the same power-law behavior.

3.6.3 Maps

Following the calculation of the finite-time Lyapunov exponents and escape times for the sets of trajectories, we proceed to plot them in an arrival distribution map (see Fig. 3.9). The location of each pixel corresponds to the arrival direction of a reference particle and the value assigned to each pixel indicates the FTLE (Fig. 3.9 top panel) or the escape time (Fig. 3.9 bottom panel). Therefore, the maps correspond to a visual representation of the different chaotic behaviors and how they are distributed. In these arrival distribution maps, we can identify that there are regions of stability where the particles are trapped within the maximum integration time (denoted in deep red in the top panel of Fig. 3.9). Originating from those regions, gradients from longer to shorter escape times appear. Since t_{esc} is related
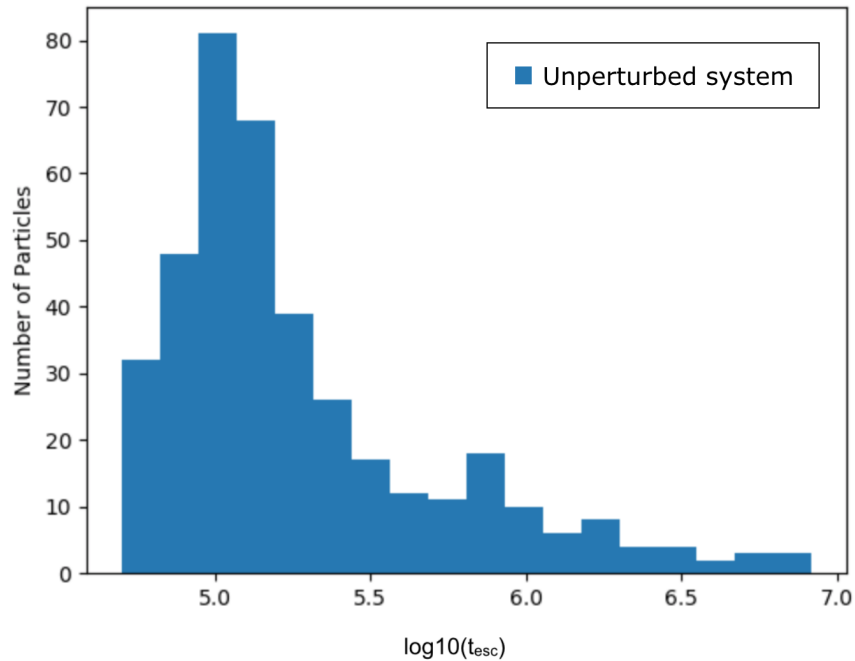
Figure 3.8: *Histogram for final escape times.* Number of sets of particles vs. the escape time from the system, t_{esc}, in the unpertubed system. Note that if we interpret this plot as a probability distribution, particles are more likely to have escape times around $t_{esc} = 10^5$, which is consistent with the migration depicted in Figure 3.7.

to the FTLE, the chaotic behavior of particles follows this trend as well; see Fig. 3.9 bottom panel.

Particles in the power law are located outside that stability region and populate the rest of the areas of the map (except for the region around the equator). Regular particles with very long trajectories are located at the margin of the stability region, with moderate Lyapunov exponents and manifesting a metastable behavior. Then, we can see a transition to the higher Lyapunov exponent for particles with shorter times (intermediate and irregular particles), which are more spatially distributed in the map.

The particles in the equator remain for a particularly short time in the system and therefore do not contribute to the Lyapunov maps. Their exponent is taken to be zero under these conditions.

For the case of the maps with perturbations present (see columns 2 and 3 in Fig. 3.9), we see significant changes that start to appear as the perturbation goes from weak to strong.
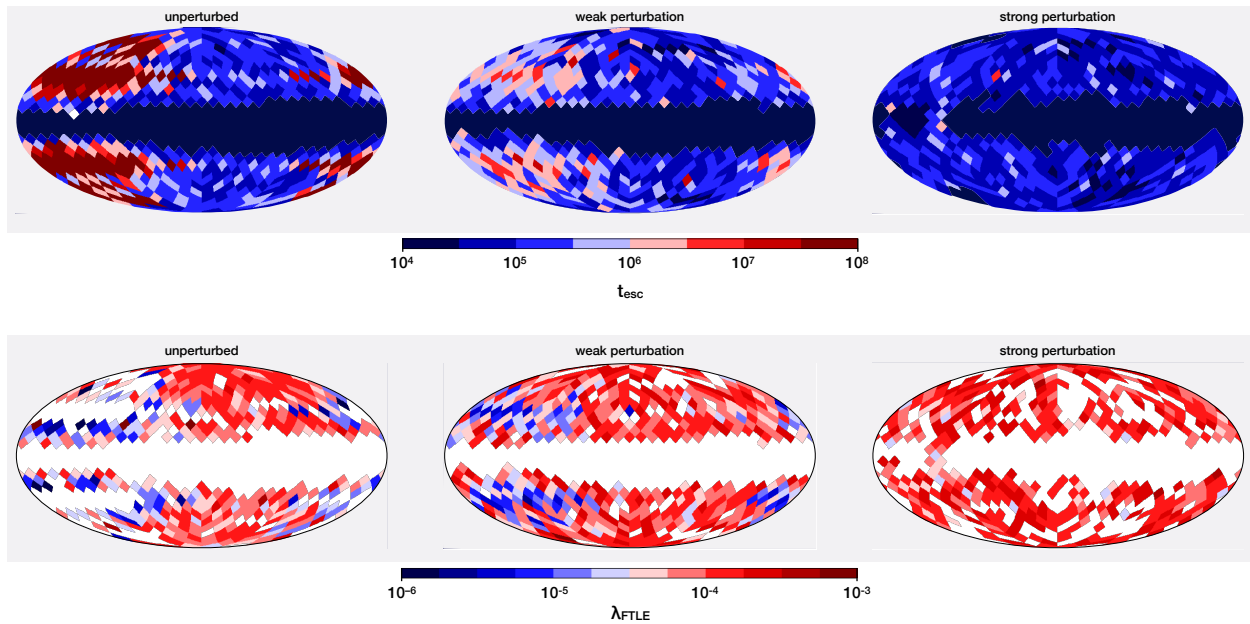
Figure 3.9: *Maps.* The top panel corresponds to the escape times for the unperturbed, weakly perturbed, and strongly perturbed systems, respectively. The bottom panel corresponds to the finite-time Lyapunov exponent, λ_{FTLE}, for those systems. These maps correspond to a visual representation of the different chaotic behaviors and how they are distributed spatially.

The most obvious change is that there is not a stability region in these cases, but still the transitions from lower FTLE to higher values are present. For the weak perturbation, there is still a variety of behaviors and values for the FTLE, yet, for the strong perturbation, we see that it is more restrictive on the values that the exponents can take, and it is basically populated by one type of particles, as we have seen in the λ_{FTLE}, vs. the escape time t_{esc} plots. The FTLE values for these particles are uniformly distributed in the map as well.

3.7   Discussion

A new method to calculate the chaotic behavior of particles' trajectories in bound systems has been developed. This method is based on the calculation of the finite-time Lyapunov exponent, a quantity that is adaptable to bounded conditions; see Section 3.4. The FTLE is

used to characterize the particles' behavior while bounded in the system but also to capture changes in behavior and transitional states. For example, particles inside a coherent magnetic structure can experience an exponential divergence, then move to a steady bounded state, and later escape. After this escape, they can propagate in a larger field and then encounter another structure where they could get bounded again. Consequently, instead of tracking just one regime, as would be the case for calculating a specific diffusive state, the FTLE can adapt to the changing conditions. Therefore, using it in conjunction with a well-defined diffusive state can yield a more comprehensive understanding of the CR propagation.

To describe the particles' behavior in bound systems, we constructed a toy model as our propagating medium. It consists of a magnetic bottle with time-perturbations added (see Section 3.2 for details). The specific parameters used in this work are based on the heliospheric magnetic configuration; nonetheless, it can be adjusted to fit different structures, as will be discussed in Section 3.8. This model captures the heliospheric large-scale magnetic features. One of these features is the magnetic mirroring effect between its flanks due to the draping of the interstellar magnetic field. The other effect is due to the solar cycles and its magnetic field variation in polarity.

As particles propagate in this system, they display chaotic behavior, as shown in Section 3.6. We found that the degree of chaos of the trajectories is correlated to the particles' escape time from the system. This relation is given by a power law, and depending on that, different behavioral regimes exist.

Particles can undergo four phases within the escape time that determine their behavioral category. However, a particle does not necessarily experience all of these phases. The initial phase is when divergence has not happened yet. Overall shorter trajectories experience almost no separation for just a brief interval compared to longer trajectories, for which this period is considerably more prolonged, as seen in Figure 3.4. The next phase is the divergence stage, where longer trajectories diverge at a slower rate, hence their low FTLE values. A penultimate phase, observed in long trajectories, corresponds to an extended slow-divergence period and an approximately constant separation behavior. The particles remain bounded in

the system for a long time. The final phase is the escape, where particles leave the confined system.

Different CR behavioral categories can be identified in these bound systems, as discussed in Section 3.6. These regimes depend on multiple elements, such as the trajectories' specific characteristics, the phases particles experienced, and their corresponding chaotic behavior.

The first of these categories is for particles that leave the system in a short time, and therefore, they cannot develop any chaos. These transient particles have very smooth trajectories and do not experience significant variations in the magnetic field. In a realistic environment, these particles will most likely trace out the magnetic field outside the bound system. For example, particles that enter the heliosphere through the nose spend a very short time in the heliosphere before being detected at Earth. Therefore, they could experience the least deviations and be more closely connected to their original direction in the interstellar medium.

The second type of particles are in an intermediate state. These particles did not achieve their maximum chaotic potential since they escape the system before doing so. Their divergent behavior is very explosive and occurs in a short period. They encounter regions where the magnetic fields vary vastly, and in consequence, their escape times are shortened. Consequently, these particles are not likely to be able to trace out the magnetic field outside the magnetic structure. Their behavior is in between the transient and the power-law regime in the system.

The next category, and where the vast majority of our particles reside, is the power-law regime. When we explore the relation between the FTLEs and the escape times, a power law emerges; see Fig. 3.5. In this power law, the Lyapunov exponent follows the inverse of the escape time; see Eq. 3.10. As we have seen in Figure 3.4, particles that diverge too quickly are unable to maintain that rapid divergence for an extended period, due to the finite size of the system, and escape rapidly. On the other hand, a slower divergence gives particles plenty of time to spend bounded in the system before leaving it. Therefore, shorter trajectories have higher FTLEs, and longer trajectories display less chaotic behavior.

Different factors contribute to the power-law relation of the FTLE vs. escape time. These elements are based on the connection between the magnetic field geometry and the test particle's energy.

One of the elements that conditions the particles' behavior in the system is the ratio ω_{bounce}/ω_g, where ω_{bounce} is the bouncing frequency between the mirrors, and ω_g is the gyro-frequency. This ratio's value is smaller for trapped trajectories than those from other categories of particles, and it does not vary much in general. This ratio has a more significant variation and a higher value for the more chaotic particles.

There are also limitations set on the maximum FTLE given by the configuration of the system. In Figure 3.5, it is shown that the highest values for the FTLE have magnitudes of 10^{-4} and are found in the vicinities of $t_{esc} = 10^5$. The maximum value achievable for the FTLE for which the particles can still be bounded is 4.90×10^{-4}. It is a constraint given by the system's physical dimensions. Its value is determined by the maximum separation that particles can achieve while still trapped and the time that it takes to achieve it, as denoted in Eq. 3.6. For instance, a particle with a $\lambda_{FTLE} = 10^{-3}$ would not be able to stay in the bounded system since its divergence is so extreme.

Therefore, for a real finite system, one could know its chaotic potential just by the system's overall dimensions compared to the characteristics of the impinging particles. This indication could be beneficial if there is a collection of similar coherent structures. Each of them can contribute to the general behavior, and we could predict their effects in the overall propagation. For example, we would expect these conditions in certain interstellar medium regions, so that we could see how the diffusion of CRs is affected by the presence of a collection of coherent magnetic structures.

Another element present in the FTLE vs. escape time plots is an inflection point in the profile. For the unperturbed system, an inflection point is found in the profile (Fig. 3.5) where the maximum values for the FTLE occur ($t_{esc} = 10^5$). This inflection point at the profile's maximum values is expected since the intermediate particles displayed a very explosive divergence and are not stable enough to remain in the system. The particles at the

inflection position are the most chaotic that were able to thoroughly diverge in the system. From that point on, particles will start to diverge at a slower pace. However, the exact location of the inflection is dependent on the perturbations that act on the system. For the perturbed cases, this inflection point is located at a shorter escape time and a slightly higher value of the λ_{FTLE}, as shown in Figure 3.6. Since the perturbations are a source of chaos in the trajectories, this decrease in escape time and increase in the FTLE values of the inflection point is expected. Nonetheless, this shift in the inflection point location is restricted since its maximum value is already determined by the system's dimensions, as mentioned before.

An important attribute that this system presents is that if the system is perturbed, the particle's behavior still falls along the same power law. As shown in Figure 3.6 and more clearly in Figure 3.7, once a perturbation affects a set of particles, the particles' behavior becomes more chaotic, but it follows the same power law as in the unperturbed case. Multiple factors can contribute to this phenomenon, from the perturbation's spatial dimensions to the overall magnitude of the perturbations' magnetic field compared to those from the magnetic bottle.

One of the aspects that could contribute to the permanence of the particles in the power law is that the time-perturbation is not very extended spatially compared to the bottle's dimensions. The particles are essentially still on the same system configuration, and the perturbation will solely drive them to another possible path of the same system. Accordingly, they will follow the same power law. Moreover, as we have seen in Figure 3.8, the region around $t_{esc} = 10^5$ is the most likely scenario; consequently, as the system is perturbed, it will be driven to this most probable case.

Another contributing factor is that the perturbation is not strong enough to change the whole behavior. Therefore, the first order in terms of the system is the magnetic bottle. Suppose the magnitude of perturbation was higher, or perhaps its extension was ampler. In that case, the bottle's magnetic field will be secondary, and the overall behavior, including the slope in FTLE vs. escape time, will change. This point is also related to the fact that the perturbation that the particles experience does not vary that much as the particles' trajectory

progresses. For example, for the strong perturbation and a particle with a final time of 10^5, the perturbation only moves 6.6 AU before the particle escapes the system.

Nonetheless, even if the perturbation does not deviate the particles from this power law, the cumulative effect of the magnetic bottle plus the perturbation does create severe chaotic changes. This idea points to the fact that even small changes can have significant effects.

Given the invariance under these perturbations that the Lyapunov-exponent–escape-time relation displays, this exact power law could prove to be an intrinsic property of the system. Similar power laws could be found for different configurations. Nonetheless, this will require investigating a variety of systems.

Another aspect to consider is how chaos and magnetically connected areas in the system can affect the observations. There are two different perspectives from which we can look at this problem. One is from the particles that are impinging the magnetic structure from the outside. The other is from the point of view of the solid angle at which the particles are detected.

From the observational point of view, the limitation resides in that we do not have the exact initial and final coordinates of the particles' trajectory. Furthermore, in these physical systems, magnetic fields could have already changed slightly by the time two consecutive trajectories pass by with the same initial position. Therefore, those trajectories will deviate from each other, and that entry point will likely correspond to two different arrival directions.

When assessing the effects on the arrival direction's anisotropy, we have to consider the different roles that each category of particles can have in the arrival distribution maps. For example, if the magnetic structure's effect is strong, then the original distribution can be completely scrambled. For a more moderate perturbation, as the one analyzed here or in the case of the heliosphere, the effect is significant, yet some of the original distribution could remain. Therefore, we could expect two situations: the map's overall distribution or parts of it are shifted slightly, or regions of the maps are changed while others are practically unaffected.

Therefore, if there is time-variability in the maps, the particles that will mainly drive this

variation and that will be the most affected are the chaotic ones (those in the intermediate and power-law categories). The transient particles may not be affected or moved as a whole, i.e., its variation will be a slow drift. Consequently, transient trajectories could provide a direct mapping between initial and final phase space configuration. Chaotic trajectories, on the other hand, could provide only an average mapping.

3.8   Outlook

As cosmic rays propagate, they encounter magnetic structures that could trap them temporarily and induce chaotic behavior on their trajectories. The model that we develop in this study can be used to represent a variety of magnetic structures and magnetic processes where cosmic rays can get momentarily trapped. In addition, the method we construct here to characterize chaotic behavior based on the FTLE can be applied to these cosmic-ray trapping scenarios. However, it can also be used when particles move rapidly from one environment to another, and their trajectories experience a change of first-order effects on them.

The rate at which CRs have such bounding interactions depends on several factors. One of the determinant elements is the particle's energy or, more specifically, the particle's rigidity, R = E/Ze. Depending on the particle's rigidity and its corresponding gyroradius in a specific magnetic field, it can experience strong effects from magnetic structures of a similar scale. If the gyroradius is smaller than the coherent structure, it will be affected by the magnetic field's large-scale geometry. If it is larger than the magnetic perturbation, accumulating effects will be felt.

The trapping of cosmic rays with their consequent chaotic effects can happen at various scales, from particles in the interstellar medium to the intercluster media. Also, different types of processes can be behind it. Therefore, from their place of origin to their detection at Earth, a particle can be affected by multiple coherent magnetic structures. Nonetheless, we can expect the number of interactions to vary for a distribution of particles at different rigidities or injected in different places in the galaxy.

For instance, we can visualize two distinct extreme scenarios for two particles at different rigidities. For a PeV proton injected into the galaxy, the motion could be dominated by the trapping of a few specific magnetic structures at the time of the detection. However, we could consider, for example, 1-TeV protons, for which the situation may look completely different. These cosmic rays with lower energy could have the chance to encounter more structures that can affect them. We could also conceive that differences will arise if particles are injected in a relatively quiet place in the galaxy instead of a very turbulent and energetic site. These scenarios can profoundly affect the arrival distribution at Earth, since our surroundings could select particles with specific rigidities.

We can expect these interactions to arise from the cosmic rays' interplay with very well-defined structures such as the heliosphere or as a result of more basic phenomena, e.g., structures that appear due to spatial intermittency.

The magnetic configuration that we use as inspiration for our toy model system is the heliosphere. Here we have a significant source of mirroring effects between the flanks of the heliosphere. Moreover, there are a variety of perturbation sources. One of them is the one that comes as a result of the solar cycles that we described in this study. The particles' chaotic behavior could change depending on the phase in the solar cycle in which the system is. The perturbation phase may distribute chaotic and non-chaotic CRs differently as a function of the phase of magnetic perturbation. This effect is because the surrounding space has different magnetic field polarities. Therefore, a time-variability could come from the existence of a perturbation, but the definite characteristics of it can have a significant impact, in this case, the polarity.

Other perturbation sources are the instabilities at the interface between the ISM and the heliosphere, turbulence, and the motion that the heliospheric flanks have relative to the inner heliosphere. In [37], this latter motion is described as having a speed of 10-100 AU per year, which could be a consistent source of variability and directionality in the maps.

Similarly, we could expect mirroring effects or trapping in more extensive structures, such as the Local Interstellar Cloud (LIC) or the Local Bubble (or Local Cavity) (see [27, 23] for

details). The LIC has an extension of 30 light-years and the Local Bubble of 300 light-years. So their influence can span over particles with rigidities in the 10^{17} V region.

As mentioned before, spatial intermittency plays an essential role when dealing with the creation of coherent structures in a particular medium [32]. These structures affect the CR propagation and a possible diffusive state. These effects can be involved in various scenarios at different scales, such as the ISM or solar processes.

3.9 Conclusions

In this work, we have explored the possibility that chaotic behavior can originate from the interaction between cosmic rays and a toy magnetic model that consists of a magnetic bottle with time-perturbations and the potential consequences that it can have on the cosmic ray arrival distribution.

The conclusions are summarized as follows:

- Our results show that the Finite-Time Lyapunov Exponent, a quantity that indicates the chaotic behavior of a trajectory, is related to the escape time of the system. A specific power-law gives this relation that even persists if perturbations act on the system. This specific power law could prove to be an intrinsic characteristic of the system.

- The maps of arrival distribution in these systems display areas where the chaotic characteristics vary significantly.

- Time variability could prove to be an essential aspect of the observed anisotropy. Since these magnetic structures are located so close to the Earth; therefore, there is no time for them to be homogenized.

Bibliography

[1]   Abeysekara, A. U., Alfaro, R., Alvarez, C., et al. 2019, ApJ, 871, 96. doi:10.3847/1538-4357/aaf5cc

[2]   Aartsen, M. et al. 2013b, Astrophys. J. 765, 55

[21] Blasi, P., & Amato, E. 2012, JCAP 1, 11

[32] Erlykin A.D., & Wolfendale A.W. 2006, Astropart. Phys. 25, 183

[67] Ptuskin V. 2012, Astropart. Phys. 39, 44

[66] Pohl, M. & Eichler, D. 2013, Astrophys. J. 766, 9

[77] Sveshnikova, L.G. et al. 2013, Astropart. Phys. 50, 33

[72] Savchenko, V., Kachelrieß, M. & Semikoz, D.V. 2015, DOI:10.1088/2041-8205/809/2/L23

[31] Effenberger, F. et al. 2012, A&A 547, A120

[60] Mertsch, P. & Funk, S. 2015 Phys. Rev. Lett. 114, 021101

[39] Giacinti, G., & Sigl, G., 2012 Phys. Rev. Lett. 109, 071101

[12] Ahlers, M. 2016 arXiv:1605.06446

[11] Ahlers, M., & Mertsch, P. 2015, arXiv:1506.05488

[85] López-Barquero, V. et al. 2016, Astrophys. J. , 830, 19

[59] López-Barquero, V., Xu, S., Desiati, P., et al. 2017, ApJ, 842, 54. doi:10.3847/1538-4357/aa74d1

[28] Desiati, P. & Lazarian, A. 2013, Astrophys. J. 762, 44

[29] Desiati, P. & Zweibel, E.G. 2014, Astrophys. J. 791, 51

[75] Schwadron, N.A., Adams, F.C., Christian, E.R., Desiati, P., Frisch, P., Funsten, H.O., Jokipii, J.R., McComas, D.J., Moebius, E., Zank, G.P. 2014, Science 343, 988

[82] Zhang, M., Zuo, P., & Pogorelov, N. 2014, Astrophys. J. 790, 5

[20] Lopez-Barquero, V. & Desiati, P. 2019, 36th International Cosmic Ray Conference (ICRC2019), 36, 1109

[21] Desiati, P., Díaz Vélez, J. C., Pogorelov, N., et al. 2020, arXiv:2009.04883

[22] Xu, S. & Lazarian, A. 2020, ApJ, 894, 63. doi:10.3847/1538-4357/ab8465

[23] Abt, H. A. 2015, PASP, 127, 1218. doi:10.1086/684436

[24] Pogorelov, N. V., Borovikov, S. N., Zank, G. P., et al. 2009, ApJ, 696, 1478. doi:10.1088/0004-637X/696/2/1478

[25] Benettin, G. 1984, Physica D Nonlinear Phenomena, 13, 211. doi:10.1016/0167-2789(84)90278-1

[26] O'c. Drury, L. 2013, International Cosmic Ray Conference, 33, 835

[27] Frisch, P. C. 1998, IAU Colloq. 166: The Local Bubble and Beyond, 269. doi:10.1007/BFb0104732

[43] Gorski, K. M., Hivon, E., Banday, A. J., et al. 2005, ApJ, 622, 759

[94] Pogorelov, N.V., Suess, S.T., & Borovikov, S.N. 2013, Astrophys. J. 772, 2

[30] Galassi M., Davies J., Theiler J., Gough B., JungmanG., Alken P., Booth M., Rossi F. 2009, *GNU Scientific Library Reference Manual (3rd Ed.)*, ISBN 0954612078., http://www.gnu.org/software/gsl/

[31] Shukurov, A., Snodin, A. P., Seta, A., et al. 2017, ApJL, 839, L16. doi:10.3847/2041-8213/aa6aa6

[32] Matthaeus, W. H., Wan, M., Servidio, S., et al. 2015, Philosophical Transactions of the Royal Society of London Series A, 373, 20140154. doi:10.1098/rsta.2014.0154

[33] Dawson, S., Grebogi, C., Sauer, T., et al. 1994, Phys. Rev. Lett., 73, 1927

[34] McCue, L.S., Troesch, A.W. 2011, Use of Lyapunov exponents to predict chaotic vessel motions. In: Neves, M.A.S., et al. (eds.) Contemporary Ideas on Ship Stability and Capsizing in Waves, Springer, Dordrecht, 415.

[35] Szezech, J. D., Lopes, S. R., & Viana, R. L. 2005, Physics Letters A, 335, 394

[36] Wolf, A., Swift, J. B., Swinney, H. L., et al. 1985, Physica D Nonlinear Phenomena, 16, 285

[37] Merav Opher, James Drake, Gary Zank et al. 2021. PREPRINT (Version 1) available at Research Square

[38] B. V. Chirikov, Proceedings of the Royal Society of London. Series A, Mathematical and Physical Sciences, Vol. 413, No. 1844, Dynamical Chaos (Sep. 8, 1987), pp. 145-156

[39] A. Ambashta & R.K. Varma, Plasma Physics and Controlled Fusion, Vol. 30, No. 10, pp. 1279 to 1296, 1988

Chapter 4

Heliospheric Effects on the Cosmic-Ray Anisotropy

Does anisotropy arise from the CR interactions with the heliosphere?

In this chapter we performed numerical calculations to test the idea that the anisotropies of TeV cosmic rays may arise from their interactions with the heliosphere. For this purpose, we used a magnetic field model of the heliosphere and performed direct numerical calculations of particle trajectories. Unlike earlier work testing the idea, we did not employ time-reversible techniques that are based on Liouville's theorem. We showed numerically that for scattering by the heliosphere the conditions of Liouville's theorem are not satisfied and the adiabatic approximation and time-reversibility of the particle trajectories are not valid. Our results indicate sensitivity to the magnetic structure of the heliospheric magnetic field, and we expect that this will be useful for probing this structure in future research.

A version of this chapter has previously appeared in The Astrophysical Journal. López-Barquero, V., Xu, S., Desiati, P., et al. 2017, ApJ, 842, 54.

4.1 Introduction

Cosmic rays (henceforth, CRs) with energy below 10^{18} eV have a gyroradius smaller than the galactic disk thickness of about 300 pc, with energy-dependent confinement within the Milky Way. The topics related to the origin, propagation and acceleration of CRs are still debated in spite of the long history of relevant studies (see the excellent textbook by [84] and references therein). However, it is generally accepted that most of the galactic CRs are being accelerated by supernova shocks. Some percentage of the CRs can be accelerated by magnetic reconnection [59][1]. Spatially, supernovae are correlated to star-forming regions, so the distribution of CRs is affected by that of their sources, but it is modified by propagation through the galactic magnetic field. Frequently the magnetic field in the Galaxy is described as composed of a global regular component [see, e.g., 48, 49], large-scale coherent (on the order of 10-100 pc) structures, and the ubiquitous turbulent component (with wide spatial-scale inertial range with amplitude following a Kolmogorov power spectrum). This is, however, an approximation, with the availability of the modern theory of magneto-hydrodynamic (MHD) turbulence (see [30] for a review) predicting a more sophisticated picture, with compressible and incompressible modes having their own cascades [41], henceforth GS95 [58, 25, 36, 65]. For sub-Alfvenic turbulence, which is typical within quiescent regions of the interstellar medium (ISM), the transition from weak turbulence to strong Alfvenic turbulence takes place [55, 53]. The latter has the Kolmogorov-type spectrum $\sim k^{-5/3}$. However, this spectrum is strongly anisotropic and therefore the scattering by Alfvenic turbulence injected at large scale is marginal [34, 119], with fast modes identified by [119] as the major scattering component induced by the galactic turbulent cascade.

An additional scattering emerges from CR instabilities. Streaming instability has been long considered an important component of CR propagation physics (see [32] for a review). Particle streaming was employed in models such as the leaky box model of propagation to

---

[1]Magnetic reconnection becomes fast, i.e., independent of resistivity, in turbulent media [55, 65, 66] (see also review by [81] and references therein). A similar acceleration mechanism that appeals to tearing is discussed in a later publication by [41].

explain the high isotropy of observed CRs. In that model, it was assumed that the streaming instability was suppressed in the partially ionized galactic disk and acts to scatter and return CRs as they enter the partially ionized galactic halo. The streaming of particles outside the disk was able to naturally explain the observed dipole anisotropies of the observed CR distribution. This model was later challenged in [45], who performed calculations of the streaming instability damping by the ISM turbulence and concluded that the streaming is not expected to take place for the levels of turbulent damping that they adopted. More recently, this conclusion was questioned in [75] where it was shown that for typical halo conditions scattering instability takes place in the galactic halo. Additional instabilities of CRs (see [76, 80]) can act as additional sources of CR isotropization. In this paper, we assume that the influence of scattering induced by the TeV CR instabilities in the vicinity of the heliosphere is negligible.

The limitation of the traditional models of CR propagation is not only due to scattering physics. In fact, at scales less than the turbulent injection scale, the particles following magnetic field lines experience super-diffusion with respect to the direction of the mean field [80]. Such effects can be strongly distorted if the synthetic data cubes are used. Therefore, in what follows, we use only the data cubes obtained by direct MHD numerical simulations.

This paper continues our numerical studies of the origin of CR anisotropies observed at Earth. The first paper, [85] (hereafter referred to as LX16), dealt with the effects of interstellar turbulence on the CR propagation and it did not take into account the strong perturbations induced by the heliosphere. In this paper, on the contrary, we focus our attention on the effects arising from the CR interactions with the heliosphere. The idea that the heliosphere can produce strong scattering on CRs, which could be important for explaining the observed high-energy CR anisotropies, was first suggested in [28] (hereafter referred to as DL13). This idea was later tested numerically in [75] and [82]. The difference between our paper and the earlier studies is that we do not assume that Liouville's theorem and the backtracking of particles is valid. In fact, in this paper, we show that the conditions of Liouville's theorem are not satisfied due to the scattering at the heliospheric boundary.

Therefore, we adopt a much more time consuming Monte-Carlo approach with the forward tracking of particles.

The paper is organized as follows. In Section 4.2, the problem of observed anisotropy of CRs is formulated along with ways to address it, while in Section 4.3.1 the long tail heliospheric model used in this study is described. Section 4.3 describes the particle integration method used and which CR particles are used in the study. In Section 4.4, we discuss the validity of applying Liouville's theorem in the context of this work. Results are presented in Section 4.5 and discussed in Section 4.6. Concluding remarks follow in Section 4.7.

4.2 The Problem of Anisotropies and Corresponding Approaches

Particle energy roughly determines which spatial scale is the most dominant in shaping the characteristics of their distribution. Galactic CRs in the energy range below about 50 GeV are strongly affected by modulations of the inner heliospheric magnetic field, in correlation with solar cycles (see, e.g., [33, 98, 64, 34]). Above 50 GeV, the modulation in the CR energy spectrum is negligible; however, the effects of long-term solar cycles on particle distribution is still observed up to an energy of few hundred GeV [62, 64]. The gyroradius of 10- to 100-GeV CR particles in the interplanetary magnetic field of < 1 μG is typically smaller than the size of the termination shock [about 80–90 AU, see 95]. This makes it possible for those particles to be spatially redistributed according to the modulating solar wind-induced perturbations on the magnetic field.

At TeV energies, a scale transition occurs. The typical particle gyroradius is larger than the size of the termination shock, therefore the influence of inner heliospheric magnetic fields on the CR distribution is negligible. In fact, solar cycle modulations are subdominant in this energy range. However, TeV galactic CRs coming from the ISM, where the local interstellar magnetic field (LIMF) is $\sim$3 μG, and propagating into the heliosphere have gyroradius on

the order of 100 AU, which is smaller than the estimated transverse size of the heliosphere of about 600 AU and shorter than the estimated length of the heliospheric tail of a few thousands AU [65, 95, 97]. From this scaling relationship, TeV CRs are expected to be influenced by the heliospheric magnetic field (see [28], hereafter referred to as DL13). At an energy scale of tens of TeV, the gyroradius of the lightest CR particles starts to exceed the heliosphere's transverse size, thus decreasing its influence; nonetheless, these particles will still experience the influence of the perturbation created by the heliosphere on the local interstellar medium (LISM) and the effects of the heliotail's length on their propagation. At higher energies, the arrival directions of the CRs are influenced by their propagation through the interstellar magnetic field (see LX16) and by the distribution of their sources in the Galaxy.

It is, therefore, expected that CRs with energy below several tens of TeV are influenced by the heliosphere to some extent. The actual degree of such an effect depends on the properties of the heliosphere, such as its size and the magnetic structure, the presence of magnetic perturbations or instabilities at the boundary with the ISM (e.g., at the flanks of the heliosphere), the large-scale perturbation of the LISM due to the heliosphere, and the mass composition (or better the rigidity[2]) of the CR particles. If the heliosphere has the effect to redistribute the TeV CR arrival direction distribution, compared to that shaped by interstellar propagation, all those details need to be properly understood and integrated into a comprehensive numerical particle trajectory integration.

From an observational point of view, a statistically significant anisotropy has been observed by a variety of experiments, sensitive to different energy ranges (from tens of GeV to a few PeV), located on or below the Earth's surface in the Northern Hemisphere [63, 45, 12, 13, 44, 7, 9, 81, 62, 14, 26, 73, 17] and in the Southern Hemisphere [3, 4, 5, 1, 2].

The global anisotropy appears to change with energy in a nontrivial way. From about

---

[2]Rigidity of a charged particle is a measure of its momentum, and it refers to the fact that a higher momentum particle has a higher resistance to deflection by a magnetic field. It is defined as $R = r_L \, B \, c = E/Ze$, with r_L the particle gyroradius and B the magnetic field [see 117]. A 1-TeV proton and a 26-TeV iron nucleus have rigidity of 1 TV.

100 GeV to tens of TeV, it has an approximately consistent structure at the largest scale, although its measured amplitude increases with energy. Above a few tens of TeV, the observed progressive change in the anisotropy topology may indicate a transition between two processes shaping the particles' arrival distribution at Earth, for instance, the transition from heliospheric-dominated to ISM-dominated influence, which culminates around 100 TeV (as observed in [2] and discussed in DL13).

However, the change in topology of the CR anisotropy as a function of energy can have different origins as well. In the scenario of particles in homogeneous and isotropic diffusion, the CR density gradient, and therefore the induced spatial anisotropy, has a dipolar shape. The direction of the dipole is expected to point towards the strongest source of the observed CRs, and its amplitude to depend on the diffusion coefficient. At different energies, the strongest contribution to the observations can shift from one source to another, thus changing the orientation of the dipole [32, 21, 67, 66, 77, 72, 12]. The difficulty with this scenario is that particle diffusion in the ISM is expected to be anisotropic, i.e., fast along and slow across the magnetic field lines. A misalignment between the CR density gradient and the regular galactic magnetic field prevents pointing to any specific source, and it would suppress the anisotropy amplitude depending on the misalignment angle [31, 47, 75, 60]. Since the ratio of perpendicular to parallel diffusion is likely to depend on energy (depending on the magnetic field geometric configuration), the change in orientation of the anisotropy is also linked to the properties of the interstellar magnetic field itself.

The observed anisotropy cannot be described with a simple dipole component. The actual distribution is a combination of several angular scales [15, 6, 4, 16, 8, 2] that can be studied by decomposing it into individual spherical harmonic contributions. This makes it possible to determine the angular power spectrum of the observed arrival distribution. As reported by experimental observations, most of the power is concentrated in the large-scale anisotropy structure, which includes dipole, quadrupole, and octupole. Such contributions are likely affected by the limited field of view of the experiments and also by biases that limit the observation at large scale (see, e.g., [11]). About 1% of the power is distributed

across small-scale structures in the arrival direction distribution (where there is no bias due to the field of view). Small angular scale anisotropy features correspond to regions where CR flux has large gradients in a relatively localized area in the field of view of the observations (on the order of 10°). Such regions can be stochastically produced by scattering processes of CRs in the ISM magnetic turbulence within the particle mean free path, as discussed in [39, 10, 11] and our companion paper LX16. Such scattering processes have the effect of decomposing a large-scale particle density gradient into small-scale components. This process constitutes an important contribution to the power spectrum, and it is certainly compatible with observations. However, it is possible to argue that some observed localized regions of TeV CR excess appear to be correlated with features associated with the heliosphere. For instance, one of the localized excess regions observed in the northern equatorial sky appears to be correlated with the direction of the heliospheric tail (see, e.g., [15, 6, 16, 8]). CRs observed within this localized region have an energy spectrum that is harder than that in the surrounding areas. It was proposed that reacceleration of CRs by magnetic reconnections in the heliospheric tail may be a possible explanation [54, 27]. Other localized regions are spatially correlated with the large angular gradient edge of relative intensity across the whole sky, with a possible link to heliospheric origin (as discussed in DL13).

Instabilities that develop dynamically at the boundary between the heliosphere and the ISM (see Section 4.3.1), such as Rayleigh–Taylor and Kelvin–Helmholtz instabilities, can have an effect on the cosmic ray arrival at Earth [83, 125, 126, 46, 65, 26, 127, 112, 95]. Specifically, if they have spatial scales on the order of 10-100 AU, they can induce scattering processes on multi-TeV-scale CRs that cross the heliosphere. Therefore, potentially, if an stability affects the configuration of the heliopause that can have an impact on the CR distribution. However, currently the information on the exact characteristics of the heliopause is limited, thus more direct measurements are needed to assess the definite nature of these instabilities. The possibility that strong resonant scattering processes cause a redistribution of the CR arrival direction distribution was already discussed in DL13. As mentioned, other authors have studied the effects of the heliosphere [75, 82] or, in general, of astrospheres [110] on the

distribution of TeV CRs. Additionally, magnetic field reconnection plays an important role in the heliopause. For instance, turbulent magnetic reconnection ([55], see also [81] and ref. therein) can induce the first order acceleration of energetic particles [59, 72, 41], which was shown to be relevant to the heliospheric settings [78, 42].

The heliospheric model used in the present work makes use of ideal MHD treatment of ions and of a kinetic multi-fluid description of neutral interstellar atoms penetrating into the heliosphere ([94]). This model incorporates the heliospheric tail up to a distance of approximately 4000 AU, which does not cover the maximum possible extension (see Section 4.3.1). In this study, the possibility that resonant scattering processes may have a strong effect on redistributing TeV CR arrival direction distribution is critically discussed. The relevant points of the present study are to dispute whether Liouville's theorem can actually be used as a tool to determine the particle trajectories affected by the heliospheric magnetic field and whether the heliosphere itself imprints a strong effect on the cosmic particles crossing it. If magnetic fields change significantly within gyroradius spatial scale, the geometry of particle trajectories may be highly sensitive to the actual initial conditions; i.e., they may have a chaotic nature. In such a case, application of Liouville's theorem is not warranted and particle distribution may follow a different scaling. In general, application of Liouville's theorem must to be investigated case by case. In what follows, we use direct numerical simulations of CR propagation using the numerical results of heliospheric simulations and without any use of Liouville's theorem.

4.3 Cosmic-ray Propagation in the Heliosphere

In this section, the description of the heliospheric magnetic field model used in the present study is laid out, then the strategy and method used to numerically integrate the particle trajectories through the heliosphere is described.

4.3.1 Heliosphere Magnetic Field Model

The heliosphere is formed when the solar wind (SW) collides with the local interstellar medium (LISM). In an ideal magnetohydrodynamic formulation of the problem, the SW–LISM interaction necessarily creates a tangential discontinuity that separates the plasmas originating at these two sources. This discontinuity is called the heliopause (HP). The HP extends thousands of astronomical units (AU) from the Sun. As any tangential discontinuity, the HP is subject to hydrodynamic instabilities, e.g., the Kelvin–Helmholtz (KH) instability [see, e.g., 22, 33, 106, 105]. Moreover, the HP nose is subject to Rayleigh–Taylor (RT) instability. The role of gravity in this case is played by the momentum-exchange terms in the MHD equations describing the plasma flow in the presence of charge exchange [83, 126]. Linear analysis [18] of the RT instability performed in an idealized formulation showed that perturbations grow unconditionally while they are small. Nonlinear, numerical investigations of the RT instability have been performed by Florinski et al. [46] and Borovikov et al. [26] in an axially-symmetric case, and by Borovikov & Pogorelov [27] in a realistically three-dimensional formulation. It was demonstrated in the latter paper that the heliospheric magnetic field (HMF) can damp the RT instability. However, the HMF becomes rather small occasionally in the course of solar cycle, so the instability results in a substantial mixing of LISM and SW plasma at the nose of the heliopause. Interestingly, Borovikov & Pogorelov [27] shows that RT instability may reveal itself also at the HP flanks, but it is caused by charge exchange with secondary neutral atoms born inside the heliosphere. As a result, the HP surface bounding the heliotail is subject to the mixture of KH and RT instabilities.

Since the KH instability is of a convective type, with the perturbation amplitude growing as a function of distance along the HP, plasma mixing as well as diffusion processes would eventually destroy the HP. However, it appears that charge exchange is a dominant process that results in continuous elimination of the hotter SW ions with cooler ions possessing properties of the LISM H atoms. As shown by Izmodenov & Alexashov [63] in an axially-symmetric case and Pogorelov et al. [96] in 3D, this makes the SW flow superfast magnetosonic

(its Mach number calculated using the fast magnetosonic speed is greater than 1) at about 4,000 AU. In the investigation presented in this paper, we use one of the heliotail models described in Pogorelov et al. [96]. This model is based on a self-consistent solution of the ideal MHD equations, with appropriate source terms due to charge exchange between ions and neutrals, to describe the flow of plasma and the Boltzmann equation to describe the transport of neutral atoms. To avoid issues related to the heliospheric current sheet, this model assumes a unipolar distribution of the HMF inside the heliosphere. It shows initial collimation of the SW plasma inside the Parker spiral field lines bent tailward by the flow, as predicted by Yu [122]. The spiral field being kink-instable [104, 96], the reason for such collimation disappears at about 800 AU from the Sun. In contrast with Yu [122] and multi-fluid simulations of Opher et al. [92], no separation of the HP into two lobes occurs in Pogorelov et al. [96]. This is because multi-fluid models substantially depress charge exchange across the lobe separation region. Such entirely hydrodynamic artifacts are impossible if atoms are treated kinetically. We assume the following properties of the LISM: temperature $T_\infty = 6300$ K, velocity $V_\infty = 23.2$ km/s, proton density $n_\infty = 0.082$ cm^{-3}, H atom density $n_{H\infty} = 0.172$ cm^{-3}, and magnetic field strength $B_\infty = 3$ μG. The LISM flow comes from the direction $(\lambda, \beta) = (79°, -5°)$, while the $\mathbf{B}_\infty$ vector arises from $(\lambda, \beta) = (225°, 44°)$ in the ecliptic coordinate system [128]. The SW is assumed to be spherically symmetric with the following properties at 1 AU: plasma density $n_{SW} = 7.4$ cm^{-3}, temperature $T_{SW} = 51100$ K, radial velocity $V_{SW} = 450$ km s, and radial magnetic field component $B_R = 37.5$ μG. The HMF is assumed to be Parker's at 1 AU.

4.3.2   Particle Trajectory Integration

Similar to the work in LX16, this study is performed by integrating particle trajectories in the magnetic field described in Section 4.3.1, using the set of 6-dimensional ordinary differential
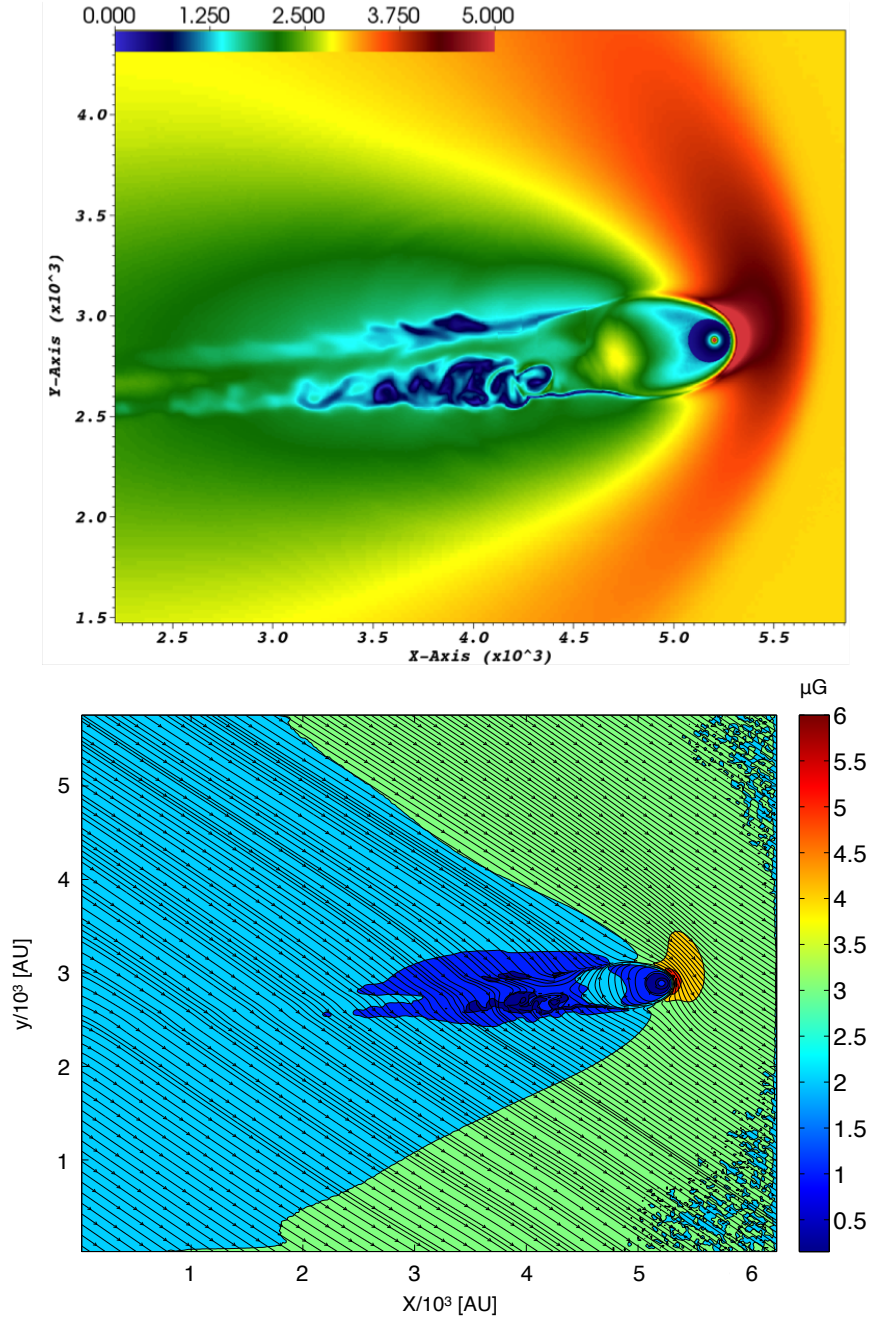
Figure 4.1: Meridional projection of the heliospheric magnetic field model described in Section 4.3.1. At the top, the figure shows high-resolution visual details of the magnetic fields (color code in units of μG) with the axes in units of AU. At the bottom, the figure shows the magnetic field lines (coarse color code in units of μG) with the axes in units of AU. The simulation box is $320 \times 280 \times 280$ grid points, corresponding to $6400 \, \text{AU} \times 5600 \, \text{AU} \times 5600 \, \text{AU}$ (20 AU/grid point).

equations

$$\frac{d\vec{p}}{dt} \;=\; q\left(\vec{u} \times \vec{B}\right) \tag{4.1}$$

$$\frac{d\vec{r}}{dt} \quad = \quad \vec{u}, \tag{4.2}$$

describing the Lorentz force with $\vec{u}$ the particle velocity, $\vec{r}$ its position vector and $\vec{p}$ the momentum. For $\vec{B}$, we use one steady-state realization of the heliospheric magnetic field described in section 4.3.1. As in LX16, the equations are integrated using the Bulirsch-Stoer integration method [68] with adaptive time step. At each integration step, the magnetic field is interpolated using a 3D cubic spline, and integration is stopped when particles cross the border of the simulation box. The choice of one specific realization of the magnetic field is justified by the fact that particle velocity is much larger than the plasma Alfvén velocity; thus, induced electric fields can be neglected.

Figure 4.1 shows the meridional projection of the heliospheric model snapshot (described in section 4.3.1) used in this study. At the top, the figure shows high-resolution visual details of the magnetic fields (color code in units of μG) with the axes in units of AU. At the bottom, the figure shows the magnetic field lines (coarse color code in units of μG). The initial simulation box is $320 \times 280 \times 280$ simulation grid points (the longer dimension to allow the inclusion of the heliospheric tail) where each grid point corresponds to 20 AU. This is equivalent to 6400 AU $\times$ 5600 AU $\times$ 5600 AU. The model has a varying resolution, depending on the region within the heliosphere, with the highest resolution in the region around the Sun, where it is 1 AU (0.05 simulation grid points). The model includes magnetic instabilities, on spatial scales on the order of 10-100 AU, that grow on the flanks at the boundary with the ISM, and a tail with length of approximately 4000 AU. In the model, the uniform interstellar magnetic field outside of the heliospheric boundary has intensity of about 3 μG. For the study presented in this work, the original simulation box is extended in such a way that a sphere centered at Earth and with radius 6000 AU (300 simulation grid points) is inside it. In the extension of the simulation box, a uniform magnetic field with intensity 3 μG and with the same direction as in the simulation is assumed.

In order to calculate the distribution of CRs at Earth after their propagation across

the interstellar and heliospheric magnetic field, there are two possible methods that can be followed. One is to integrate a large number of particle trajectories (typically isotropically distributed) initiated on Earth and *back-propagate* (or *back-track*) them to outer space. The other method is to integrate particle trajectories initiated at a large distance from Earth and *forward-propagate* (or *forward-track* them, meaning directly propagate them according to the arrow of time) towards Earth. The back-propagation technique is based on the validity of Liouville's theorem, which states that particle density in phase space is conserved along the particle trajectories if conditions such as no collisional scattering or no resonant collisionless scattering are satisfied (see section 4.4). If the theorem conditions are valid, then particle trajectories can be time reversed. This method is very efficient, because it entails the integration of particle trajectories from the target back into outer space. Nevertheless, there is no particle loss, and only portions of space that are directly *magnetically connected* to the target location have non-zero particle density population. Therefore, it is necessary to impose an initial anisotropy as a directional dependent weight in order to calculate the particle distribution at the target position. Such a weight function breaks the isotropy initially constructed and provides the anisotropy distribution transmitted back to the target position from the magnetically connected remote regions of space. By construction, this technique does not take into account the generation of anisotropy from particle escape during their propagation.

In the presence of turbulence or instabilities, magnetic fields can vary in spatial scales that are shorter than the particle gyroradius. This breaks adiabaticity and effectively induces collisional processes that may invalidate the application of Liouville's theorem. The validity of Liouville's theorem is extensively discussed in LX16. In Section 4.4 of this paper, it is argued that the theorem does not have the grounds to be applicable for this particular study of heliospheric effects, and therefore it cannot be utilized. In this case, therefore, the forward-propagation method is used. Such a technique is implicitly inefficient because only a small fraction of the injected particles will make it to or near the target. As discussed in [70] as well, this method naturally accounts for the role that CR escape has in shaping the

anisotropy. There is no need to assume a global anisotropy at large distance (injected, for instance, by CRs diffusively propagated away from a source) to obtain anisotropy at Earth, since particles naturally stream along interstellar magnetic field lines and undergo scattering processes in magnetic turbulence or instabilities.

In this study, it is argued that scattering at the boundary between the heliosphere and the ISM breaks the particle trajectory reversibility in that those particles that escape without reaching Earth cannot be represented in a back-propagation calculation method. Yet, those trajectory configurations occur and contribute to the overall shape of CR arrival direction distribution. In addition, the distribution of CRs at Earth is reshaped by the heliospheric instabilities in a stochastic manner and the exact individual features produced by this phenomenon may not be predicted; therefore, a statistical approach is used, for instance by calculating the angular power spectrum of the arrival distribution.

The inefficiency intrinsic to the forward-propagating methods is compensated by starting particle trajectory integration only from those areas in space where they have a significantly higher chance to reach the neighborhood of Earth, and by assuming a "larger size" of Earth to record the trajectories that arrive at the final target. Although this last assumption may lead to approximate results, it is sufficient to unveil the role that the heliosphere has on the propagation of TeV CRs independent of the propagation history in the ISM. The actual prediction of the anisotropy details most probably results from fine-tuning of several effects, and it is not addressed in this work.

4.3.3   Cosmic-Ray Composition

An important aspect of this study is taking into account that CRs are not dominated by protons only, which is particularly true at energies in excess of 1 TeV. As shown in [38] and references therein, the abundance of helium nuclei is already comparable to that of protons at the TeV energy range, and it starts to dominate at 10 TeV. Heavier particles become increasingly more important at higher energies as well. Figure 4.2 shows that the maximum
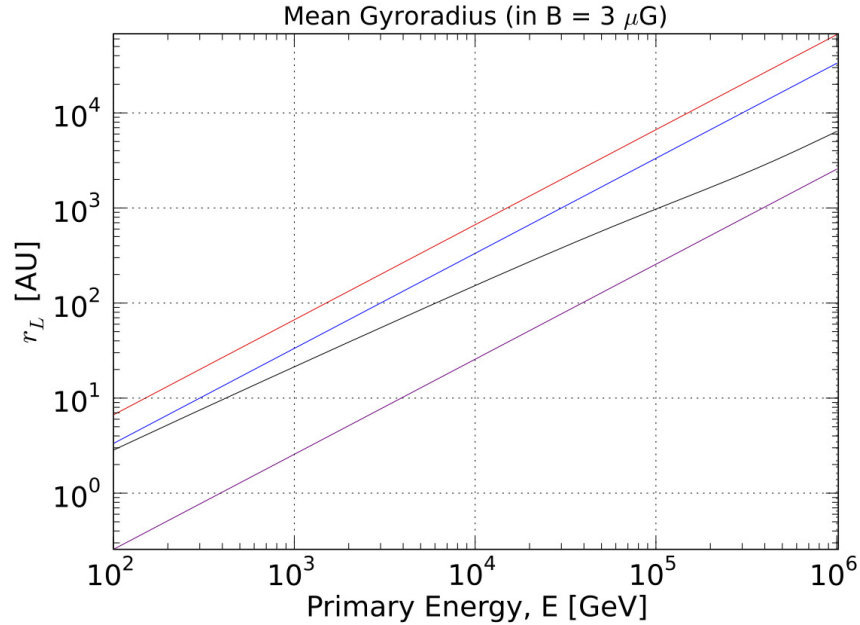
Figure 4.2: Cosmic-ray maximum gyroradius (or Larmor radius) r_L in a 3 μG magnetic field as a function of particle energy averaged over the observed mass composition (from [38]) (black line). This is compared to that of protons (red line), of helium (in blue), and of iron nuclei (in purple). Note that due to the mass composition of cosmic rays the average gyroradius is smaller than that for pure protons. This difference becomes important for energies in excess of about 1 TeV.

CR particle gyroradius r_L, averaged over the CR composition, is smaller than that of only protons the higher the contribution from heavier nuclei. Therefore, the relevant quantity is not the CR particle energy but their rigidity $R = r_L B c$. Particles with same rigidity have the same gyroradius r_L in a given magnetic field B. Or, equivalently, an iron nucleus of energy E has a gyroradius that is 26 times smaller than that of a proton with the same energy and in the same magnetic field B. In the energy range of 1-10 TeV, galactic CRs are approximately composed of a mix of protons, helium, and heavier atomic nuclei [38]. CR composition is an important ingredient in the understanding of anisotropy, especially since heavier particles, i.e., with small rigidity, may have a non-negligible contribution even at relatively high particle energy.
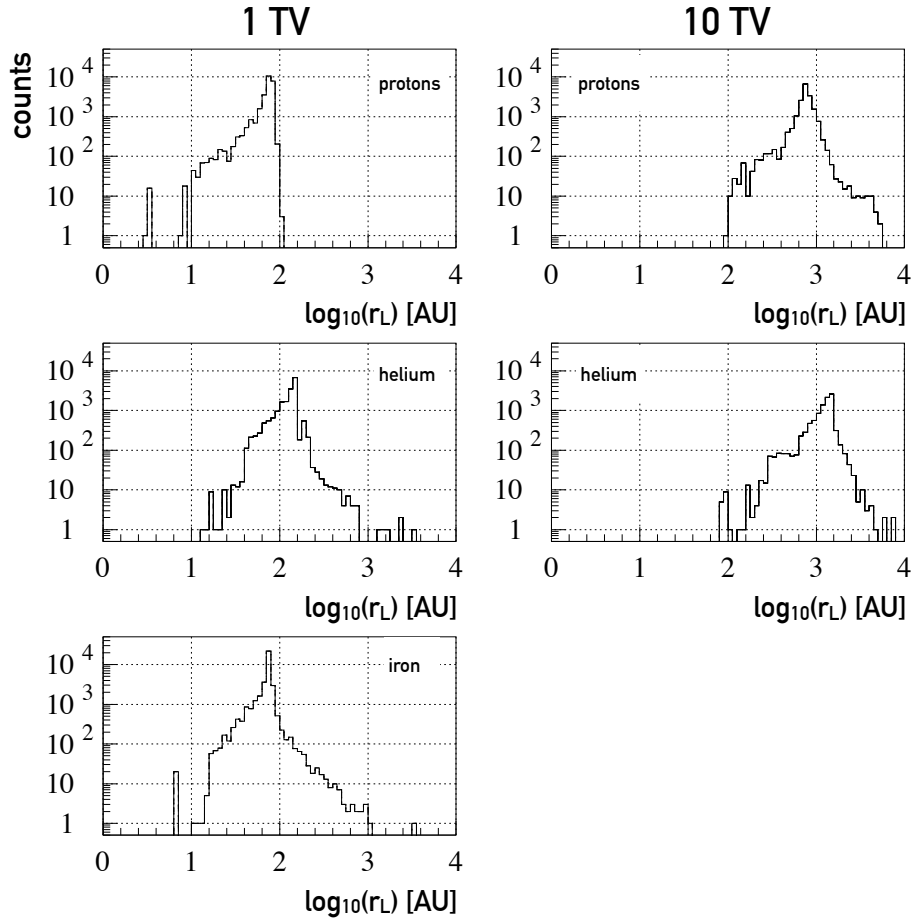
Figure 4.3: Distributions of instantaneous gyroradii r_L (in units of AU) of the particles from sets of Table 4.1 calculated along their trajectories. Note the wide range of variabilities of r_L due to the changes in magnetic field and pitch angle as particles propagate through the heliosphere.

4.3.4 Particle Data Sets

In this study, trajectories for three types of particles are integrated, as shown in Table 4.1: protons, helium, and iron nuclei. Since the energy range of interest is approximately 1-10 TeV, two rigidity ranges are used here: 1 TV (for all three particle types) and 10 TV (for protons and helium nuclei). For each set, 1×10^6 particle trajectories are integrated with initial position on a sphere (labeled as *injection sphere*) of radius 6000 AU (300 simulation grid points) centered on Earth and with uniform direction distribution towards the inner volume of the sphere. The initial positions correspond to regions where particles streaming

Table 4.1: Physics parameters of simulation sets

Set	Particle	E_p	$\langle r_L \rangle$	Injected particles	Recorded particles
1	Protons	1 TeV	70.23 ± 14.63 AU	1×10^6	8758
2	Helium	4 TeV	121.7 ± 54.5 AU	1×10^6	10416
3	Iron	30 TeV	72.89 ± 31.50 AU	1×10^6	6065
4	Protons	10 TeV	764.3 ± 252.2 AU	1×10^6	9789
5	Helium	40 TeV	$1235. \pm 383.$ AU	1×10^6	8655
				5×10^6	43683

along the LIMF have a higher chance to reach the Earth's neighborhood. To account for scattering processes, the injection regions, on the interstellar wind upstream and downstream directions of the LIMF, were initially identified by back-propagating particle trajectories from Earth across the heliospheric magnetic field (as shown in Figure 4.4). Once these main zones were identified, their extension was then expanded to account for the chance that particles initiated further away may reach Earth and yet maintain a manageable efficiency level. The regions where forward-propagated particle trajectories start are identified with a $30° \times 30°$ zone on the interstellar wind upstream side of the heliosphere (i.e., on the lower right side of Figure 4.4) and with a $60° \times 60°$ zone on the interstellar wind downstream side of the heliosphere (i.e., on the upper left side of Figure 4.4). For each set in Table 4.1, out of 1×10^6 particles initiated in both regions, approximately 1×10^4 reach the vicinity of Earth (i.e., cross a sphere centered on Earth, labeled as *target sphere*, of radius 200 AU (10 simulation grid points)).

The integrated trajectories from the sets of Table 4.1 are cumulated in the two rigidity range groups according to the relative mass composition from [38]: the 1 TV and the 10 TV rigidity scales. Table 4.1 shows the mean instantaneous gyroradius of the numerically integrated trajectories in the heliospheric magnetic field, and the corresponding RMS (numerical values taken from the distributions in Figure 4.3). The low-rigidity particle group corresponds to $\langle r_L \rangle \sim$ 70-100 AU (i.e., smaller than the size of the heliosphere). For a large fraction of particles, r_L is the same order of magnitude as the magnetic instabilities on the heliospheric boundary. Note the wide distributions of r_L in Figure 4.3 are due to the changes in magnetic

field and pitch angle as particles propagate through the heliosphere. The high-rigidity group corresponds to $\langle r_L \rangle \sim$ 700-1000 AU (i.e., just larger than the heliosphere transverse size but smaller than the predicted heliospheric tail length). As discussed in DL13, the rigidity scale of 10 TV is when the heliospheric effect on the particle distribution starts to become subdominant, compared to that from the ISM. This rigidity scale corresponds to CR particles in the range of 10-300 TeV, depending on the mass.

4.4   The Validity of Liouville's theorem

As discussed in Section 4.3.2, there are two possible ways to obtain the anisotropy at Earth. One involves the application of Liouville's theorem to link the distribution of the particles at some distance in the ISM to the arrival distribution at Earth. The other is to directly propagate the particles from outer space and record the particles' positions at Earth.

In LX16, the theoretical framework for the application of Liouville's theorem in the study of CR arrival direction was provided. The theorem states that the particle density in the neighborhood of a given system in phase space is constant if restrictions are imposed on the system [42]. We obtained the equation:

$$\frac{\partial \rho}{\partial t} + \vec{v} \cdot \vec{\nabla}(\rho) + \vec{F} \cdot \vec{\nabla}_p(\rho) = \frac{d\rho}{dt} = 0, \tag{4.3}$$

which is precisely the expression for Liouville's theorem [42, 23], where $\vec{\nabla}_p$ is the `del` operator in momentum space, ρ the distribution function, and $\vec{F}$ the applied external force.

The most relevant conditions for its application, as shown in LX16, are that the number of particles is conserved and that the forces acting on the particles are p-divergence free. This last restriction tells us that the forces have to be conservative and differentiable. Collision processes evidently violate this condition. In addition, Liouville's theorem can be considered in the context of conservation of information. Each time that a collision event occurs, it violates the connectedness, and information is lost. Therefore, particle trajectories cannot be
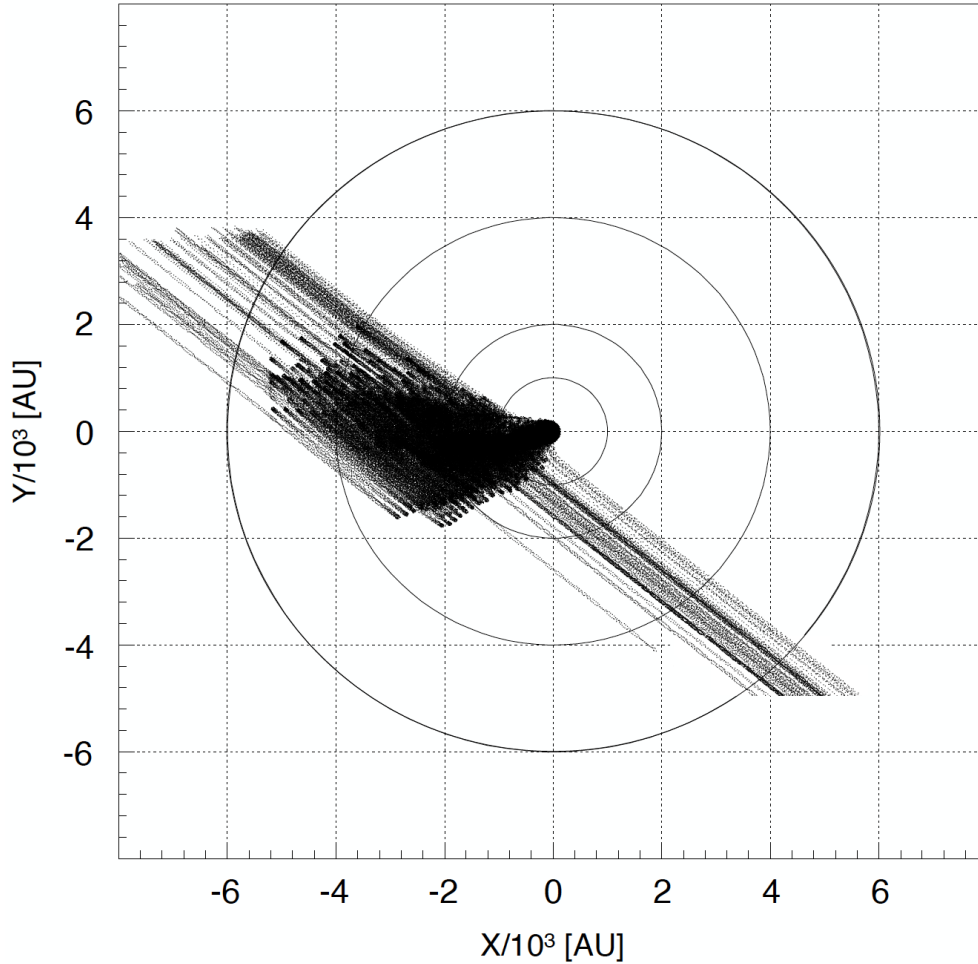
Figure 4.4: Integrated trajectories of protons with energy of 1 TeV, starting from Earth with initial uniform direction distribution, calculated with the heliospheric magnetic field of Figure 4.1. The figure illustrates the complex structure of over 100 trajectories passing through the heliosphere and ultimately streaming along the uniform interstellar magnetic field. The regions where the trajectories cross the injection sphere of radius 6000 AU are used to identify where to forward-propagate cosmic-ray particles (see text). Note that on the interstellar-wind downstream direction (i.e., in the upper left corner of the figure), particles are more spread out in space as an effect of the elongated heliospheric tail, compared to those in the upstream direction (i.e., in the lower right corner of the figure).

time reversed.

The derivation provided in LX16 for Eq. 4.3 is for a pure magnetic force, but in fact, when calculating particles' trajectories in a magnetic field subject to perturbations and instabilities, a variety of factors come into play. The most significant effect is when particles encounter a region where the magnetic field varies abruptly, i.e., the scale of variation of the magnetic

field is shorter than the gyroradius of the particle. In this scenario, the trajectory does not have time to adjust smoothly to this change, and the scattering process can be effectively considered a collision. For such cases, the right-hand side of Eq. 4.3 can be modified by the addition of a term, $\left[\frac{\partial \rho}{\partial t}\right]_c$, which takes into account collisions of various origins that are differentiated by their exact functional form, given the fact that they will cause a nonzero time rate of change in the distribution function [18]. Under these conditions, Liouville's theorem can't be applied.

To test the abruptness in particle trajectories, it is possible to calculate how the density in phase space is modified by scattering processes, i.e., how adiabatic the change is. In the presence of collisions, the magnetic moment of the gyrating particles changes. Therefore, to check for the adiabaticity of the trajectories, we can calculate the magnetic moment for each particle at each time step and find out if, statistically, it truly behaves as an adiabatic invariant. The relativistic magnetic moment (also called *first* adiabatic invariant) is given by:

$$\mu = \frac{p_\perp{}^2}{2m|\vec{B}|}, \tag{4.4}$$

where $p_\perp$ is the momentum perpendicular to the magnetic field $\vec{B}$ and m the particle mass. This quantity, relating magnetic field and perpendicular momentum of the particle, is conserved if the field gradients are small within distances comparable to the particle gyroradius. Note that no assumption about the conservation of magnetic moment is used in the numerical integration calculation.

To perform a statistical test on the first adiabatic invariant, we integrated trajectories from two different data sets, each with 1×10^4 particles, initiated at Earth and back-propagated to outer space. One set corresponding to 1 TeV and the other one to 10 TeV protons. Using these specific sets, the magnetic moment in Eq. 4.4 was calculated at each integration time step and plotted in a histogram. The mean value $\bar{\mu}$ of the magnetic moment of the particle ensemble from each data set and the corresponding standard deviation σ_μ were calculated. Figure 4.5 shows the ratio $\sigma_\mu/\bar{\mu}$ for the two sets. A distribution with $\sigma_\mu/\bar{\mu} = 0$
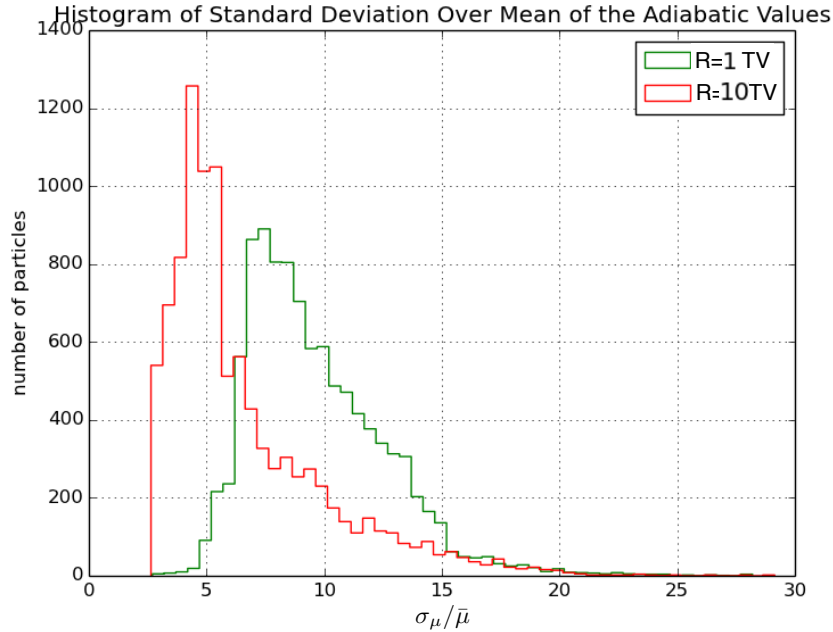
Figure 4.5: Histogram of standard deviation of magnetic moment σ_μ over mean magnetic moment $\bar{\mu}$ for the two rigidity data sets of Table 4.1. The red histogram corresponds to the R = 1 TV (p, He, Fe) mixed composition set, and the green histogram to the R = 10 TV (p, He) mixed composition. The magnetic moment is calculated for each particle at all time steps. The mean value and the standard deviation are for the total trajectory.

indicates that the conservation of the magnetic moment is perfect. In this case, particles can mirror back and forth between magnetic bottles, which maintain magnetic moment conserved. However, a distribution peaked at a value much larger than one means that the particles suffer strong variations in their trajectories and collision-like interactions happened. It is not simple mirroring for most particles, but effectively resonant scattering processes at the heliospheric boundary where particles propagate across magnetic field lines (see, e.g., [29]) with a stochastically redistributed pitch angle. The distributions obtained for these two sets show peaks at around 5 and 7, with strong skewness to the right, or towards higher values of $\sigma_\mu/\bar{\mu}$. This indicates that the magnetic moment fluctuated strongly, that severe changes have occurred, and collision-like interactions happened to the particles under consideration. A stronger deviation in the conservation of magnetic moment is observed with the low-rigidity set than with the high-rigidity set, because of the stronger scattering effects at lower rigidity. Note that in LX16 the same trajectory integration code was used to calculate particle

trajectories in compressible MHD turbulence, in the rigidity range between 750 TV and 30 PV. In that case, it was found that the ensemble average was $\langle \sigma_\mu/\bar{\mu} \rangle \lesssim 1$, i.e., significantly smaller than in the present case. The accuracy of the numerical trajectory integration is at the same level as that in LX16. The adaptive time step algorithms constrain both spatial and momentum coordinates to the same relative error level, thus limiting accuracy in spatial coordinates to a level that is $\ll r_L$, even after several tens of thousands of gyrations. Therefore, the strong nonconservation of the ensemble-average magnetic moment is not caused by lack of numerical accuracy but rather by the characteristics of the magnetic field used in this study. The scattering processes with the heliospheric magnetic instabilities determine the global statistical properties of the particles. The value of $\langle \sigma_\mu/\bar{\mu} \rangle$ in Figure 4.5 is smaller in the higher rigidity set because scattering is less effective in redistributing particles with a gyroradius significantly larger than the spatial size of the instabilities.

To conclude, interactions with the heliospheric magnetic field model used in this study result in dramatic changes in the distribution of particle trajectories. The original directional information carried by the particles is lost in these collision-like events. Trajectories diverge due to the magnetic field lines geometry in the regions of magnetic instabilities at the boundary between the heliosphere and the ISM. Thus, based on the above considerations, it is not possible to assume that Liouville's theorem is applicable in this case.

For that reason, in this work, the forward propagation method is used. With this method, anisotropy arises naturally from particle propagation and the interaction with the heliosphere. One important factor to take into account is that since there is a violation of the conditions of Liouville's theorem, we cannot make causal links to or rely in any way on the reversibility of the trajectories; consequently, this constrains the possibility of connecting a specific position in the ISM and the arrival direction at Earth. Therefore, it is only possible to determine to what degree the incoming distribution from outer space is distorted due to the features of the heliosphere but not possible to draw direct correlations between the incoming specific directions and the ones observed at Earth. In our case, we will show how the heliosphere acts on and distorts this distribution and how anisotropies arise.

4.5 Results

This section shows the results obtained with the numerical calculation data sets described in Section 4.3.2.

4.5.1 Sky Maps of Arrival Direction Distribution

The numerically integrated trajectories of the sets in Table 4.1 were combined according to the mixed CR composition from [38] (i.e., approximately 40% protons, 40% helium nuclei, and 20% iron nuclei at low rigidity and 50% protons and 50% helium nuclei at high rigidity) and used to study the effects that scattering processes on the heliospheric magnetic field have on the particle arrival direction distributions. As mentioned in Section 4.4, unlike the procedure followed in LX16, in this study particles were injected in two regions on the injection sphere at 6000 AU distance from Earth aligned along the LIMF and forward-propagated. At each point within those two regions, the particle directions were chosen from a uniform distribution towards the inner sphere. As shown in Table 4.1, a large fraction of the injected particles does not reach the target sphere, in proximity of Earth, because of scattering processes in the magnetic instability regions, thus contributing to the anisotropic distribution independently of the initial CR density gradient.

The particles hitting the target sphere were recorded and are represented in the sky maps of Figures 4.6 (for particles injected in the region downstream of the ISM flow, and in proximity of the heliospheric tail) and 4.7 (for particles injected in the region upstream of the ISM flow). In the figures, the direction of the heliotail is indicated with a yellow star. At the top of the figures, the initial positions on the injection sphere of those trajectories that reach the target sphere are shown. The yellow dashed boxes indicate the region of initial positions of all generated particles. The limited size of those regions show that those particles streaming along the LIMF within a relatively narrow magnetic field-line tube have the highest chance of reaching the target sphere. Note that, within those localized regions, all particles have a wide range of uniformly distributed pitch angles (or directions), which determines the

size of the corresponding gyroradius $r_L \approx (220/Z)\,(E/TeV)\,\sqrt{1-\mu^2}\,(\mu G/B)$ AU, with μ the cosine of the pitch angle. The instantaneous gyroradius along the particle trajectories are shown Figure 4.3 and the corresponding mean and RMS values in Table 4.1. At the center of the figures, the arrival directions of the 1-TV rigidity scale particles at the target sphere are shown. The sky maps show that, although particles arrive at the heliosphere streaming along the LIMF from one specific direction, they are significantly redistributed. Approximately 50% of the particles streaming from the downstream direction (and thus approaching the heliosphere in proximity of its elongated tail) undergo multiple scattering processes and appear as if they approach Earth from the upstream region (center of Figure 4.6). While, approximately 20-30% of the particles streaming from the upstream direction (and thus approaching the heliosphere in the proximity of its nose) appear to approach Earth from the downstream region (center of Figure 4.7). Resonant scattering along the heliotail has a more pronounced *focusing* effect towards the inner heliosphere. The wider injection region downstream (top of Figure 4.6) compared to that upstream (top of Figure 4.7) shows that the heliotail is able to *trap* particles more efficiently from larger distances downstream and collect them near Earth.

The arrival directions of the 10-TV rigidity scale particles on the target sphere are shown at the bottom of the figures. The effects of scattering on magnetic perturbations are still visible; however, the particle distribution is not as smooth, but it develops localized regions associated with the magnetic field geometric structure. Even at this high rigidity, it is possible to notice that multiple scattering effects of the heliotail are stronger for particles streaming downstream than for those upstream. At higher rigidity, with the decreasing influence of scattering, particle distribution is expected to converge to that at the injection sphere.

A side effect of the relatively large radius of the target sphere (200 AU, i.e., 2-3 times the gyroradius at 1-TV rigidity scale) is that, although the trajectories show the effect of multiple scattering processes across the heliospheric boundary (see Figure 4.4), they are not propagated too deep into the vicinity of Earth. As a consequence, although particles propagate across magnetic field lines with stochastically distributed pitch angle, the connection to the

large-scale magnetic field direction is still relatively strong because of the general structure of the heliosphere. This generates very low particle populations along directions that are approximately perpendicular to the LIMF (visible as a dark band at the center and the bottom of Figures 4.6 and 4.7).

The figures show a specific snapshot. However, particles reaching Earth are from all masses and energies, and ground-based experiments have relatively poor mass and energy resolutions. Each infinitesimal rigidity interval produces a characteristic fingerprint pattern similar to those in the figures, deeply dependent on the properties of the heliospheric magnetic field. Observations reveal the overlapping of those characteristic distributions, and, in fact, there is experimental evidence that coexisting anisotropy features originate from different energy ranges (see, e.g., [16, 2]). Even though in this study we provide a window on the possible effects of CR composition, a detailed prediction of the observation requires fine-tuning of several effects, which is not within the scope of this work.

4.5.2   Angular Power Spectrum

As discussed in the previous section, the topology of the sky maps in Figures 4.6 and 4.7 is associated with the specific rigidity scales used for the particular particle sets of Table 4.1. Because of the stochastic nature of scattering processes, statistically uncorrelated data sets would produce similar but not identical sky maps. Even with a seemingly different topology, however, such sky maps would have the same angular power spectrum, since this contains global statistical properties of the ensemble of particles, independent of the spatial location of the anisotropic features. The angular power spectrum, therefore, is a physically relevant quantity to study.

Figure 4.8 shows the angular power spectrum for the particle sets of Table 4.1. On the left, the results for the 1-TV rigidity sets and on the right for the 10-TV rigidity sets. For each particle set, the trajectories propagating from both injection regions are used (see Section 4.3.4). As expected, the shape of the angular power spectrum depends on particle

rigidity. As in LX16, the figures shows the angular power spectrum from the IceCube observatory [71, 2], the power spectrum from [10], and that corresponding to an isotropic arrival direction distribution of the same number of particles. In the figures, the power spectra are normalized to each other at the dipole component (i.e., $\ell = 1$).

CR particles in the 1-TV rigidity scale, as discussed in Section 4.5.1, are those most affected by multiple scattering induced by magnetic instabilities at the heliospheric boundaries. Their arrival direction distribution appears to develop angular structures on the order of $20°$ ($\ell \approx$ 10-15, where it reaches the statistical limit) as shown on the left of Figure 4.8. In the 10-TV rigidity scale, on the other hand, the small-scale filaments visible in Figures 4.6 and 4.7 contribute to the higher power for large values of ℓ on the right of Figure 4.8. As already mentioned, the sets used in this study represent two particular particle rigidity snapshots of the wide CR energy spectrum. Figure 4.8 highlights that a complex angular power spectrum arises even when particles propagate across relatively small-scale magnetic structures on a short distance scale. This overlaps with the effects of large-scale turbulence in the ISM over long distance scales (as discussed in LX16). While the ISM contribution is stochastically distributed, the heliospheric effects, although produced by scattering on magnetic instabilities, are expected to have directional correlations with the heliosphere. The experimental separation of the two contributions is the key to exploring the properties of the heliospheric magnetic field with TeV CRs.

4.6 Discussion

We have shown the dramatic effects that the heliosphere imprints on the CR arrival distribution at Earth. Our results show that the interactions of CRs with the heliosphere are relevant, and for the 1-10 TV range, cosmic-ray arrival cannot be studied without taking these effects into account.

The feature that distinguishes this work from previous studies is the forward-propagation technique used. We have shown that Liouville's theorem cannot be applied in this case because

resonant scattering on magnetic perturbations on the heliospheric magnetic field generates stochastic pitch angle distributions, and it effectively breaks adiabaticity (Section 4.4); therefore a back-propagation approach is not applicable. Another important idea behind the forward propagation is the concept of particle escape. As pointed out in Section 4.3.2 and in [70], particle escape due to transport in complex magnetic fields contributes to the resulting arrival direction distribution. Those particles that escape without ever reaching a given target location build up an uneven arrival direction distribution. In a back-propagation approach, there is no particle escape by construction. In this case, a weight function is used to inject an initial anisotropy for the reversed trajectories. The final anisotropy results from the spatial redistribution of a constant particle density.

The results of the present study are different from those in [75], where the importance of a relative large-scale excess of CR (due to a nearby supernova) was highlighted, without accounting for the effects of scattering on the heliospheric magnetic field. In our study, we use a self-consistent solution to the ideal MHD equations to obtain a model of the heliosphere. In that way, we can assess the direct heliospheric effects on the CR arrival distribution. And our approach is fundamentally different from the study in [82] and [75], where a back-propagation approach was used. In the case of [82], a model of the heliosphere was used, although different from the one used in the present study in that magnetic instabilities were not as prominent. Even though our forward propagation approach is computationally expensive, it is the only acceptable technique since the conditions of Liouville's theorem are not satisfied given the effective collision interactions with the instabilities in the heliosphere (Section 4.4).

Transport across the galactic magnetic field may be described with homogeneous anisotropic diffusion scenarios, where particles propagate faster along the magnetic field lines. If diffusion describes large-scale CR propagation in the ISM, the arrival direction distribution is expected to have a dipolar shape oriented along the LIMF. Even in the presence of multiple angular scale structures from nondiffusive propagation effects (see Section 4.1), it is usually assumed that the dipole component still has a direct connection to the underlying large-scale diffusion. Observations show that the dipole component appears to be aligned with the LIMF [12] after

accounting for the experimental biasing projection of angular features on the equatorial plane and the limited field of view of all ground-based experiments [11]. The actual direction of the dipole component can be considered accidental and perhaps associated to a relatively recent and nearby source of CRs contributing to the excess on one side of the LIMF lines rather than the other (see, e.g., [75] and [12]).

In reality, the structured interstellar magnetic field, with its different overlapping contributions at different spatial scales, easily generates deviations from the simple diffusion scenario. Particles with a given rigidity are likely to be more strongly affected by magnetic fields with gyro-scale spatial structures. This can cause dramatic changes in the transport properties (see for instance [29] and references therein). At a given rigidity scale, CR particle distributions are shaped, over their entire propagation history, by the accumulating effects of magnetic perturbations at scales $\ll r_L$, by the magnetic field geometric structure at scales $\gg r_L$, and by the strong resonant effects on geometric features at scale $\approx r_L$. The LIMF is found to be coherent within approximately 60 parsec [35]. This means that CRs approach the heliosphere from the ISM spiraling around the LIMF lines with pitch angle distribution reflecting their propagation history. At 1-TV rigidity scale, it is, therefore, expected that the heliosphere, with its approximately gyro-scale magnetic instabilities, has the power to redistribute CRs.

The strong heliospheric influence on the arrival direction distribution of CR particles is shown in Figures 4.6 and 4.7, where a large fraction of the particles passing through the heliosphere is redistributed in pitch angle by multiple scattering in the magnetic instabilities. While the global anisotropy may still be ordered by the LIMF, the medium- and small-scale features depend on the peculiar properties of the heliospheric magnetic field. In the 1-TV rigidity scale, where resonant scattering processes are more dominant, particles are severely redistributed, and this results in a relatively smoother distribution. On the contrary, in the 10-TV rigidity scale, scattering processes are still significant, but the large scale average magnetic field induces the formation of medium- and small-scale structures.

In other words, the heliosphere acts as a *diffusor* where particles with gyroradius $r_L \approx$

$L_{\text{instabilities}} \approx 10 - 100$ AU are more stochastically influenced via resonant multiple scattering than those with $r_L \gtrsim L_{\text{heliosphere}} \approx 600$ AU. A consequence of violation of magnetic moment conservation (see Figure 4.5) is that an initially uniform pitch angle distribution becomes more structured with most of the energy stored in the large angular scales. The lower the effect of stochastic redistribution from scattering, the higher the contribution from small angular scale structures, as shown in Figure 4.8. It is likely that the largest angular scale, such as dipole and quadrupole, are affected by these scattering processes as well. However, in this work, such an effect is not explicitly assessed, since particles need to be propagated much closer to Earth.

Statistically uncorrelated data sets can produce sky maps that have similar features; nonetheless, they will not be identical since these scattering processes are stochastic by nature. These sky maps may look different but they share the same angular power spectrum, since it encloses the global statistical properties of the ensemble, and not the specific spatial locations of the maps' features. Consequently, the physically relevant quantity is the angular power spectrum.

The energy transfer between angular scales is different from that studied in LX16, where the effect of turbulence on a back-propagated particle distribution was considered. In that case, the particle gyroradius r_L was always smaller than the largest scale of magnetic turbulence. Therefore, as long as $r_L < L_{\text{injection}}$, particles are always in resonance with a given turbulence scale, the largest scale conveying more power than smaller scales. The energy of an initially dipolar pitch angle distribution is more rapidly transferred into smaller angular scales at higher energy, because resonant scattering occurs on higher power turbulence scales. In both studies, LX16 and this work, it is found that magnetic scattering generates flatter power angular spectra at higher rigidity scales. In general, if scattering is sufficiently strong, it is possible to form small-scale features within a relatively short distance scale as well. In the heliospheric model used in the present study, the size and location of the magnetic instabilities mostly influence 1 TV-scale particles, especially those propagating from downstream of the interstellar wind, i.e., in closer proximity to the elongated tail. It is important to note that

other heliospheric properties, not accounted for in the model used here, may significantly increase the scattering rate at a specific rigidity range. The 11-year solar magnetic field inversion cycle generates pockets of magnetic polarity dragged outward and along the heliotail by solar wind [65]. The size of those regions is approximately 200-300 AU, as discussed in DL13, which resonate with particles with a rigidity of a few TV. Since the geometry of such polarity regions is different than that of magnetic instabilities, the effect can account for different distributions. This effect was not considered in the present study and will be the subject of a followup project.

One carefully studied possibility is that the nonconservation of the magnetic moment discussed in Section 4.4 may result from poor accuracy of the trajectory interaction code used. The numerical algorithm used to integrate particle trajectories in this study is the same used in LX16, in the study of MHD turbulence effect of the particle distribution. As extensively discussed in LX16, the Bulirsch-Stoer numerical integration method used is considered one of the best known algorithms satisfying both high accuracy and efficiency [68] and widely applied in the literature [40, 78]. Although this integration method is not symplectic, i.e. it does not have a bound on the global error (see [108]) which can then be accumulated at each integration step [86], it was found, in this study, that the accuracy is still very high (as discussed in the appendix of LX16). The accuracy of the numerical integration is controlled by monitoring the local truncation error estimated at each time step. If the relative error is larger than the relative tolerance level of 10^{-6}, the step size is adaptively reduced in order to limit the error accumulation in both momentum and spatial coordinates, across the maximum integration time used in this study (between 10,000 and 100,000 gyrations). The accuracy in momentum coordinates was tested, and the resulting energy conservation was found to be constrained well within 10^{-5} (see LX16). Due to the adaptive step size, the accuracy in spatial coordinates is $\ll r_L$, thus limiting numerical diffusion to an undetectable level. In LX16, the violation of magnetic moment was not statistically relevant (and therefore the back-propagation method was utilized), while in the current heliospheric study it is dramatically significant. The difference between the two cases is in the magnetic field used.

The numerical accuracy of the trajectory integration method is the same.

The magnetic field interpolation via 3D cubic spline functions does not appear to reduce numerical accuracy. In general, it is known that a straightforward interpolation of magnetic fields may be not divergence-free, while the calculation of vector potential via Fourier transforms and its interpolation does produce well behaved magnetic fields. The two different interpolation strategies may influence the particle integrated trajectories, and in particular the first adiabatic invariant [86]. However, in the present problem, although the heliospheric magnetic field has instabilities, there are no cusps that may produce significant discontinuities in the interpolated fieldlines. In addition, the cubic spline interpolation used in this work requires continuity of the second derivative in the entire domain. Therefore, it is not expected that a divergence-free interpolation strategy would significantly change the results.

As described in LX16, it is possible to exclude with confidence that the particle trajectory integration method used in this study can induce chaotic behavior as a result of poor accuracy. Therefore it is the opinion of the authors that the effective collisional behavior found in this case is due to the properties of the heliospheric magnetic field used.

To conclude, the study presented in this work explores the effects of the heliosphere on multi-TeV CR arrival direction distribution. The results illustrate the importance of particle rigidity, E/Ze, in making it possible that the heliospheric influence stretches across a relatively wide CR particle energy range. For the particular model of the heliosphere by [95] (described in Section 4.3.1), resonant scattering processes are strong enough to break adiabaticity and generate stochastic pitch angle distributions. As a consequence, Liouville's theorem could not be applied and a computationally expensive forward propagation technique was used. The escape of particles due to magnetic bottle mirroring and multiple resonant scattering generates a rigidity-dependent complex arrival distribution of CR particles that comprises a wide power spectrum in angular structures. In order to reproduce the observations, proper consideration must be given to a wider range in rigidity accounting for the actual spectrum and composition of the CRs, especially taking into account that the precise features are not exactly reproducible given the stochastic process at the heliospheric boundary, and an

angular power spectrum approach should be taken in order to study the CR-arrival anisotropy. Assuming that the dipole component of the observed CR anisotropy is the imprint of diffusion in the ISM, the study of the complex angular structure can provide important hints as to the turbulent properties of the ISM (especially at energies > 100 TeV, as shown in LX16) and to the properties of the heliosphere (in the TeV energy range).

4.7 Summary

The main results can be summarized as follows:

- As CRs are strongly affected by magnetic structures on the order of their gyroradius, multi-TeV particles are subject to significant heliospheric scattering. This redistributes CRs and affects their arrival direction distribution. Our work shows that this scattering can have a significant effect.

- Our simulations show significant resonant scattering of the CRs by the heliosphere. Therefore, the conditions of Liouville's theorem are not satisfied and the backward-propagation technique cannot be used to study CR anisotropies arising from the interaction of heliospheric magnetic fields with CRs.

- Our study of the effect of the heliosphere on CR anisotropy, which we performed using the forward-propagation techniques, demonstrates the following features:

  - Results for protons: The heliosphere has a strong effect in redistributing CRs at the 1 TV rigidity scale. Multiple scattering with stochastic pitch angle redistribution is relevant, and anisotropy arises even without assuming any weight in the initial arrival distribution of CR particles. The scattering effect is weaker at the 10 TV rigidity scale but is still important in producing small- to medium-angular scale features that contribute to the overall arrival direction distribution.

– Results for heavy nuclei: At 10 TeV, the flux of helium nuclei starts to become dominant, while heavy nuclei contribute to about a third of the total flux [38]. We found that high-energy heavy nuclei have an important role in shaping the observed anisotropy at very small angular scales (i.e., multipole moments $\ell = $ 7-25). This also means that the heliospheric influence affects observed anisotropies over a wide energy range.

• Our study calls for both more extensive observations of CR anisotropies and more detailed numerical testing using high-resolution models of the heliosphere. Future research should also take into account the significant time variations of the heliospheric magnetic field related to both the 11-year cycle and dynamical instabilities on the longer time scales.
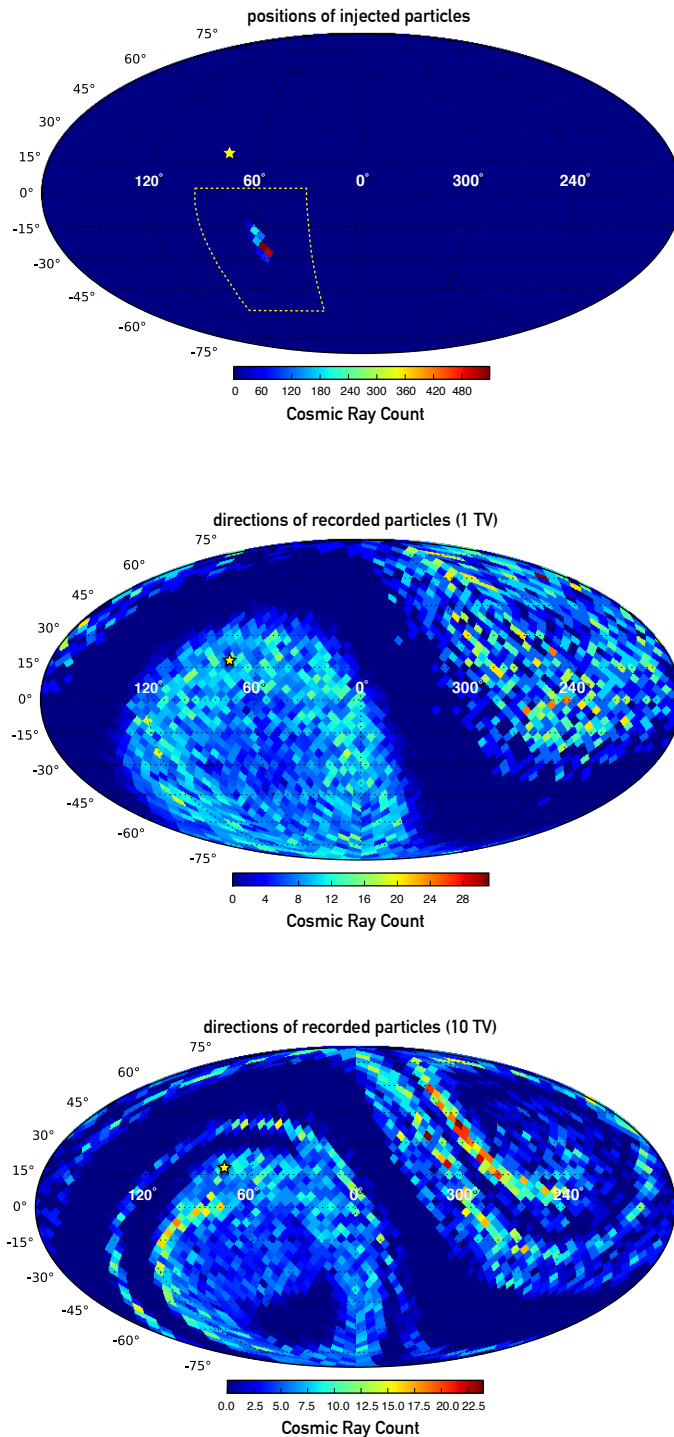
Figure 4.6: *Top:* Map in equatorial coordinates of the positions of injected particles (from the 60°×60° region of the heliosphere upstream of the ISM flow). Only the initial positions of those particles that are actually recorded are shown here. *Center:* Map in equatorial coordinates of the arrival direction distribution of the recorded mixed composition particles at rigidity scale of 1 TV. *Bottom:* Map in equatorial coordinates of the arrival direction distribution of the recorded mixed composition particles at rigidity scale of 10 TV. The yellow star indicates the approximate position of the heliospheric tail. The dashed yellow box corresponds approximately with the region of initial position of all the particles.
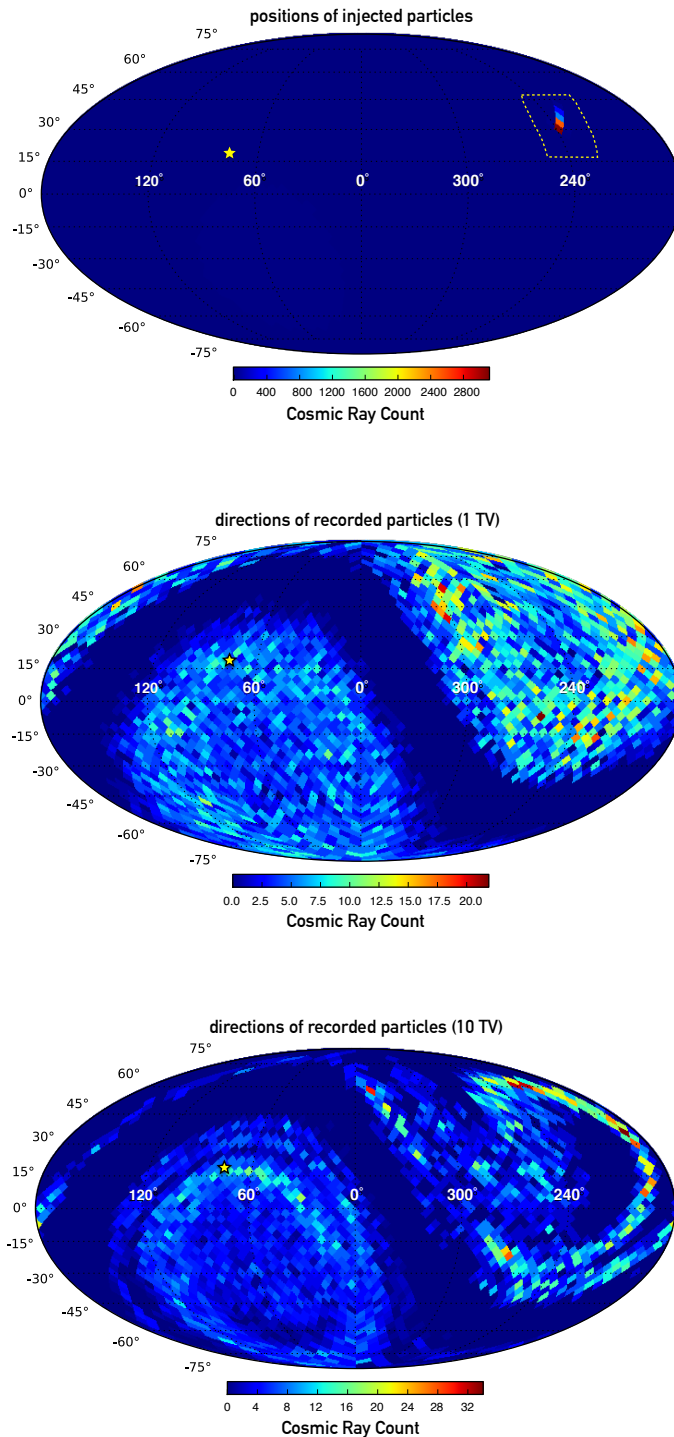
Figure 4.7: *Top:* Map in equatorial coordinates of the positions of injected particles (from the 30°×30° zone of the heliosphere downstream of interstellar side, in proximity of the heliotail). Only the initial positions of those particles that are actually recorded are shown here. *Center:* Map in equatorial coordinates of the arrival direction distribution of the recorded mixed composition particles at rigidity scale of 1 TV. *Bottom:* Map in equatorial coordinates of the arrival direction distribution of the recorded mixed composition particles at rigidity scale of 10 TV. The yellow star indicates the approximate position of the heliospheric tail. The dashed yellow box corresponds approximately with the region of initial position of all the particles.
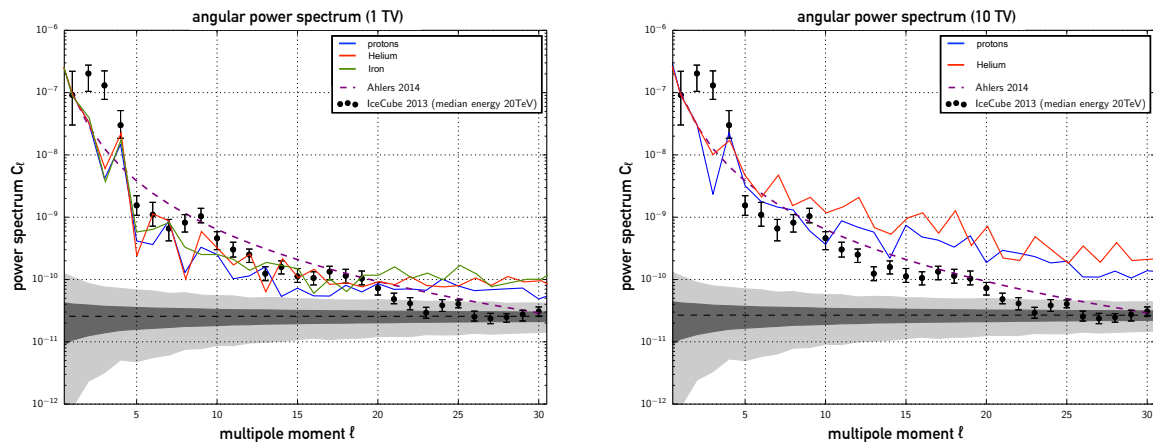
Figure 4.8: Angular power spectrum of the arrival direction distribution on the target sphere of the 1-TV rigidity particle sets (on the left) and of the 10-TV rigidity particle sets (on the right). Protons (blue lines), helium nuclei (red lines), and iron nuclei (green line) are separately shown. The gray bands show the 1σ and 2σ bands for a large set of isotropic sky maps. The black circles are the results from the IceCube Observatory at a median energy of 20 TeV [71, 2]. The dashed purple line is the power spectrum from [10]. The angular power spectrum results are normalized to the IceCube experimental results at the dipole component ($\ell = 1$). Note that the angular power spectra are calculated with all particles initiated from both regions on the injection sphere.

Bibliography

[1] Aartsen, M. et al. 2013b, Astrophys. J. 765, 55

[2] Aartsen, M. et al. 2016, accepted for publication on ApJ

[3] Abbasi, R. et al. 2010a, Astrophys. J. 718, L194

[4] Abbasi, R. et al. 2011a, Astrophys. J. 740 16

[5] Abbasi et al. 2012b, Astrophys. J. 746, 33

[6] Abdo, A.A. et al. 2008, Phys. Rev. Lett. 101, 221 101

[7] Abdo, A.A. et al. 2009, Astrophys. J. 698, 2121

[8] Abeysekara, A.U. et al. 2014, Astrophys. J. 796, 108

[9] Aglietta, M. et al. 2009, Astrophys. J. 692, L130

[10] Ahlers, M. 2014 Phys. Rev. Lett. 112, 021101

[11] Ahlers, M. et al. 2016, ApJ 823, 10

[12] Ahlers, M. 2016 arXiv:1605.06446

[11] Ahlers, M., & Mertsch, P. 2015, arXiv:1506.05488

[12] Amenomori, M. et al. 2005, Astrophys. J. Lett. 626, L29

[13] Amenomori, M. et al. 2006, Science, 314, 439

[14] Amenomori, M. et al. 2011, Proc. 32nd ICRC, Beijing China

[15] Amenomori, M. et al. 2007, Proc. 30th ICRC, Mérida, Mexico

[18] Avinash, K., Zank, G. P., Dasgupta, B., Bhadoria, S. 2014, Astrophys. J. , 791, 102

[16] Bartoli, B., et al. 2013, Phys. Rev. D 88-8, 082001

[17] Bartoli, B., et al. 2015, Astrophys. J. 809, 90

[18] Baumjohann, W. & Treumann, R. A. 1996, Plasma Physics, Magnetohydrodynamics, Kinematics, Radiative Transfer, London: Imperial College Press

[22] Belov, N. A, & Ruderman, M. S. 2010, MNRAS, 401, 607

[19] Beresnyak, A., Yan, H., & Lazarian, A. 2011, Astrophys. J. 728, 60, 8 pp.

[20] Biermann, P.L., Becker Tjus, J., Seo, E.-S., & Mandelartz, M. 2013, Astrophys. J. 768, 124

[21] Blasi, P., & Amato, E. 2012, JCAP 1, 11

[26] Borovikov, S. N., et al. 2008, Astrophys. J. 682, 1404

[27] Borovikov, S. N., Pogorelov, N. V. 2014, Astrophys. J. , 783, LX16

[22] Bradt, H. 2008, Astrophysics processes, Cambridge Univ. Press, Cambridge

[23] Bradt, H. 2008, in Astrophysics Process (Cambridge, (supplement): Cambridge Univ. Press)

[30] Brandenburg, A. & Lazarian, A. Space Sci Rev (2013) 178: 163.

[24] Burkhart, B. et al. 2014, Astrophys. J. 790 130

[32] Cesarsky, C. J. 1980, ARA&A, 18, 289

[33] Chalov, S. V. 1996, AAP, 308, 995

[34] Chandran, B. D. G. 2000, PhRvL, 85, 4656

[25] Cho, J., & Lazarian, A. 2002, Phys. Rev. Lett. 88, 245001

[36] Cho, J., & Lazarian, A. 2003, MNRAS, 345, 325

[26] de Jong, J. et al. 2011, Proc. 32nd ICRC, Beijing, China

[27] Desiati, P. & Lazarian, A. 2012, NPG 19, 351

[28] Desiati, P. & Lazarian, A. 2013, Astrophys. J. 762, 44

[29] Desiati, P. & Zweibel, E.G. 2014, Astrophys. J. 791, 51

[41] Drake, J. F., Swisdak, M., Che, H., & Shay, M. A. 2006, Nature, 443, 553

[42] Drake, J. F., Opher, M., Swisdak, M., & Chamoun, J. N. 2010, ApJ, 709, 963

[31] Effenberger, F. et al. 2012, A&A 547, A120

[32] Erlykin A.D., & Wolfendale A.W. 2006, Astropart. Phys. 25, 183

[45] Farmer, A. J., & Goldreich, P. 2004, ApJ, 604, 671

[46] Florinski, V., Zank, G. P., & Pogorelov, N. V. 2005, J. of Geophys. Res. (Space Physics), 110, 7104

[33] Florinski, V, Jokipii, J. R., Alouani-Bibi, F., le Roux, J. A. 2013, Astrophys. J. 776, L37

[34] Florinski, V., Stone, E.C., Cummings, A.C., & le Roux, J.A. 2015, Astrophys. J. 803 47

[35] Frisch, P.C. et al. 2012 Astrophys. J. 760, 106

[36] Frisch, P.C. 2015 J. Phys.: Conf. Ser. 577, 012010

[37] B. M. Gaensler, et al. 2011, Nature 478, 214

[38] Gaisser, T.K., Stanev, T. & Tilav, S. 2013 Front. of Phys. 8-6, 748

[53] Galtier, S., Nazarenko, S. V., Newell, A. C., & Pouquet, A. 2000, Journal of Plasma Physics, 63, 447

[39] Giacinti, G., & Sigl, G., 2012 Phys. Rev. Lett. 109, 071101

[40] Giacalone, J. & Jokipii, J.R. 1999, Astrophys. J. 520, 204

[41] Goldreich, P., & Sridhar, S. 1995, Astrophys. J. 438, 763

[42] Goldstein, H., Poole, C., & Safko, J. 2002, Classical Mechanics (3rd ed.; San Francisco, CA: Addison-Wesley)

[43] Gorski, K. M., Hivon, E., Banday, A. J., et al. 2005, ApJ, 622, 759

[59] de Gouveia dal Pino, E. M. & Lazarian, A. 2005, A&A, 441, 845.

[44] Guillian, G. et al. 2007, Phys. Rev. D 75, 062003

[45] Hall, D.L. et al. 1999, J. of Geophys. Res. 104, 6737

[46] Haverkorn, B., et al. 2008, Astrophys. J. 680, 362

[63] Izmodenov, V. V., Alexashov, D. B. 2003, Astronomy Lett., 29, 58

[64] Kozai et al. 2014, Earth, Planets and Space 66, 151

[65] Kowal, G. et al. 2009, Astrophys. J. 700, 63

[66] Kowal, G. et al. 2012, Nonlinear Processes in Geophysics, 19, 297

[47] Kumar, R., & Eichler, D. 2014 Astrophys. J. 785, 129

[48] Jansson, R., & Farrar, G.R. 2012a, Astrophys. J. 757, 14

[49] Jansson, R., & Farrar, G.R. 2012b, Astrophys. J. 761, L11

[50] Jokipii, J.R. 1966, Astrophys. J. 146, 480

[51] Jokipii, J.R. & Parker, E.N. 1969, Astrophys. J. 155, 777

[72] Lazarian, A. 2005, in AIP Conf. Proc. 784, Magnetic Fields in the universe: From Laboratory and Stars to Primordial Structures (Melville, NY: AIP), 42

[52] Lazarian A., 2006 AIPC, 874, 301

[53] Lazarian, A. 2007, J. Quant. Spectros. & Radia. Transfer 106, 225

[75] Lazarian, A. 2016, arXiv:1607.02042

[76] Lazarian, A., & Beresnyak, A. 2006, MNRAS, 373, 1195

[54] Lazarian, A. & Desiati, P. 2010, Astrophys. J. 722, 188

[78] Lazarian, A., & Opher, M. 2009, ApJ, 703, 8

[55] Lazarian, A., & Vishniac, E.T. 1999, Astrophys. J. 517, 700

[80] Lazarian, A., & Yan, H. 2014, ApJ, 784, 38

[81] Lazarian, A., Eyink, G., Vishniac, E., & Kowal, G. 2015, RSPTA, 373, 40144

[58] Lithwick, Y., & Goldreich, P. 2001 Astrophys. J. 562, 279

[83] Liewer, P. C., Karmesin, S. R., & Brackbill, J. U. 1996, J. of Geophys. Res., 101, 17119

[84] Longair, M. 2011, High Energy Astrophysics (3rd ed.; Cambridge: Cambridge Univ. Press)

[85] López-Barquero, V. et al. 2016, Astrophys. J. , 830, 19

[86] Mackay, F., Marchand, R. & Kabin, K. 2006, Journal of Geophysical Research (Space Physics) 111, A06205

[60] Mertsch, P. & Funk, S. 2015 Phys. Rev. Lett. 114, 021101

[61] Minnie, J., et al. 2009, JGR 114, A01102

[62] Munakata, K. et al. 2010, Astrophys. J. 712, 1100

[63] Nagashima, et al. 1998, J. of Geophys. Res. 1031, 17429

[64] Manuel, R., Ferreira, S., & Potgieter, M. 2014, Solar Physics 289, 2207

[92] Opher, M., Drake, J. F., Zieger, B., Gombosi, T. I. 2015, Astrophys. J. , 800, 28

[65] Pogorelov, N.V., Zank, G.P., & Ogino, T. 2006, Astrophys. J. 644, 1299

[94] Pogorelov, N.V., Suess, S.T., & Borovikov, S.N. 2013, Astrophys. J. 772, 2

[95] Pogorelov, N.V., et al. 2015, Astrophys. J. Lett. 812, L6

[96] Pogorelov, N. V., Borovikov, S. N., Heerikhuisen, J., Zhang, M. 2015, Astrophys. J. , 812, L6

[97] Pogorelov, N. V. 2016, J. Phys. Conf. Ser., 719, 012013

[98] Potgieter, M. 2013, Living Rev. in Solar Phys. 10, 3

[66] Pohl, M. & Eichler, D. 2013, Astrophys. J. 766, 9

[68] Press, W.H., Flannery, B.P., & Teukolsky, S.A. 1986, Cambridge: University Press, 1986

[67] Ptuskin V. 2012, Astropart. Phys. 39, 44

[69] Rechester, A.B. & Rosenbluth, M.N. 1978, Phys Rev Lett 40, 38

[70] Rettig, R. & Pohl, M. 2015, in Proc. of 34th ICRC, The Hague, The Netherland

[104] Roberts, P. H. 1956, Astrophys. J. , 124, 430

[105] Ruderman, M. S., & Belov, N. A. 2010, J. Phys. Conf. Ser., 216, 012016

[106] Ruderman, M. S., Fahr, H. J. 1995, AAP, 299, 258

[71] Santander, M. et al. 2013, in Proc. of 33rd ICRC, Rio de Janeiro, Brazil; arXiv:1309.7006

[108] Sanz-Serna, J. M & Calvo, M. P 1994, Numerical Hamiltonian problems, 1st ed, Chapman & Hall, London ; New York

[72] Savchenko, V., Kachelrieß, M. & Semikoz, D.V. 2015, DOI:10.1088/2041-8205/809/2/L23

[110] Scherer K. et al. 2016, Astrop. Phys. 82, 93.

[73] Shuwang, C. et al. 2011, Proc. 32nd ICRC, Beijing China

[112] Shaikh, D., & Zank, G. P. 2010, Phys. Lett. A, 374, 4538

[74] Shalchi, A. 2009 Nonlinear Cosmic Ray Diffusion Theories, ASSL 362 (Springer)

[75] Schwadron, N.A., Adams, F.C., Christian, E.R., Desiati, P., Frisch, P., Funsten, H.O., Jokipii, J.R., McComas, D.J., Moebius, E., Zank, G.P. 2014, Science 343, 988

[76] Sridhar, S., & Goldreich, P. 1994, Astrophys. J. 432, 612

[77] Sveshnikova, L.G. et al. 2013, Astropart. Phys. 50, 33

[117] Wiedemann, H. 2015, Particle Accelerator Physics (Springer)

[78] Xu, S., & Yan, H. 2013, Astrophys. J. 779, 140

[119] Yan, H., & Lazarian, A. 2002, PRL, 89, 281102

[79] Yan, H., & Lazarian, A. 2008, Astrophys. J. 673, 942

[80] Yan, H., & Lazarian, A. 2011, Astrophys. J. 731, Issue 1, article id. 35, 10 pp. (2011)

[122] Yu, G. 1974, Astrophys. J. , 194, 187

[81] Zhang, J.L. et al. 2009, Proc. 31st ICRC, Łódź, Poland

[82] Zhang, M., Zuo, P., & Pogorelov, N. 2014, Astrophys. J. 790, 5

[125] Zank, G. P. et al. 1996, J. of Geophys. Res., 101, 21639

[126] Zank, G. P. 1999, in AIP Conf. Ser. 471, Solar Wind 9, ed. S. R. Habbal et al. (Melville, NY: AIP), 783

[127] Zank, G. P. et al. 2009, Sp. Sci. Rev. 146, 295

[128] Zank, G. P., Heerikhuisen, J., Wood, B. E., et al. 2013, Astrophys. J. , 763, 20

Chapter 5

Cosmic Ray Anisotropy from Local Turbulent Magnetic Fields

*Does anisotropy arise from the CR propagation in the turbulent
interstellar magnetic fields?*

Cosmic ray anisotropy has been observed in a wide energy range and at different angular scales by a variety of experiments over the past decade. However, no comprehensive or satisfactory explanation has been put forth to date. The arrival distribution of cosmic rays at Earth is the convolution of the distribution of their sources and of the effects of geometry and properties of the magnetic field through which particles propagate. It is generally believed that the anisotropy topology at the largest angular scale is adiabatically shaped by diffusion in the structured interstellar magnetic field. On the contrary, the medium- and small-scale angular structure could be an effect of nondiffusive propagation of cosmic rays in perturbed magnetic fields. In particular, a possible explanation of the observed small-scale anisotropy observed at TeV energy scale, may come from the effect of particle scattering in turbulent magnetized plasmas. We perform numerical integration of test particle trajectories in low-β compressible magnetohydrodynamic turbulence to study how the cosmic rays arrival direction distribution is perturbed when they stream along the local turbulent magnetic field. We utilize Liouville's theorem for obtaining the anisotropy at Earth and provide the

theoretical framework for the application of the theorem in the specific case of cosmic ray arrival distribution. In this work, we discuss the effects on the anisotropy arising from propagation in this inhomogeneous and turbulent interstellar magnetic field.

A version of this chapter has previously appeared in The Astrophysical Journal. López-Barquero, V., Farber, R., Xu, S., et al. 2016, ApJ, 830, 19.

5.1 Introduction

Cosmic rays are found to possess a small but measurable anisotropy in their arrival direction distribution at Earth. The origin of the observed anisotropy is not yet understood. However, it is reasonable to assume that it is a combination of effects correlated to the distribution of the galactic sources of cosmic rays, the geometry and turbulence properties of the galactic magnetic field, and the propagation in interstellar magnetized plasmas. These are likely to be responsible for the complex shape of the energy spectrum as well [38]. Since we don't know the locations of cosmic ray sources and we lack details of the interstellar magnetic field, understanding these observations of anisotropy is not an easy task.

Above the energy range where cosmic rays are directly affected by inner heliospheric processes (see, e.g., [33, 64, 34]), a statistically significant anisotropy has been observed by a variety of experiments, sensitive to different energy ranges (from tens of GeV to a few PeV), located on or below the Earth's surface in the Northern Hemisphere [63, 45, 12, 13, 44, 7, 9, 81, 62, 14, 26, 73, 17] and in the Southern Hemisphere [3, 4, 5, 1].

The global anisotropy changes with energy in a non-trivial fashion. From about 100 GeV to tens of TeV, it has been observed to have an approximately consistent structure at the largest scale, although its amplitude appears to increase with energy. Above a few tens of TeV, the observed progressive change in the anisotropy topology may indicate a transition between two processes shaping the particles' arrival distribution at Earth. The observation could be qualitatively explained on the basis of diffusive propagation of cosmic rays in the Milky Way from stochastically distributed sources, responsible for generating a gradient in

cosmic ray density.

Numerical studies of particle propagation in a scenario of homogeneous and isotropic diffusion in the Galaxy predicts that the cosmic ray density gradient, and the consequent induced anisotropy, has a dipole shape with direction toward the source of the particle and with amplitude that directly depends on the diffusion coefficient. In particular, for a given realization of galactic source spatial distribution, the dipole anisotropy would point toward the source with the largest contribution [32, 21, 67, 66, 77, 72], which may change with energy, in agreement with observations. On the other hand, the systematic overestimation of the anisotropy amplitude may be partially compensated by the fact that diffusion is expected to be anisotropic (see, e.g., [31]), thus modifying the expected cosmic ray density gradient shape as a function of the source direction with respect to the regular galactic magnetic field [47]. The misalignment between the cosmic ray density gradient and the regular galactic magnetic field would prevent pointing to any specific source, and it would suppress the anisotropy amplitude to a value closer to what has been observed [60].

Another scenario is that it is the transition from heliospheric- to interstellar-dominated contributions, starting at a 10 TeV energy scale and culminating around 100-200 TeV, at the origin of the shift in anisotropy. In [28], this scenario was proposed noting that 10 TeV protons have an average gyroradius, in a μG scale magnetic field, on the order of the thickness of the heliosphere (see, e.g., [65]). In addition, the dynamical instabilities of the heliospheric magnetized plasma at smaller scales may generate strong scattering that redistributes the arrival direction of TeV cosmic rays. This heliospheric scenario is studied and presented in our companion paper [59]. Such strong scattering may be able to produce large localized particle gradients, experimentally interpreted as medium- or small-scale anisotropy. In [75], a scenario of weak influence of the heliospheric magnetic field on TeV protons was explored, thus interpreting the observations as directly related to the ordering of the local interstellar magnetic field (see also [82]).

The anisotropy appears to possess a complex angular structure with evidence of a harder cosmic ray spectrum within the localized excess region in the apparent direction of the

heliospheric tail [15, 6, 16, 8]. The decomposition of TeV cosmic ray anisotropy in the individual spherical harmonic contributions shows that the arrival direction distribution is dominated by large-scale structures (such as, e.g., dipole and quadrupole) with a relative intensity on the order of 10^{-3}, but that medium- and small-scale angular structures are significantly contributing with relative intensities below 10^{-4}.

The experimental determination of small angular scale anisotropy is generally performed by filtering out the large-scale modulations from the observed arrival direction distribution, thus retaining all structures with large angular gradients. Some of the small-scale anisotropy features seem to be correlated to regions in the sky where the global anisotropy has large variations (see [28]) or may be an effect of re-acceleration by magnetic reconnection processes in the tail of the heliosphere [54, 27]. However, globally, the observed small scale anisotropy may appear to be rather randomly structured and, therefore, possibly a natural consequence of cosmic ray propagation in the local turbulent magnetic field in the presence of a global anisotropy [39]. The global anisotropy, at all angular scales, arises from the same physical processes, thus it is impossible to disentangle its origin. However, as a first approximation, it is generally assumed that the anisotropy at the largest scale is dominated by global physical processes (such as a density gradient from sources of cosmic rays or from convective effects originated by large-scale cumulative stellar winds, and from propagation through the regular galactic magnetic field), while the small angular scales are dominated by local processes.

A complex angular power spectrum is asymptotically generated by progressive decomposition of the energy of an initial anisotropy distribution (for instance a dipole) into higher multipoles, by the effect of scattering off magnetic turbulence [10, 11]. The conservation of phase space density, as stated by Liouville's theorem, predicts, for an idealized situation of a homogenous large-scale anisotropy, the total sum of the multipoles' angular terms is conserved. This makes it possible to generate small-scale structures, as shown in [10].

Turbulence in astrophysical plasmas have significant effects on particle propagation, in that the stochastic nature of magnetic field lines is transmitted to the particles' trajectories. If particles are tied to magnetic field lines, the maximum perpendicular diffusion rate is set

by the rate of perpendicular field line wandering, scaled by particle velocity (field line random walk). This has been extensively discussed by, e.g. [50, 51, 69, 40, 61, 74] in the context of diffusion at distance scale larger than the turbulence injection scale. On scales smaller than the injection scale, particles are characterized by super-diffusion in the perpendicular direction of the mean magnetic field. This behavior is described by the so-called Richardson diffusion, where particle separation grows as $(\text{time})^{3/2}$ [56]. In [30] it was shown that this is directly connected to the separation of turbulent magnetic field lines, which grows as $(\text{distance})^{3/2}$ [55]. In this case, the stochastic nature of the astrophysical magnetic fields (such as, e.g. the interstellar magnetic field, or, at larger scales, the intercluster magnetic field), inevitably produces chaotic particle trajectories, meaning that the geometry of particle trajectories is highly sensitive to the actual initial conditions. Diffusion by magnetic field line wandering is found to be a dominant contribution and stronger than the extreme case of Bohm diffusion, where scattering frequency is one per particle gyration. The important aspect that determines the properties of a large ensemble of particles is its statistical nature, which in this case is influenced by the properties of the magnetic field and specifically by the induced scattering rate. While individual trajectories may have chaotic properties and are, therefore, practically/realistically unpredictable, the large ensemble of particles can still be deterministically described. For these reasons, the recorded spatial distribution of the ensemble will be statistically determined and a direct consequence of the properties of the turbulent magnetic field. In this work, a study of particle propagation in compressible magnetohydrodynamics (MHD) turbulence is performed in the context of its effects on arrival direction distribution.

In addition, depending on the degree to which magnetic field lines diverge on scales less than the particle gyroradius, pitch angle scattering on small-scale magnetic perturbations affects particle distribution at the large spatial scale, thus increasing the diffusion coefficient depending on the large geometrical scale of the magnetic field turbulence (see, e.g., [29] and references therein). The anisotropic nature of interstellar turbulence and the properties of turbulence itself can significantly complicate the description of cosmic ray transport (see,

e.g., [79, 80, 19]).

This paper is organized as follows. In section 5.2, we describe the turbulent magnetic field used and the test particle trajectory integration. In section 5.3, we discuss the validity of applying Liouville's theorem in the context of this work by statistically assessing the level of conservation of magnetic moment. The results of the study are presented in section 5.4 and discussed in section 5.5. Concluding remarks follow in section 5.6.

5.2 Cosmic ray Propagation in Turbulent Magnetic Fields

Cosmic rays, which are accelerated in their sources and "injected" into the interstellar medium (ISM), are free to propagate through the interstellar magnetic field. Globally, the galactic magnetic field is characterized by a large-scale regular component and a small-scale random component (see, e.g., [48, 49]). The regular component can be described as a superposition of spiral and toroidal structures, possibly with a contribution perpendicular to the galactic plane, and the random component represents the stochastic perturbations of the regular field caused by the dynamics of the galaxy and its density distribution. An important property of the interstellar magnetic field is turbulence. A variety of observations show that the coherence scale of turbulent magnetic fields is on the order of 10 pc in spiral arm regions (with more frequent stellar formation activity) and on the order of 100 pc in the interarm regions [46]. The injection scale of turbulence is determined by the scale at which the magnetic perturbation is generated (for instance, by stellar collapse or binary mergers).

Astrophysical plasmas are typically highly ionized and have high Reynolds numbers, thus the dynamics of the flow is dominated by nonlinear convective processes at the largest scale. In such conditions, turbulence develops and magnetized Alfvénic eddies dynamically cascade to smaller scales and progressively elongate along the magnetic field lines, as initially proposed by [76, 41] (see also [53] for a review). This model of incompressible MHD turbulence predicts

a Kolmogorov-type energy power spectrum $E(k_\perp) \propto k_\perp^{-5/3}$ in terms of the wave-vector component perpendicular to the local direction of the magnetic field, while the parallel component of the wave vector is $k_\parallel = k_\perp^{2/3}$. In those pioneering papers, the theory assumes the injection of energy at scale L and the injection velocity equal to the Alfvén velocity in the fluid V_A, i.e., the Alfvén Mach number $M_A \equiv (V_L/V_A) = 1$ (i.e., trans-Alfvénic turbulence), where V_L is the plasma velocity at injection scale L. The model was later generalized for both sub-Alfvénic (i.e., $M_A < 1$) and super-Alfvénic (i.e., $M_A > 1$) cases [55, 52] (see also [57, 24]). Typically, the ISM is characterized by $M_A \lesssim 1$ [37].This means that magnetic field lines do not typically fluctuate too far from the mean direction.

While the model by [41] describes incompressible MHD turbulence, modeling compressible turbulence turned out to be more complex. In isothermal plasmas, there are three types of MHD waves: Alfvén, slow, and fast waves. Alfvén modes are incompressible, while slow and fast modes are compressible. The compressible modes are conjectured to resemble incompressible behavior at high-β (i.e., high gas to magnetic pressure ratio) [58]; however, ISM plasmas are typically characterized by low-β. [25] investigated the scaling properties of low-β compressible sub-Alfvénic MHD turbulence and confirmed that slow compressible modes behave as the Alfvén incompressible modes but also that the fast modes are isotropic, since their velocity does not depend on magnetic field direction.

The spatial distribution of particles propagating in a turbulent field is affected by the magnetic perturbations within the particle autocorrelation length scale (or mean free path). To study the correlation between turbulence and cosmic ray distribution, trajectories of test particles were integrated in an MHD turbulent magnetic field. The methodology used is described in the next two sections.

5.2.1   Turbulent Magnetic Field

Test particle trajectories are integrated in a compressible sub-Alfvénic isothermal MHD turbulence in low-β based on numerical calculations developed by [25]. In the model,

turbulence is driven solenoidally in Fourier space, setting the velocity and density fields initially to unity. The calculation is performed in a cube with side $L_{box} = 512$ grid-points, with inertial range from $L_{inj} = 204.8$ grid-points (i.e., $0.4 \times L_{box}$) down to a "damping" scale of $L_{min} = 5$ grid-points.

The average magnetic field is directed along the x-axis and turbulence is characterized by a gas-to-magnetic pressure value of $\beta \sim 0.2$ and by Alfvénic Mach number $M_A = 0.773$. Such a Mach number corresponds to the fluctuations being on the order of the mean magnetic field at the injection scale, which is in agreement with what we would have expected from the local ISM. The external mean magnetic field is the only controlled parameter in this MHD model.

5.2.2 Cosmic Ray Propagation

The analysis is performed by integrating proton trajectories in a static magnetic field, using the set of 6-dimensional ordinary differential equations

$$\frac{d\vec{p}}{dt} = q\left(\vec{u} \times \vec{B}\right) \tag{5.1}$$

$$\frac{d\vec{r}}{dt} = \vec{u}, \tag{5.2}$$

describing the Lorentz force and the particle velocity $\vec{u}$, where $\vec{r}$ is the particle position vector and $\vec{p}$ the momemtum. For $\vec{B}$, we use one steady state realization of the magnetic field described in section 5.2.1. The equations are integrated using the Bulirsch-Stoer integration method with adaptive time step. At each integration step, the magnetic field is interpolated using a 3D cubic spline, and integration is stopped when particles cross the border of the MHD simulation box. The accuracy of the particle trajectory integration for this study was assessed and is discussed in Appendix A.1. The choice of one specific realization of the magnetic field is justified by the fact that particle velocity is much larger than the plasma Alfvén velocity, thus induced electric fields can be neglected.

Table 5.1: Physics parameters of simulation sets

Set	E_p	r_L	L_{inj}	L_{mfp}	Particles	$\langle B_0 \rangle$
1	750 TeV	0.24 pc	10 pc	5.0 pc	3×10^5	3 μG
2	7.5 PeV	2.4 pc	100 pc	50 pc	10^5	3 μG
3	30 PeV	10 pc	100 pc	60 pc	10^5	3 μG

The magnetic field can be interpreted as a snapshot of the local interstellar magnetic field. Since the MHD simulation can be scaled to an arbitrary injection scale, in this study, two physical scenarios are investigated: an injection scale of $L_{inj} = 10$ pc, which is approximately the magnitude typical of the Milky Way spiral arms, and $L_{inj} = 100$ pc, which is characteristic of the interarm regions (see section 5.2). Although the ISM surrounding the solar system seems to have interarm properties [35, 36], both cases are taken into consideration. Assuming a particle gyroradius of 5 grid-points (corresponding to the smallest spatial scale in the MHD simulation), the injection scale sets the particle energy scale. In order to avoid grossly underestimating the effects of magnetic perturbations smaller than the particle gyroradius, the latter is set to 20 grid-points as well. Table 5.1 shows the three trajectory integration data sets used in this study. They cover an energy range from 750 TeV to 30 PeV, partially overlapping the recent cosmic ray observations reported by the IceCube Observatory [5, 1, 2].

In order to study the effect of interstellar magnetic turbulence on the arrival direction distribution of cosmic rays, a large number of particles would need to be injected with randomly uniform directions on a spheric surface centered at the Earth and with a radius larger than the mean free path. Unfortunately, such method would be highly inefficient because a large fraction of the injected particles would never reach Earth. The alternative approach is typically to use the so-called "back-propagation method," where the trajectories of particles with opposite charge are integrated from Earth, with initial directions uniformly distributed, backward into outer space. Since energy losses are negligible for proton particles, their energy is conserved, and therefore their trajectories can be time-reversed, provided there are no collisional scattering processes and no resonant scattering. Under such general conditions, Liouville's theorem states that particle density in phase space is conserved along

particle trajectories. In the presence of turbulence, magnetic fields can vary faster in space than the particle gyroradius, thus breaking adiabaticity and effectively inducing collisional processes. In section 5.3, the applicability of Liouville's theorem in the present case is discussed.

For set 1 of Table 5.1, 3×10^5 proton trajectories are integrated, while for sets 2 and 3, the number of particles is 10^5. The numerical trajectory integration starts from a point at the center of a 3×3 MHD simulation box, with uniform direction distribution, and stops when particles reach the edge of the integration volume. The integration box corresponds to a distance scale of 75 pc (for set 1 in table 5.1) and of 750 pc (for sets 2 and 3 in Table 5.1). The back-propagated trajectories calculated in this way provide the information on the effects of the magnetic field on an initially uniform particle distribution emanating from one point. In other words, they provide a map of regions that are magnetically connected to the origin at a given distance. The calculation implicitly takes into account the dynamical processes of a particle's motion in a magnetic field, including drifts and pitch angle scattering. Under the hypothesis that such trajectories are time-reversible (see section 5.3), they can be interpreted as directly propagating from outer space back to the original point (assumed to coincide with Earth). This means that the particle distribution far from Earth, resulting from the back-propagation numerical calculations, corresponds to a perfectly uniform arrival distribution at Earth.

The numerically calculated trajectories can be used, therefore, to determine the arrival distribution at Earth as a consequence of a global anisotropy at a large distance. Such a global anisotropy, which is the effect of a particle density gradient induced by sources of cosmic rays or by convective processes, is treated as a weight on the forward-inverted trajectories, and it effectively produces a nonuniform arrival direction distribution at Earth, which is described in section 5.4.2.

5.3 The Validity of Liouville's theorem

Generating a large number of particle trajectories that pass through a point in space is implicitly highly inefficient, since most particles will bypass the target point. One possibility is to increase the size of the target to record those particles that pass "nearby," or to appeal to Liouville's theorem.

Liouville's theorem states that the density of particles in the neighborhood of a given system in phase space is constant if restrictions are imposed on the system [42], as shown below. To determine its validity for our specific case of cosmic ray arrival distribution, we shall start with the continuity equation in phase space [22, 23], under the assumption that the number of particles stays fixed:

$$\frac{\partial \rho}{\partial t} = -\vec{\nabla} \cdot (\rho \vec{v}) - \vec{\nabla}_p \cdot (\rho \vec{F}) \tag{5.3}$$

where $\vec{\nabla}_p$ is the `del` operator in momentum space, ρ the distribution function, and $\vec{F}$ the applied external force.

Upon expansion of this expression, we arrive at:

$$\frac{\partial \rho}{\partial t} = -\rho \vec{\nabla} \cdot (\vec{v}) - \vec{v} \cdot \vec{\nabla}(\rho) - \rho \vec{\nabla}_p \cdot (\vec{F}) - \vec{F} \cdot \vec{\nabla}_p(\rho) \tag{5.4}$$

The first term on the right-hand side of Eq. 5.4 vanishes, since the divergence of the velocity in phase space is zero. The third term in the right-hand side of Eq. 5.4, with $\vec{\nabla}_p \cdot (\vec{F})$, gives us restrictions on the forces that can be applied to the particles. For this term to go to zero, we need the forces to be conservative and differentiable. In particular, they must be p-divergence free. Evidently, if collisions are present, they will not fulfill these requirements. Now, we can analyze the case of magnetic forces and can express this term explicitly:

$$\vec{\nabla}_p \cdot (\vec{F}) = q\vec{B} \cdot (\vec{\nabla}_p \times \vec{v}) - q\vec{v} \cdot (\vec{\nabla}_p \times \vec{B}) \tag{5.5}$$

Assuming that the magnetic field is independent of the velocity of the particle, the p-curl of $\vec{B}$ goes to zero. In this case, the assumption is valid since the particles are moving so fast that the possibility of changing the magnetic field is negligible. For the p-curl of $\vec{v}$, it just vanishes, since the velocity is the gradient of a scalar function, the relativistic energy. Therefore, if we have only pure magnetic forces, the $\vec{\nabla}_p \cdot (\vec{F})$ cancels.

We arrive at the equation:

$$\frac{\partial \rho}{\partial t} + \vec{v} \cdot \vec{\nabla}(\rho) + \vec{F} \cdot \vec{\nabla}_p(\rho) = 0 \tag{5.6}$$

But this is just the expression for the total derivative of the distribution. Therefore, we can reexpress it as:

$$\frac{d\rho}{dt} = 0 \tag{5.7}$$

which is the precisely the expression for Liouville's theorem [42, 23].

This derivation is for a pure magnetic force, but in fact when calculating the particles' trajectories in a turbulent magnetic field, a variety of factors come into play. The most significant effect is when particles encounter a region where the magnetic field varies abruptly, i.e., the scale of variation of the magnetic field is shorter than the gyroradius of the particle. In this scenario, the trajectory does not have time to adjust smoothly to this change, and the interaction can be effectively considered a collision. For such cases, the right-hand side of Eq. 5.6 can be modified by the addition of a term, $\left[\frac{\partial \rho}{\partial t}\right]_c$, which takes into account collisions of various origins that are differentiated by their exact functional form, given the fact that they will cause a nonzero time rate of change in the distribution function [18]. Therefore, under these conditions, Liouville's theorem can't be applied. To ensure that the abruptness in the trajectory is limited, we can calculate how adiabatic this change is. Having established this, it will ensure that a smooth variation will not greatly modify the density in phase space.

In the presence of collisions, the magnetic moment of the gyrating particles changes. Therefore, to check for the adiabaticity of the trajectories, we can calculate the magnetic
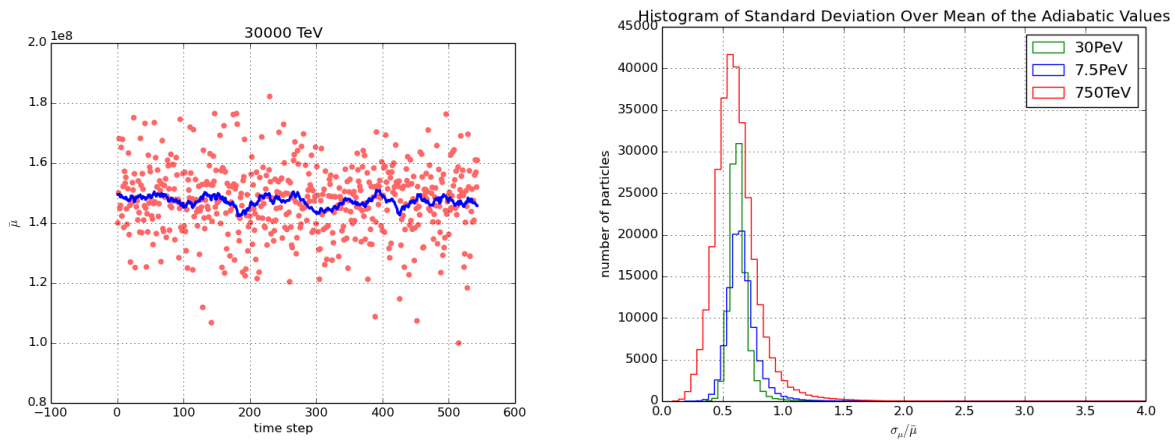
Figure 5.1: *Left*: The mean magnetic moment $\bar{\mu}$ for the data set at 30 PeV (red circles) with the corresponding moving average with subset of 30 time steps (blue line). The magnetic moment is calculated for all the particles at each time step, and then the average for the total set is calculated at each step. *Right*: Histogram of standard deviation of magnetic moment σ_μ over mean magnetic moment $\bar{\mu}$ for the three data sets of Table 5.1. The red, blue, and green lines represent 750 TeV, 7.5 PeV, and 30 PeV protons, respectively. The magnetic moment is calculated for each particle at all time steps. The mean value and the standard deviation are for the total trajectory. Note that the 750 TeV set has three times the number of particles as the other sets, as described in Table 5.1.

moment for each particle at each time step and find out if it statistically behaves as an adiabatic invariant.

The relativistic magnetic moment (also called *first* adiabatic invariant) is given by:

$$\mu = \frac{p_\perp{}^2}{2m|\vec{B}|} \tag{5.8}$$

where $p_\perp$ is the momentum perpendicular to the magnetic field $\vec{B}$ and m the particle mass. This quantity, relating magnetic field and perpendicular momentum of the particle, is conserved if the field gradients are small within distances comparable to the particle gyroradius. Using the integrated particle trajectories from the data sets of Table 5.1, the magnetic moment Eq. 5.8 was calculated at each integration time step and histogrammed in time step slices. In each time slice, the mean value $\bar{\mu}$ of the magnetic moment of the particle ensemble from each data set and the corresponding standard deviation σ_μ were

calculated. Figure 5.1 shows the evolution of $\bar{\mu}$ over the integration time of the 30 PeV set (on the left) of Table 5.1 and the ratio $\sigma_\mu/\bar{\mu}$ for the three sets (on the right) of Table 5.1. A perfect distribution with $\sigma_\mu/\bar{\mu} = 0$, indicates that the particles most likely stay in the same magnetic field line, which is unrealistic for a particle moving along a turbulent magnetic field. Nonetheless, a distribution peaked at a value much larger than one will tell us that the particles suffered strong variations in their trajectories and collision-like interactions happened. The distributions calculated for our three different energy data sets peak at around 0.5 and do not appear to have trends or large variations during integration time (compared to σ_μ), as shown on the left of Figure 5.1. This indicates that even though the particles have interacted with the turbulent field, and it has changed their trajectories, the changes are relatively smooth and with limited statistical impact on the overall particle ensemble.

Note that the width of the distributions in $\sigma_\mu/\bar{\mu}$ means that at some level the magnetic moment of the particles fluctuates during propagation. Different particles follow different magnetic field lines and experience different interactions. There might be also a contribution from the limited accuracy of the numerical integration. However, as discussed and shown in appendix A.1, in the present application, the effects due to accuracy limitations are not sufficiently large to significantly violate adiabaticity. The highest level of possible inaccuracy, where particles are stochastically re-distributed at each gyration, provides a numerical diffusion at the level of Bohm diffusion, where particles are scattered every gyration. It has been proven that in astrophysical turbulence Bohm diffusion is always much smaller than diffusion induced by magnetic field line wandering [56]. So the fact that the accuracy of the used trajectory integration method is significantly below the Bohm diffusion level (see appendix A.1) poses no problem on the statistical results obtained in this study.

Based on the fact that the ensemble-average $\langle \sigma_\mu/\bar{\mu} \rangle \lesssim 1$, especially that only magnetic forces are explicitly taken into account and that the changes in the particles' trajectories are relatively smooth, it is assumed that Liouville's theorem is applicable (see further discussions in Section 5.5). So in this study, back-propagation of the particle trajectories is justified in this statistical sense. The situation changes if scattering rate is higher, such as in the
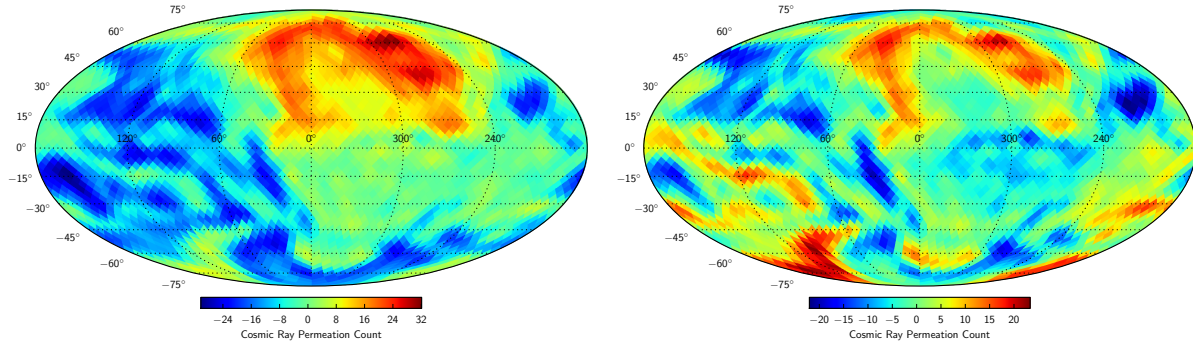
Figure 5.2: Sky map of arrival direction distribution of the 7.5 PeV proton set of Table 5.1 after propagation for a distance of 40 pc. The decomposition of the initial dipole distribution is shown. On the left is the sky map obtained after time inversion, and on the right is the same map after subtracting the dipole component from the map on the left. A Gaussian smoothing with $\sigma = 3°$ was used.

heliospheric magnetic field case studied in [59], where resonant scattering processes produce larger deviations from adiabaticity.

5.4 Results

This section shows the results obtained with the numerical calculation data sets described in Section 5.2.2.

5.4.1 Mean Free Path

Using the particle trajectory data sets from Table 5.1, it is possible to evaluate general properties that the ensemble of particles have after a sufficiently long duration of propagating in the turbulent magnetic field. The mean free path λ_{mfp} is the distance at which the instantaneous particle directions become uncorrelated with respect to those at time t=0. At this distance, and associated to scattering time scale, particles have lost *memory* of the direction distribution at initial conditions. This is a cumulative property of all particles, and it can be estimated by calculating the mean distance at which the direction of each particle has an angle of 90° from its initial position. This definition is equivalent to evaluating the

velocity autocorrelation function and estimating the distance at which it is sufficiently close to zero (i.e., correlation to initial condition is lost).

The results of λ_{mfp} calculations are given in Table 5.1. As expected in this regime, the mean free path increases with energy. For the interarm region, where the injection scale is on the order of 100 pc, $\lambda_{mfp} \sim 60$ pc for 30 PeV protons. For an energy four times smaller, 7.5 PeV, the mean free path decreases to a value of 50 pc. In the spiral arm, with injection scale on the order 10 pc, our calculation for 750 TeV protons is 5.0 pc. Note that in the two lowest energy data sets considered here, the particle gyroradius is on the order of the damping scale of the turbulent field. Therefore, pitch angle scattering arising from smaller scale magnetic perturbations is significantly reduced, and may result in the mean free path being overestimated to some degree. In the present work, the intent is to show the effects of turbulence in the particle spatial distribution in relation to the mean free path; therefore, whether the value is strictly correct is of limited importance in this context. In future studies, the need to use MHD simulations in a wider inertial range will be considered in more detail.

5.4.2   Sky Maps of Arrival Direction Distribution

The particle trajectories numerically integrated with Eqs. 1-2 for the sets in Table 5.1 are used to study the properties of their arrival direction distribution that results from the scattering off magnetic turbulence from a particle density gradient. As described in Section 5.2.2, the procedure used for determining the sky maps of the particles' arrival distribution makes use of the trajectory integration backward in time, uniformly emanating from one point assumed to be Earth, until they exit the integration box. At a sufficiently long distance from the origin, particle trajectories accumulate in the direction of the mean magnetic field, since the perpendicular diffusion is smaller than that which is parallel to the magnetic field lines. A sphere of radius R with center at the origin of the back-propagated trajectories is used to record the position and velocity direction of each trajectory. The trajectories are inverted in time from those locations on the sphere to the origin, by virtue of Liouville's theorem (see

Section 5.3 for a discussion of the validity of Liouville's Theorem and the consequences of its use in the context of the present study).

It is likely that there are several sources of cosmic rays in the Milky Way, perhaps from different populations injecting particles into the ISM with different energy spectral shapes. It is also possible to suppose that a single source may dominate the cosmic ray distribution at Earth, depending on the energy range (see Section 5.1). In a scenario of isotropic diffusion, the cosmic ray density gradient is expected to be described by a simple dipole distribution. This is a similar distribution as would be expected if convective transport were the dominant source of the cosmic ray density gradient, such as in the case of superbubbles [20] or the effect of Loop I shell in the local ISM [75]. In the general and more likely scenario of anisotropic diffusion, cosmic ray propagation along the magnetic field line is faster than the perpendicular, thus producing a cosmic ray gradient ordered along the regular magnetic field (see, e.g., [47, 60]). Although the density gradient is not expected to be a dipole but rather a distribution that depends on the ratio of perpendicular to parallel diffusion, in this work it is assumed a simple dipole distribution, regardless of the origin of the underlying density gradient of the cosmic rays.

If the underlying distribution of cosmic rays is perfectly uniform, the effects of scattering off magnetic turbulence shuffles one isotropic distribution into another isotropic distribution. However, with an existing particle density gradient, the scattering processes redistribute particles from the region of higher density to that of lower density, and vice versa, thus creating a complex arrival distribution that can be described with higher order multipole terms of the spherical harmonic expansion.

In the process of inverting time on the numerically calculated trajectories, a dipole gradient distribution, assumed to be aligned with the direction of the mean magnetic field of the MHD snapshot, is introduced as a weight on each trajectory at the crossing point on a sphere of radius R. The weight is calculated using the angle of the particle direction at the crossing point from that of the density gradient. The arrival distribution of these forward-propagated trajectories at Earth (i.e., the origin) is then determined. One key factor to remember is that

only the small-scale angular anisotropy is studied, since this is the one that arises from the specific interaction with the turbulent magnetic field. Therefore, the large scale component, specifically the dipolar component of the map at Earth, is fitted and removed. Such a dipole component can have a different direction and amplitude than that injected. Figure 5.2 shows the sky map, in equatorial coordinates, of the arrival distribution of the 7.5 PeV protons at Earth before (on the left) and after (on the right) dipole subtraction, thus emphasizing the small scale features. A Gaussian smoothing with $\sigma = 3°$ was used. The residual map shows medium- and small-scale angular structures arising from the breakout of the underlying dipole anisotropy after a propagation of $R = 50$ pc.

The maps were created with the HealPix mapping tool [43], which divides the sphere into pixels of equal areas. For the present work, a pixelization parameter of $N_{side} = 16$ was used, which corresponds to 3072 pixels in total, with a mean spacing of 3.67°. In Figure 5.2, the excess regions, with respect to the average isotropic flux, are identified by a red color and deficit regions by a blue one. Therefore, a pixel in which many particles pass through will be represented in a stronger red color than one that has only a few events.

Figure 5.3, under the assumption of the Earth's location in the interarm zone with L_{inj}=100 pc, shows the sky maps progression of the 30 PeV cosmic ray arrival direction distribution with the dipole density gradient weight at different propagation distances of $R = 10$ pc, 20 pc, 60 pc, and 90 pc. On each map, a dipole fit was performed, and the resulting dipole component was subtracted. Such a component may be different for each map, since it depends on the actual magnetic field structure at a given distance. The sky maps show that by increasing the propagation distance the arrival direction distribution progressively develops smaller structures up the mean free path (60 pc in this case, see Table 5.1). At larger distances, the arrival direction distribution reaches a statistically steady configuration (in Figure 5.2 only the 90 pc propagation distance is shown). Only propagation processes within the mean free path are responsible for the actual arrival direction distribution of cosmic rays at Earth, as discussed also in [39]. Whatever happens at larger distances is reshuffled by the scattering processes and is only relevant in the generation of the seed particle density

gradient at large scale.

The actual distribution of cosmic rays depends on the specific realization of the turbulent magnetic field and on the particle energy. Figure 5.4 shows the steady-state arrival direction distribution of 750 TeV (on the left) and 30 PeV (on the right) cosmic rays. This figure qualitatively shows that in the higher energy case the anisotropy of the distribution shows more small-scale angular regions than in the lower energy case. For a quantification of such a visual property, it is necessary to calculate the angular power spectrum. The map from 7.5 PeV presents almost the same distribution as the one for 750 TeV, since the only differences between them are the assumption on the injection scale and that they are independent sets (as described in Section 5.2.2 and shown in Table 5.1). The particles at 7.5 PeV energy and $L_{inj} = 100pc$ are physically equivalent to particles at 750 TeV with $L_{inj} = 10pc$.

5.4.3 Angular Power Spectrum

The sky maps of arrival direction distributions described in the previous sections are not dissimilar to experimental observations. However, it is the determination of the angular power spectrum that makes it possible to quantify the formation of small-scale structure anisotropy arising from scattering off magnetic turbulence. With the power spectrum, a sky map of arrival direction distribution is decomposed into spherical harmonics to provide information on the angular scale contribution of the anisotropy. The spectrum quantitatively indicates which multipole moments ℓ in the spherical harmonic expansion contribute to the observed map. The IceCube observatory provided a power spectrum of their Southern Hemisphere observation in the 10 TeV scale [4, 2] and the HAWC gamma-ray observatory provided one for the Northern Hemisphere in the TeV scale [8]. The angular power spectrum is determined using the `anafast` tool in the HealPix framework.

Figure 5.5 shows the angular power spectrum from the numerical trajectory integration set of 30 PeV protons at propagation distances from the initial unperturbed dipole anisotropy at 10 pc, 20 pc, 60 pc and 90 pc, as in Figure 5.3, but without subtracting the dipole

component. In the figure, the result from the observations made by the IceCube observatory is included as well. Note that the higher power values observed at low ℓ, not reproduced in the calculations, are most probably due to the partial sky view of the IceCube observatory, which causes correlations with the largest scale spherical harmonic moments. The experimental observation is for a median cosmic ray energy of about 20 TeV, much lower than the numerical calculations. The numerical calculation sets are normalized to the dipole component (i.e., ℓ = 1) of experimental power spectrum for the farthest propagation distance of 90 pc only. At shorter propagation distances, the normalization corresponds to the relative power obtained from the calculations. This normalization is valid since we are interested in the small-scale features, not on the assumptions on the large-scale anisotropy.

Note that the numerical calculation shows, within statistical fluctuations, that the power of the dipole component decreases with increasing propagation distance, due to the transfer of part of it into the higher ℓ components. At very short distances, i.e., smaller than the mean free path, the low multipole moments are dominant. However, as the distance increases, more power is transferred to the higher multipole moments, which is the signature of particle interactions with the turbulent magnetic field. Once they reach the mean free path distance, in this case 60 pc, the power spectrum converges to a steady configuration, as the sky maps in Figure 5.3 show. In Figure 5.5, the power spectrum of an isotropic flux of the same number of particles is included as a gray band and properly normalized [1]. It is evident that the distribution at distance λ_{mfp} and beyond is not only a random distribution but also possesses a definite structure. It is noted that the angular power spectra calculated for propagation distance longer that 90 pc show the same relative normalization and shape of that corresponding to the mean free path. This is compatible with the achievement of steady state in the anisotropy structures as evident in the sky maps of Figure 5.3. The approach of the power spectra to the band of isotropic distribution for $\ell > 30$ means that, for the numerical realization studied here, the smaller angular scales are indistinguishable

---

[1]The power spectrum of the isotropic flux is calculated by generating 10,000 realizations of uniform particle direction distribution, matching the number of the integrated particle trajectories, and calculating the power spectrum for each of them. The 68%, 90%, and 99% containment bands are reported in Figure 5.5

from random fluctuations of the isotropic flux.

As observed in Figure 5.4, the angular structure generated from the effect of scattering off magnetic turbulence depends on the particle energy (750 TeV and 30 PeV shown). This is evident also in the corresponding power angular spectra in Figure 5.6, calculated at the propagation distance of their mean free paths. The figure also shows the experimental result from the IceCube observatory at 20 TeV median energy, with the corresponding power of the isotropic distribution background and with the curve expected from the hierarchical breakup of angular components from [10], normalized to the dipole component of the IceCube result. Note that the angular power spectrum at higher energy is flatter than that at lower energy. This is compatible with the existence of more small-scale structures as evident in the sky maps of Figure 5.4.

5.5   Discussion

We have shown how small-scale anisotropy arises from the interaction of particles with the turbulent magnetic field. Specifically, we have addressed how the integration of trajectories in an MHD turbulent magnetic field provides a realistic understanding of the small-scale features present in the observations of cosmic ray anisotropy at Earth. The ISM is in a plasma state, where the MHD equations serve as a model for its dynamics, therefore an MHD turbulent magnetic field is a natural approach to study the magnetic field properties in the ISM. Previous work [39] had considered the effects of magnetic turbulence on cosmic ray distribution. In this study, the authors have considered synthetic turbulence, which, on one hand, lacks the proper development of the gas dynamics but, on the other hand, provides the first qualitative connection between a magnetic turbulent field and cosmic ray arrival directions. In compressible MHD turbulence, scattering efficiency strongly depends on the wave type and how the particle gyroradius compares to the turbulence scales. Specifically, fast modes are identified as the main source for cosmic ray scattering [79].

The dynamics of the different turbulence modes and the relationship between particle

energy and turbulence scale determine the actual scattering efficiency, which is most responsible for the breakout of a global cosmic ray density gradient into small-scale angular anisotropy. The angular power spectrum calculated for the data sets studied in this work appears to evolve in time until particles cross the mean free path distance. In a steady state, the shape of the angular power spectrum is a function of the magnetic field structure and of the consequent effects on particle propagation.

Studying particle trajectories in MHD magnetic turbulence provides a more realistic framework to investigate the behavior of cosmic ray propagation in the ISM, where turbulence is expected to be anisotropic, although MHD turbulence simulations typically represent a significantly more restrictive inertial range than the actual astrophysical plasmas.

The ISM is a complex environment and its exact representation is difficult to achieve; therefore, our MHD magnetic field can be considered one possible configuration of the magnetic field in the ISM. For this reason, direct comparison should be on the angular power spectrum itself, not on the exact topology of the small-scale features in our maps.

The framework for the application of Liouville's theorem is provided in the context of cosmic ray arrival distribution and applied through the back-propagation method. Although particle trajectories appear to suffer from mild deviation from adiabaticity, Liouville's theorem was applied in this particular case to study the first order effects of magnetic turbulence on the global topology of particle trajectories. This is because particles do not experience severe scattering in their trajectories, as shown in the first adiabatic invariant calculations; nonetheless, if the magnetic field were to vary dramatically with respect to the gyroradius of the particles, it prohibit application of Liouville's theorem. The spread in the magnetic moment μ distribution in Figure 5.1 suggests that some trajectories may have experienced more scattering than average in their propagation. This effect will manifest in the anisotropy through higher power at high ℓ, since these particles will have had greater interactions with the turbulent field, resulting in a slightly flatter angular power spectrum. If the distribution on the $\sigma_\mu/\bar{\mu}$ plot had peaked at a higher value or a progressive trend had appeared on the mean magnetic moment plot of the data set, this would be an indication of a clear violation

of Liouville's theorem. Neither of these trends have statistically or significantly occurred in our calculations; nevertheless, we would expect them to appear in magnetic fields that have a strong variation in scale on the order of the gyroradius of the particles. Future studies will need to use MHD turbulence simulation with wider inertial range to include enlarge the energy range in which magnetic turbulence affects cosmic ray distribution. In this way, these studies will reveal the connection between the angular power spectrum of the cosmic ray arrival direction distribution and the turbulence properties, naturally accounting for spurious effects derived by the numerical methods used.

As mentioned in Section 5.2.2, the trajectory back-propagation method is intended to provide a high efficiency in the studies of particle propagation in magnetic fields. Such a numerical method provides a mapping of the regions in space that are magnetically connected to the arrival point, where particles are assumed to be isotropically distributed. Therefore, appealing to the conservation of the total power across all spherical harmonic contributions, as dictated by Liouville's theorem, makes higher multipole moments possible. Anisotropy was studied as a function of an initial large-scale density gradient at a large distance from the arrival point. Such a density gradient, however, is generated by the same propagation processes that produce all angular structures in the arrival direction distribution as well. In fact, smaller scale structures can arise in trajectory forward-propagation integration methods, where particle escape is naturally accounted for, even without assuming an initial global anisotropy, as shown in [70]. On the other hand, as long as a global anisotropy is developed at some distance larger than λ_{mfp}, independently on how it is generated, the arrival direction distribution reaches a steady state angular power spectrum, and the effects of *seed* anisotropy and observed anisotropy can be disentangled.

For the mean free path calculation, it is shown to be dependent on energy. In this regime, from 750 TeV to 30 PeV, the λ_{mfp} increases with energy. This is in agreement with how the more energetic particles interact with the perturbations of the magnetic field. In the case of the 750 TeV and 7.5 PeV sets, the minimum scale in the power spectrum of turbulence is of the size of the gyroradius of the particles, which may cause an overestimation of the λ_{mfp},

since there is limited power in the physical perturbations that interact with the particles. For our 30 PeV particles, we are well above this minimum scale, so the λ_{mfp} is unaffected.

The anisotropy maps and their corresponding angular power spectrum can tell us about the propagation of the particles themselves in the turbulent field. At very short distances, the low multipole moments are completely dominant and hold most of the power, as shown with the line of 10 pc in Figure 5.5. The reason for this is that the particles have not had enough time to interact with the features of the magnetic field, and the distribution is still reminiscent of the initial configuration. However, the particles continue to interact and structures start to develop. As we can see with the line of 20 pc in Figure 5.5, the higher multipole moments start to rise, with small-scale features becoming highly visible even in the maps in Figure 5.4. One interesting feature is that the small-scale structures develop within the mean free path, but once they reach this scale, the maps do not change significantly. This observation is confirmed in the angular power spectrum. Therefore, the distribution of power between the different multipole moments reaches a steady state. Of course, the particles keep moving and interacting after they have reached one λ_{mfp}, but the anisotropy itself does not change. From Figure 5.5 it is possible to see that this steady distribution is not isotropic, yet it possesses a definite structure that is dependent on the nature of the turbulent magnetic field. Consequently, the observed anisotropy is for the most part created in the last λ_{mfp} of the particle's trajectory, and it becomes a way to indirectly probe the local ISM.

In Figure 5.5, we can see from the comparison with the observations that the experimental data behaves according to what we would have expected from a lower energy. In the case of 20 TeV, the distribution of power among the higher multipole moments is lower than at the higher energy, i.e., 30 PeV. One of the causes is that the 30 PeV particles interact with perturbations that carry more power than the ones at a lower energy. Therefore, when an interaction process occurs with these perturbations, the higher energy particles are affected more strongly and more small-scale structure is created.

This effect is confirmed in Figure 5.6, where the spectrum at the λ_{mfp} of energies 750

TeV and 30 PeV is compared with the observations at the median energy of 20 TeV. The distribution at 750 TeV is similar to the observations at 20 TeV; however, for 30 PeV, the distribution of high multipole moments is much higher and flatter than that at lower energy. Therefore, greater small-scale anisotropy is observed at higher energies. This is also easily seen in the maps in Figure 5.4.

The flatter angular power spectrum obtained with 30 PeV compared to 750 TeV protons tells us about differences in pitch angle scattering as a function of energy. However it is important to note that the 750 TeV data set corresponds to a gyroradius scale close to the dissipation region of the MHD turbulence inertial range. It is likely that scattering is underestimated, thus preventing a full development of small-scale angular structures in the particle anisotropy. From this point of view, it is reasonable to assume that the resemblance of the 750 TeV proton power spectrum to experimental data should be considered coincidental but still in agreement with the fact that lower energies should have less structure, as mentioned above. On the other hand, the difference of the 30 PeV proton power spectrum with experimental data does not necessarily mean that the fundamental processes responsible for the small-scale anisotropy are overestimated in the present study. The results show an energy dependence in the shape of the angular power spectrum that needs further study, requiring MHD turbulence simulation with a significantly wider inertial range.

Figure 5.6 includes the angular power spectrum resulting from hierarchical decay of angular scales if Liouville's theorem is satisfied, as calculated by [10]. Here the different curves have been normalized to the dipole of the observational data, as discussed in Section 5.4.3, so that only the small-scale structure is relevant. In [10], an existing global dipole anisotropy evolves to create higher multipole moments. The difference between that result and the one shown in the present work resides in the fact that here the shape of the distribution is determined by the specific turbulence characteristics of the magnetic field and the gyroradius of the particles. The 750 TeV case appears similar to [10], but since this set is at the damping scale and scattering is likely to be underestimated, we were already expecting less structure to be present.

[11] studied the effect of relative diffusion, i.e., from correlated nearby trajectories, as the contribution to the development of small scale anisotropy structures. In this complementary approach, the angular power spectrum is calculated based on the effect that a particle density gradient has on the trajectory topology shaped by homogeneous isotropic magnetic turbulence. In the present work, the relationship between the shape of angular power spectrum and the scattering processes induced by Alfvénic, slow, and fast modes in a compressible MHD turbulence were studied. This will make it possible to identify physical properties that shape the angular power spectrum, so that the problem can be inverted, i.e., the angular power spectrum and different cosmic ray energies and masses can be used to probe the properties of the interstellar magnetic turbulence.

5.6   Conclusions

This work explores the possibility that the local interstellar magnetic field could shape the arrival direction distribution of high-energy cosmic rays. An MHD turbulent magnetic field was used as a propagating medium that resembles the ISM, and particle trajectories with various energies were integrated in this field. To obtain the anisotropy in arrival direction distribution at Earth, the theoretical framework for application of Liouville's theorem was provided, and the theorem was shown to be applicable in this specific case. Nonetheless, there could be cases where the magnetic field varies abruptly, which would ultimately violate the application of the theorem.

The results presented in this work show that small-scale anisotropy arises from the interaction of cosmic rays with the local turbulent magnetic field, as confirmed in the sky maps and angular power spectra. The angular power spectrum becomes flatter the higher the energy; therefore, experimental data at the 10 TeV scale is expected to be steeper than the numerical calculations presented in this paper. Cosmic rays with less rigidity are more sensitive to the lower power small-scale magnetic perturbations. Since cosmic rays are not composed only of protons, the contribution of heavy ions would yield a steeper angular power

spectrum.

The inertial range of our turbulent magnetic field provides a limitation on the lowest energy that could be studied, in this case 750 TeV. Therefore, in the future, it will be necessary to extend this inertial range and sample even lower energies, so that direct comparisons with the observations at 20 TeV will be possible. Still, it is expected that at these TeV energies the effects of the heliosphere should be present as well, which would provide a primary topic for future study and publication. Another factor to improve is the number of particles that are propagated. If we were to have at least 10^7 events, it would be possible to obtain a clearer view of the distribution of cosmic rays at Earth. Investigating how the properties of our local turbulent magnetic field might influence TeV-PeV cosmic ray arrival direction distribution will provide the basis for further exploring the observed anisotropy, and it will open the doors for a better understanding of our local interstellar medium.
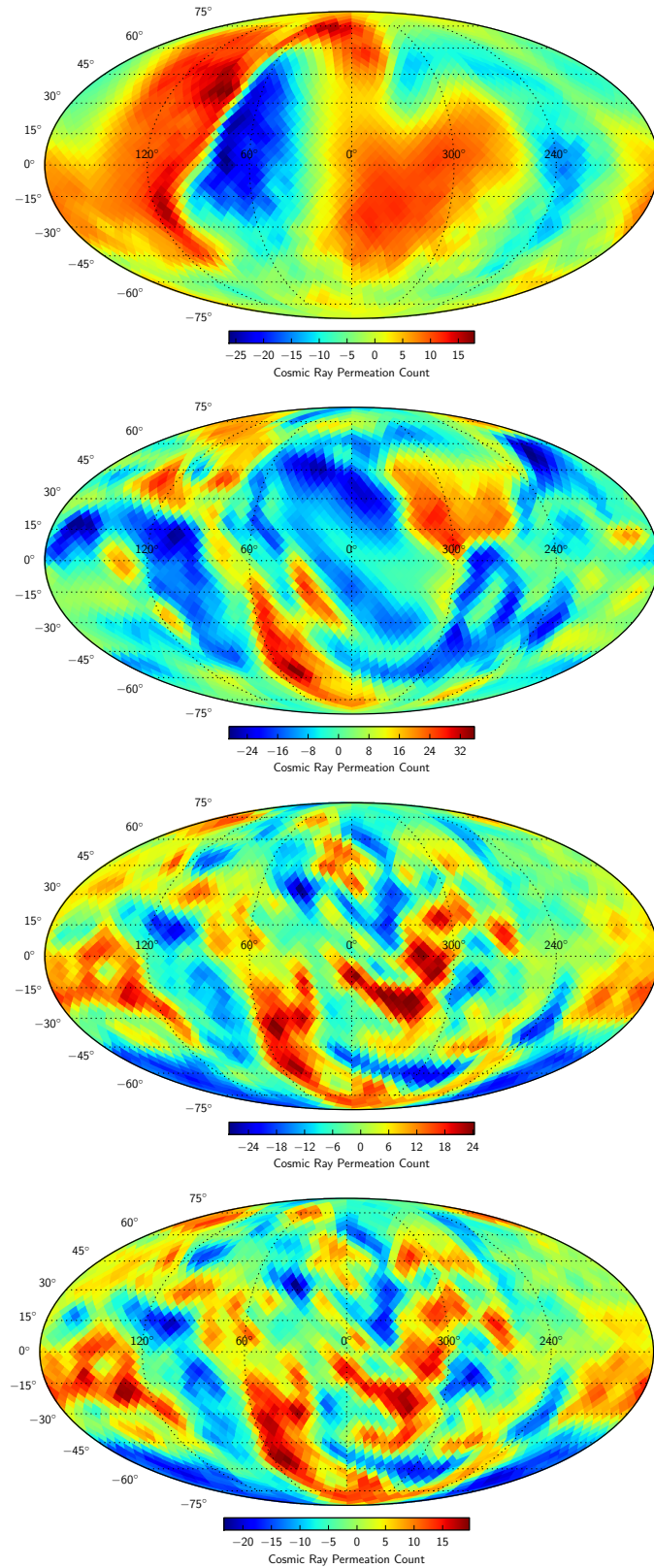
Figure 5.3: Sky maps of arrival direction distributions of 30 PeV protons in equatorial coordinates, with the dipole density gradient weight at different distances: $R = 10$ pc, 20 pc, 60 pc, and 90 pc (from top to bottom). Gaussian smoothing with $\sigma = 3°$ was used. On each map, a dipole fit was performed and the resulting dipole component was subtracted.
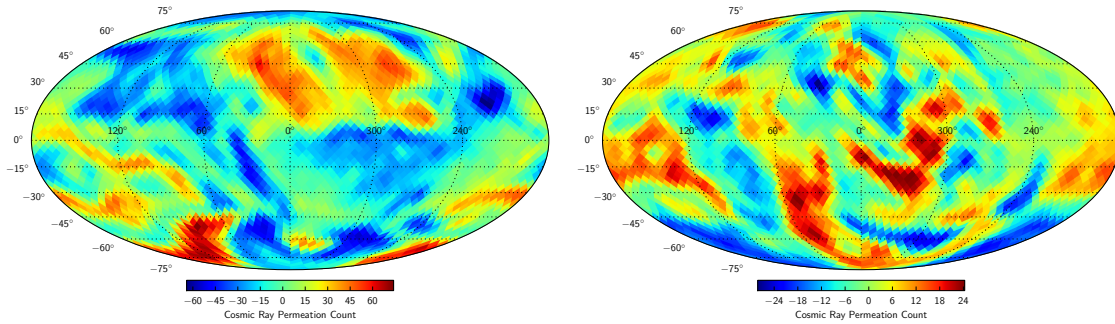
Figure 5.4: Sky maps of arrival direction distributions of 750 TeV protons (on the left) and 30 PeV (on the right) in equatorial coordinates and at propagation distance corresponding to the mean free path. Gaussian smoothing with $\sigma = 3°$ was used. On each map, a dipole fit was performed and the resulting dipole component was subtracted.
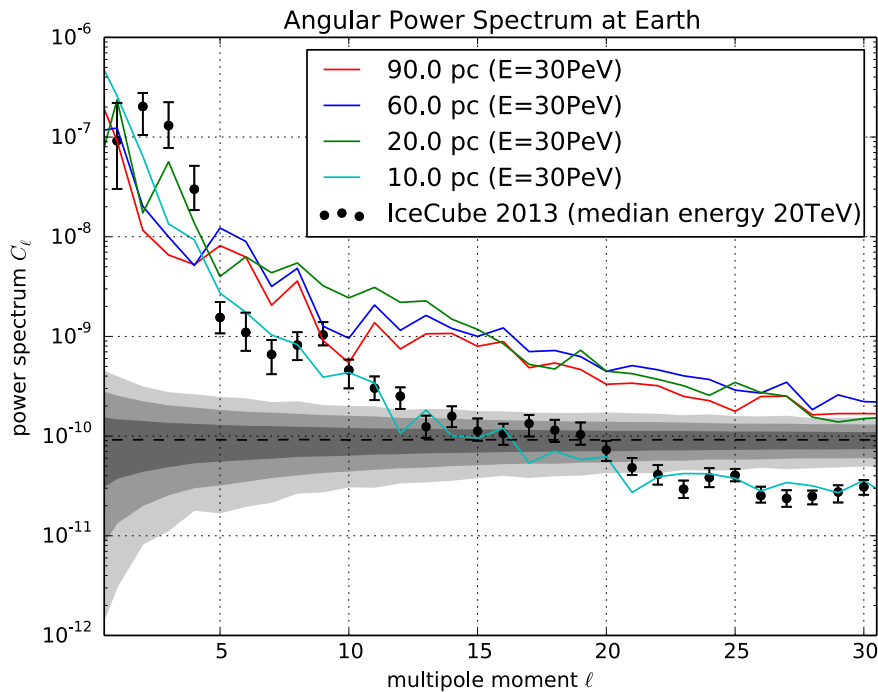

Figure 5.5: Angular power spectrum of the arrival direction distribution of 30 PeV trajectories set of Table 5.1 and Figure 5.3 with dipole weight injected at a distance of 10 pc (in cyan), 20 pc (in green), 60 pc (in blue and corresponding to the mean free path) and of 90 pc (in red). The gray bands show the 1σ, 2σ and 3σ bands for a large set of isotropic sky maps. The black circles are the results from the IceCube observatory at a median energy of 20 TeV [71]. Note the difference in energy scale between the experimental data and the numerical calculations.
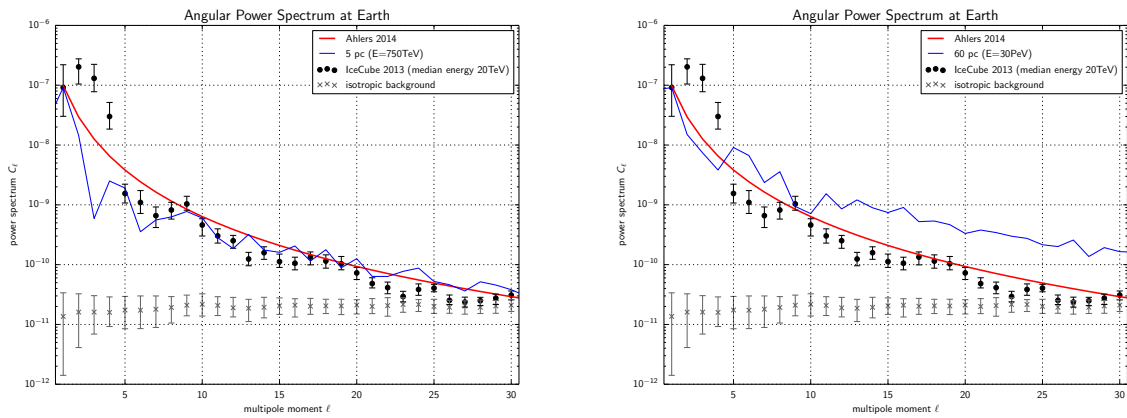
Figure 5.6: Angular power spectrum of the arrival direction distribution of 750 TeV (blue line on the left) and 30 PeV (blue line on the right) trajectories sets of Table 5.1 with dipole weight injected at the corresponding mean free path distance. The red line is the power spectrum from [10]. The black circles are the results from the IceCube observatory at a median energy of 20 TeV. The gray crosses and error bars show the 1σ band for a large set of isotropic sky maps [71]. Note the difference in energy scale between the experimental data and the numerical calculations.

Bibliography

[1] Aartsen, M. et al. 2013b, Astrophys. J. 765, 55

[2] Aartsen, M. et al. 2015, submitted to ApJ

[3] Abbasi, R. et al. 2010a, Astrophys. J. 718, L194

[4] Abbasi, R. et al. 2011a, Astrophys. J. 740 16

[5] Abbasi et al. 2012b, Astrophys. J. 746, 33

[6] Abdo, A.A. et al. 2008, Phys. Rev. Lett. 101, 221 101

[7] Abdo, A.A. et al. 2009, Astrophys. J. 698, 2121

[8] Abeysekara, A.U. et al. 2014, Astrophys. J. 796, 108

[9] Aglietta, M. et al. 2009, Astrophys. J. 692, L130

[10] Ahlers, M. 2014 Phys. Rev. Lett. 112, 021101

[11] Ahlers, M., & Mertsch, P. 2015, arXiv:1506.05488

[12] Amenomori, M. et al. 2005, Astrophys. J. Lett. 626, L29

[13] Amenomori, M. et al. 2006, Science, 314, 439

[14] Amenomori, M. et al. 2011, Proc. 32nd ICRC, Beijing China

[15] Amenomori, M. et al. 2007, Proc. 30th ICRC, Mérida, Mexico

[16] Bartoli, B., et al. 2013, Phys. Rev. D 88-8, 082001

[17] Bartoli, B., et al. 2015, Astrophys. J. 809, 90

[18] Baumjohann, W., & Treumann, R. A. 1996, Basic Space Plasma Physics (London: Imperial College Press)

[19] Beresnyak, A., Yan, H., & Lazarian, A. 2011, Astrophys. J. 728, 60, 8 pp.

[20] Biermann, P.L., Becker Tjus, J., Seo, E.-S., & Mandelartz, M. 2013, Astrophys. J. 768, 124

[21] Blasi, P., & Amato, E. 2012, JCAP 1, 11

[22] Bradt, H. 2008, Astrophysics processes, Cambridge Univ. Press, Cambridge

[23] Bradt, H. 2008, in Astrophysics Process (Cambridge, (supplement): Cambridge Univ. Press)

[24] Burkhart, B. et al. 2014, Astrophys. J. 790 130

[25] Cho, J., & Lazarian, A. 2002, Phys. Rev. Lett. 88, 245001

[26] de Jong, J. et al. 2011, Proc. 32nd ICRC, Beijing, China

[27] Desiati, P. & Lazarian, A. 2012, NPG 19, 351

[28] Desiati, P. & Lazarian, A. 2013, Astrophys. J. 762, 44

[29] Desiati, P. & Zweibel, E.G. 2014, Astrophys. J. 791, 51

[30] Eyink, G.L., Lazarian, A. & Vishniac, E.T. 2011, Astrophys. J. 743, 51

[31] Effenberger, F. et al. 2012, A&A 547, A120

[32] Erlykin A.D., & Wolfendale A.W. 2006, Astropart. Phys. 25, 183

[33] Florinski, V., Jokipii, J. R., Alouani-Bibi, F., le Roux, J. A. 2013, Astrophys. J. 776, L37

[34] Florinski, V., Stone, E.C., Cummings, A.C., & le Roux, J.A. 2015, Astrophys. J. 803 47

[35] Frisch, P.C. et al. 2012 Astrophys. J. 760, 106

[36] Frisch, P.C. 2015 J. Phys.: Conf. Ser. 577, 012010

[37] B. M. Gaensler, et al. 2011, Nature 478, 214

[38] Gaisser, T.K. et al. 2013 Front. of Phys. 8-6, 748

[39] Giacinti, G., & Sigl, G., 2012 Phys. Rev. Lett. 109, 071101

[40] Giacalone, J. & Jokipii, J.R. 1999, Astrophys. J. 520, 204

[41] Goldreich, P., & Sridhar, S. 1995, Astrophys. J. 438, 763

[42] Goldstein, H., Poole, C., & Safko, J. 2002, Classical Mechanics (3rd ed.; San Francisco, CA: Addison-Wesley)

[43] Gorski, K. M., Hivon, E., Banday, A. J., et al. 2005, ApJ, 622, 759

[44] Guillian, G. et al. 2007, Phys. Rev. D 75, 062003

[45] Hall, D.L. et al. 1999, J. of Geophys. Res. 104, 6737

[46] Haverkorn, B., et al. 2008, Astrophys. J. 680, 362

[47] Kumar, R., & Eichler, D. 2014 Astrophys. J. 785, 129

[48] Jansson, R., & Farrar, G.R. 2012a, Astrophys. J. 757, 14

[49] Jansson, R., & Farrar, G.R. 2012b, Astrophys. J. 761, L11

[50] Jokipii, J.R. 1966, Astrophys. J. 146, 480

[51] Jokipii, J.R. & Parker, E.N. 1969, Astrophys. J. 155, 777

[52] Lazarian A., 2006 AIPC, 874, 301

[53] Lazarian, A. 2007, J. Quant. Spectros. & Radia. Transfer 106, 225

[54] Lazarian, A. & Desiati, P. 2010, Astrophys. J. 722, 188

[55] Lazarian, A., & Vishniac, E.T. 1999, Astrophys. J. 517, 700

[56] Lazarian, A., & Yan, H. 2016, Astrophys. J. 784, 38

[57] Lazarian, A. et al. 2012, Space Science Reviews 173, 557

[58] Lithwick, Y., & Goldreich, P. 2001 Astrophys. J. 562, 279

[59] López-Barquero, V., Xu, S., Desiati, P., et al. 2017, ApJ, 842, 54. doi:10.3847/1538-4357/aa74d1

[60] Mertsch, P. & Funk, S. 2015 Phys. Rev. Lett. 114, 021101

[61] Minnie, J., et al. 2009, JGR 114, A01102

[62] Munakata, K. et al. 2010, Astrophys. J. 712, 1100

[63] Nagashima, et al. 1998, J. of Geophys. Res. 1031, 17429

[64] Manuel, R., Ferreira, S., & Potgieter, M. 2014, Solar Physics 289, 2207

[65] Pogorelov, N.V., Zank, G.P., & Ogino, T. 2006, Astrophys. J. 644, 1299

[66] Pohl, M. & Eichler, D. 2013, Astrophys. J. 766, 9

[67] Ptuskin V. 2012, Astropart. Phys. 39, 44

[68] Press, W.H., Flannery, B.P., & Teukolsky, S.A. 1986, Cambridge: University Press, 1986

[69] Rechester, A.B. & Rosenbluth, M.N. 1978, Phys Rev Lett 40, 38

[70] Rettig, R. & Pohl, M. 2015, in Proc. of 34th ICRC, The Hague, The Netherland

[71] Santander, M. et al. 2013, in Proc. of 33rd ICRC, Rio de Janeiro, Brazil; arXiv:1309.7006

[72] Savchenko, V., Kachelrieß, M. & Semikoz, D.V. 2015, DOI:10.1088/2041-8205/809/2/L23

[73] Shuwang, C. et al. 2011, Proc. 32nd ICRC, Beijing China

[74] Shalchi, A. 2009 Nonlinear Cosmic Ray Diffusion Theories, ASSL 362 (Springer)

[75] Schwadron, N.A., Adams, F.C., Christian, E.R., Desiati, P., Frisch, P., Funsten, H.O., Jokipii, J.R., McComas, D.J., Moebius, E., Zank, G.P. 2014, Science 343, 988

[76] Sridhar, S., & Goldreich, P. 1994, Astrophys. J. 432, 612

[77] Sveshnikova, L.G. et al. 2013, Astropart. Phys. 50, 33

[78] Xu, S., & Yan, H. 2013, Astrophys. J. 779, 140

[79] Yan, H., & Lazarian, A. 2008, Astrophys. J. 673, 942

[80] Yan, H., & Lazarian, A. 2011, Astrophys. J. 731, Issue 1, article id. 35, 10 pp. (2011)

[81] Zhang, J.L. et al. 2009, Proc. 31st ICRC, Łódź, Poland

[82] Zhang, M., Zuo, P., & Pogorelov, N. 2014, Astrophys. J. 790, 5

Chapter 6

Conclusions and Future Work

This thesis details the contributions of coherent structures, chaos, the heliosphere, and local turbulent magnetic fields to the cosmic-ray anisotropy observed on Earth. Specifically, we found that:

- Chaotic behavior can originate from the interaction between cosmic rays and coherent structures. Our results show that the Finite-Time Lyapunov Exponent, a quantity that indicates the chaotic behavior of a trajectory, is related to the escape time of the system. This relation is given by a specific power law that persists even if perturbations act on the system. This specific power law could prove to be an intrinsic characteristic of the system. Additionally, the maps of arrival distribution in these systems display areas where the chaotic characteristics vary significantly. This result can potentially modify the cosmic ray arrival distribution.

- CRs are strongly affected by magnetic structures on the order of their gyroradius. 1-10 TV particles are subject to significant heliospheric scattering. This redistributes CRs and affects their arrival direction distribution. Our work shows that this scattering can have a significant effect on the observations. The study of the complex angular structure can provide important hints about the turbulent properties of the ISM and the heliosphere.

- Small-scale anisotropy arises from the interaction of cosmic rays with the local turbulent magnetic field, as confirmed in the sky maps and angular power spectra. Investigating how the properties of our local turbulent magnetic field might influence TeV-PeV cosmic ray arrival direction distribution will provide the basis for further exploring the observed anisotropy, and it will open the doors for a better understanding of our local interstellar medium.

6.1 Future Work

Our studies call for more extensive observations of CR anisotropies and more detailed numerical testing using high-resolution models.

As a natural continuation of the current work, we are studying the chaotic behavior of particles propagating in a heliosphere model. CRs with rigidities between 1-10 TV are severely affected by the heliospheric features; thus, distinct levels of chaos are anticipated. We are expecting to identify and classify regions of the arrival distribution maps according to this chaotic behavior. In this work, CRs are propagated in an MHD-plasma/kinetic-neutrals simulation model of the heliosphere. We will use the theoretical framework based on the Finite-Time Lyapunov exponents to study the chaotic characteristics of CRs. Consequently, we will focus on the arrival distribution maps and how the chaotic behavior is distributed to make predictions on the actual CR anisotropy measurements. Moreover, this mapping could potentially lead us to a description of time-variability in the CR anisotropy.

A similar approach could be made to describe other coherent structures with the model presented here. For example, the Local Bubble, Loop I, and the Local Cloud could be responsible for reshaping particles' arrival directions due to their bounded structures.

Another scenario to explore is the use of this coherent structure model for understanding intermittency in the ISM. Spatial intermittency is linked to abrupt gradients and coherent structures in magnetic fields. Such structures can modify the transport of charged particles. In this case, CR propagation in the interstellar medium is modified by coherent structures.

Therefore, we can use our analytical model of a magnetic bottle with time-dependent perturbations to create a configuration that will mimic the conditions in the ISM. Consequently, as a particle propagates in this system, its diffusion will be modified every time an interaction happens as it gets trapped on them. The main objective will be to study the properties of CR propagation under these conditions and how their arrival directions at the Earth will be affected.

Figure 6.1: Venus de Milo with Drawers, Salvador Dalí. Fundació Gala-Salvador Dalí / Artists Rights Society (ARS), New York, 2018

Chapter 7

Thesis Summary for the General Public

> Imagine you could travel the Universe at the speed of light.
> Imagine you were born in the middle of the death of a star.
> Imagine you are the most energetic entity in the Universe.
> Your imagination can bring you to envision all of these different
> scenarios, but if you were a cosmic ray, this is your reality.

This chapter aims to understand the fundamental ideas for the study of cosmic rays, how they propagate in the Universe and the explanations behind the way that they arrive on Earth. First, we will talk about the quintessential question: what are cosmic rays?

7.1   Cosmic Rays and their Fundamental Mysteries

The birth of the twentieth century saw a fantastic revolution in physics. Various surprising results start to appear. One of them was the discovery of radioactivity. Scientists at the time studied this phenomenon where certain substances would naturally emit small particles while they disintegrate. But one particular observation did not match with what they knew. At the moment, they thought that the main source of that radiation was coming solely from the Earth. Yet, when they would make observations even at very high altitudes, the radiation was still there.

Inspired by these experiments, between 1911 and 1912, Victor Hess, an Austrian physicist, conducted a series of experiments in balloon flights (see figure 7.1). He wanted to test at what distance from the Earth's surface the radiation would decrease, which was expected according to the theories of the time. Initially, he climbed to an altitude of 1000 meters and measured the radiation using an electroscope. Hess noticed no relevant changes in the levels there compared to the ground level. Later, in 1912, he rose to altitudes of 5000 meters. He did those ascents at night and during an almost total solar eclipse[1] to avoid having his results affected by the Sun. He noticed, at first, that the radiation decreased as the altitude increased, but then, as he got even higher, the radiation started increasing. This result was astounding and opposed expectations. Therefore, he concluded that the radiation must be coming from a source other than the Earth. A cosmic origin. This simple yet significant observation would become the beginning of the study of cosmic rays. [2] [3]
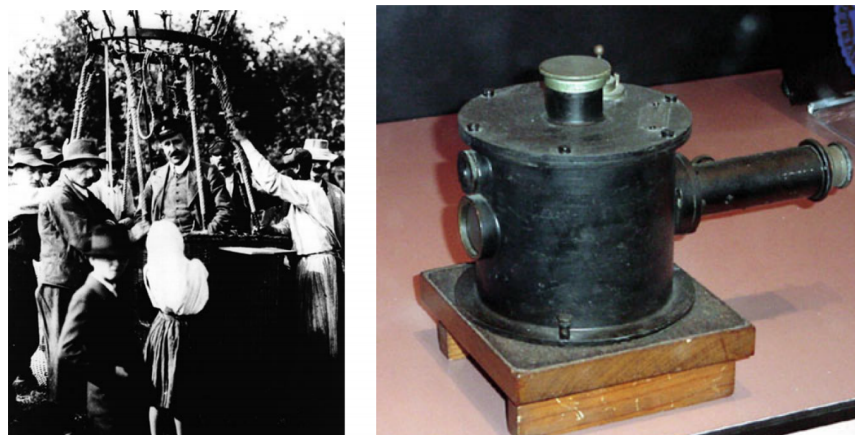

Figure 7.1: Left: Canonical photo of Victor Hess' balloon flight. Right: Electrometer used by Hess (Smithsonian National Air and Science Museum). Photos taken from: A. De Angelis and C. Arcaro b. Schultz, 2018 [4].

Even though *cosmic rays* may sound like they are rays of light, like the familiar X-rays or UV-rays. The name is a misnomer since, in the beginning, it was thought that they

---

[1] A solar eclipse occurs when the Moon is in between the Sun and the Earth; therefore, a shadow of the Moon is cast over the Earth.

[2] Victor Hess published his results in the *Physikalische Zeitschrift*. Translation to English and historical commentary by A. De Angelis and C. Arcaro b. Schultz [4].

[3] Hess received the Nobel Prize in Physics for this discovery in 1936. Prize motivation: "for his discovery of cosmic radiation."

were a type of light. But they are not. *Cosmic rays* (CRs) are small fragments of an atom—subatomic particles—that travel at almost the speed of light. We can think of them as the "cosmic messengers" of the Universe since they can transport information from one distant place in the Universe to another. And they can even reach us here on Earth. [4] They are mainly protons, helium, heavy nuclei, and electrons accelerated to high energies. They can have extremely high energies. For example, CRs have been detected at energies 20 million times greater than what particle colliders here on Earth can reach.

We are bombarded by millions of these particles every day at every second. Nonetheless, there are multiple mysteries involved when we talk about CRs. For example: where do they come from? How do they move across the Galaxy? And most importantly, for our purposes, what effects influence them as they arrive on Earth?

Cosmic rays can be classified based on their origin: solar, galactic, or extra-galactic (see figure 7.2). Solar CRs refer to particles that are accelerated in the Sun. For galactic CRs, we are talking about particles that have their origin in our galaxy, the Milky Way. And extra-galactic refers to CRs that are created outside our Galaxy.

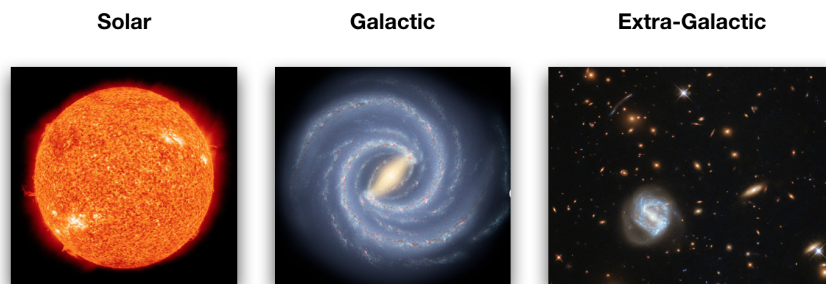**Solar**   **Galactic**   **Extra-Galactic**

Figure 7.2: Origin of Cosmic Rays. *Left:* The Sun photographed by the Atmospheric Imaging Assembly (AIA 304) of NASA's Solar Dynamics Observatory (SDO). *Center:* Artist's concept of the Milky Way. Source: NASA/JPL-Caltech/R. Hurt (SSC/Caltech). *Right:* The galaxy cluster in this image is SDSS J0333+0651. Credit: ESA/Hubble and NASA

In this chapter, we will concentrate on CRs that are galactic. At the moment, an exact place of origin for these CRs has not been pinpointed. However, one staple candidate can

---

[4]You can download an app for your phone that can detect cosmic rays. Basically, you can have a CR detector in your hand. The app is called CRAYFIS.

accelerate particles in the Galaxy. That perfect site for the acceleration of these particles is when a star dies, the so-called *supernova remnants*. When a star dies, it creates a shock that can accelerate CRs, similar to a surfer and a wave that accelerates them (see figure 7.3).
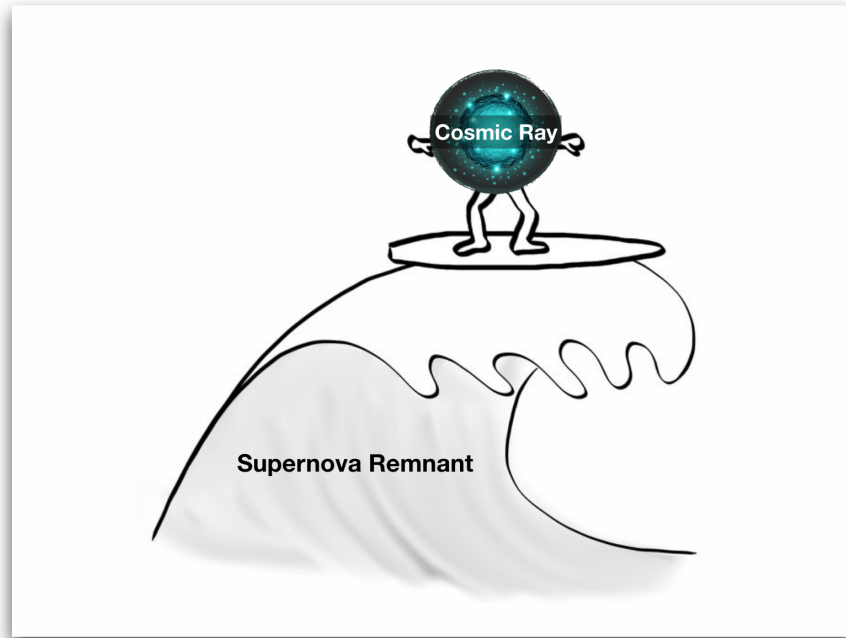

Figure 7.3: Supernova remnants as sites for CR acceleration.

7.2   Propagation of Cosmic Rays

Cosmic rays are extraterrestrial charged particles. Particles can be positively charged, such as a proton, or negative as an electron. The main issue from this characteristic is that charged particles do not follow a straight line but are affected by magnetic fields that deflect them. In figure 7.4, we have an example of what a CR trajectory could look like. Suppose a particle is injected into the Galaxy at point A and there were no magnetic fields. In that case, it will follow the straight white trajectory to point B. However, since magnetic fields are in their path, the trajectory will be deflected and twisted by them, such as the red trajectory in the figure. Therefore, if we were to detect the particle at point B, we would not be able to point directly towards the direction of origin A since that information has been distorted.

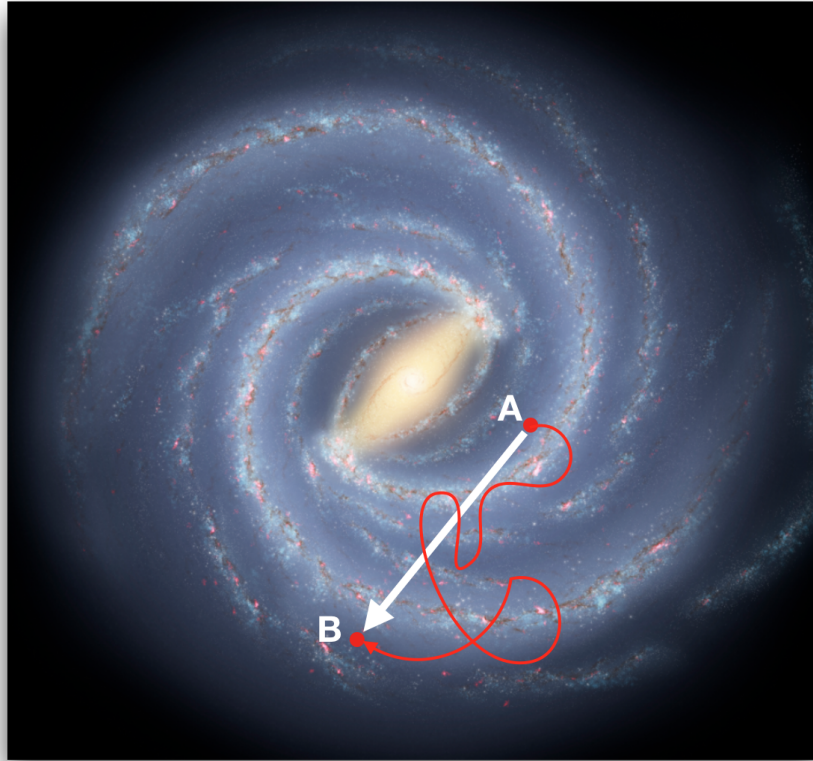This problem is the basis for exploring how particles arrive on Earth and what affects their propagation.

Figure 7.4: Cosmic Ray Trajectory. Cosmic rays do not follow straight lines in their trajectories because magnetic fields in the Galaxy deflect them.

One of the challenges concerning this problem and its captivating argument is that, since cosmic rays interact with different media in the galaxy, a multidisciplinary approach should be taken to provide a satisfactory description. In the next section, we will analyze the map of how particles arrive at the Earth. The following sections will explore the different components that can affect cosmic rays and help us build a comprehensive picture of the observations.

7.3 Cosmic Ray Anisotropy

When Galactic cosmic rays arrive on Earth, they do so in a non-uniform manner. Figure 7.5 shows a sky map of the arrival directions distribution of CRs. In this map, the red color

indicates areas in the sky where more CRs pass through. On the other hand, the blue color denotes fewer CRs from those directions. If particles came in equal numbers from all the different directions in the sky, this map would have been just one color. But as we can see, we have a lack of uniformity–or anisotropy–in the map; this is why this phenomenon is referred to as the *Cosmic-Ray Anisotropy.*

An exact explanation for this anisotropy still eludes us. However, it is expected that the origin is due to a synthesis of factors such as the distribution and nature of their sources, properties of the magnetic fields, and overall cosmic-ray propagation. Nonetheless, from this anisotropy, we can distill crucial information about the environment surrounding us in the Galaxy and how CRs move through it. In the next section, we will explore different explanations for this anisotropy.
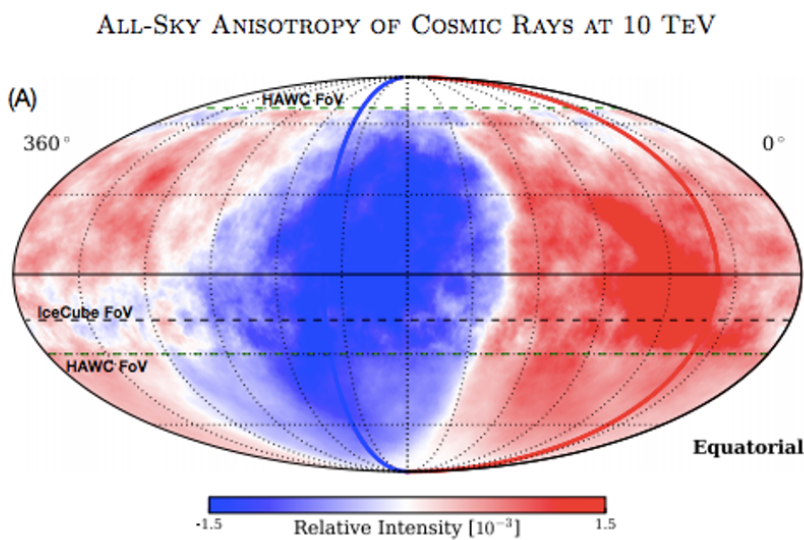

Figure 7.5: Map of the arrival directions of Cosmic Rays. Data by the High-Altitude Water Cherenkov and IceCube observatories in the northern and southern hemispheres

7.4 Effects on the Cosmic Ray Anisotropy

In this section, we will explore different effects that could cause this anisotropy. They will shine a light on specific mechanisms behind the behavior of CRs and what we can learn

about the environment that they travel through.

7.4.1 Turbulence in the Local Neighborhood

As we mentioned before, when particles travel in the Galaxy, they are affected by magnetic fields. A critical characteristic of these magnetic fields is that they are turbulent. The space in which they travel between the stars is called the interstellar medium. The magnetic fields in this environment have a very complex structure because they are turbulent. Turbulence creates chaotic eddies that tangled the magnetic field lines, much like the drawing by Leonardo da Vinci in figure 7.6 of a water jet plunging into a pool. So, the question that arose here was: can the interstellar medium imprint its structure onto the CR arrival maps? We found that through the interaction of the particles with these turbulent fields, a beautiful myriad of structures was created. This means that we can learn about our local neighborhood in the interstellar medium by looking at the directions CRs come from. These tiny particles can bring us information about structures that are one hundred trillion kilometers away.
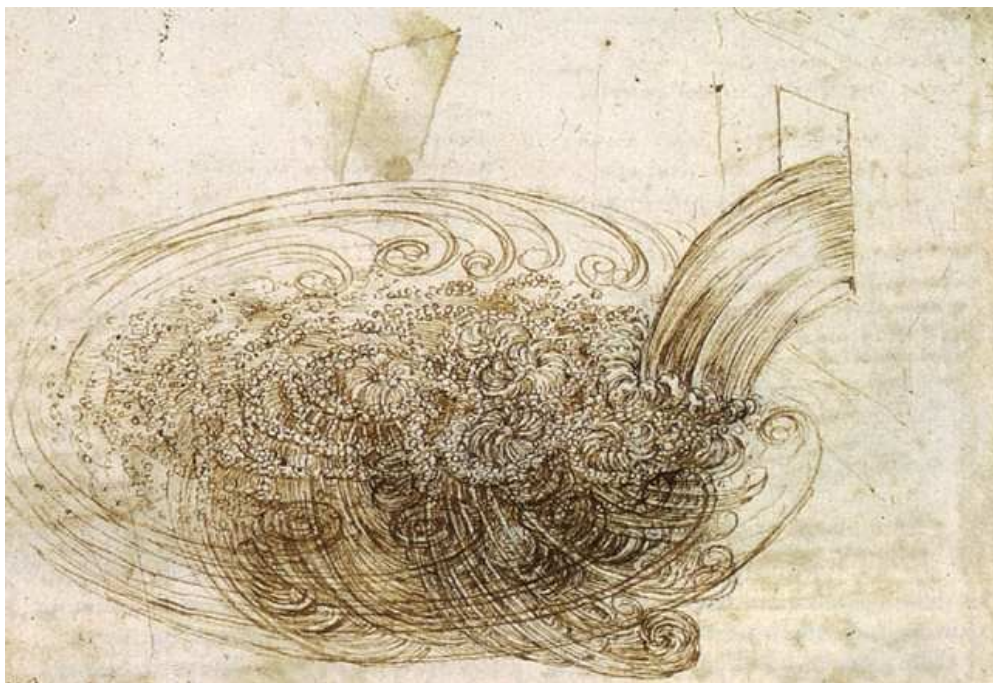

Figure 7.6: Leonardo da Vinci's sketch of a water jet plunging into a pool. showing the resultant turbulent flow. Royal Collection at Windsor (RCIN 912660v).

7.4.2 The Heliosphere

The other aspect that I explore in my dissertation is the effect of the heliosphere. The heliosphere is a cavity formed in the interstellar medium by the particles that the Sun emits. Consequently, the heliosphere distorts the interstellar medium's magnetic field. For example, suppose a particle is coming from outside the heliosphere. In that case, as it is shown in figure 7.7, it could get trapped in the heliosphere and bounce back and forth until it is detected on Earth. This trapping and bouncing of the CR can ultimately affect the original direction that the particle had outside the heliosphere. Therefore, there is a strong rearrangement of the particles' directions as they approach our detectors. From this result, we can conclude that the effects of the heliosphere are crucial when we are explaining the arrival anisotropy of CRs.

Additionally, we can use this effect to turn the problem around and ask ourselves about the heliosphere's shape. We can do this because CRs interact with it and sample its structure in the process. One issue that we have is that even though we live inside the heliosphere, we do not know its exact form or size. The only direct measurements that give us as an indication are those made by Voyager 1 and 2. These two spacecrafts sent by NASA in the 1970s are now the farthest away of any mission that humankind has sent, billions of kilometers from Earth. But they were only able to sample a tiny part of the heliosphere. This is the reason why we have to rely on these indirect cosmic ray measurements to extract information about the heliosphere's overall configuration until new missions shed light on it.

7.4.3 Chaos

Another element that can impact the arrival direction of CRs is chaos. The basic idea behind chaos is that the path that particles follow is very sensitive to the initial conditions. This means that even a tiny variation in the trajectory can have monumental effects later on. For example, we can consider the CR trajectories in figure 7.8. Imagine we have two particles in a non-chaotic environment (the left panel in the figure). Suppose they start with a small
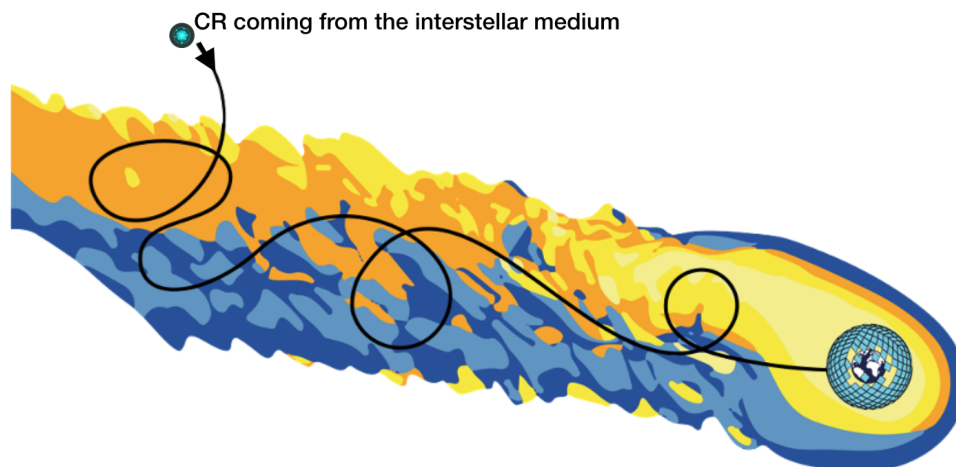
Figure 7.7: Particle interacting with the heliosphere.

separation *S1*, after some time, they will have a separation *S2* that is equal or almost the same as *S1*. So, as they move across the Galaxy, these two particles will remain close together. Contrarily, what happens if these particles travel in a chaotic medium? (The right panel in figure 7.8.) The CRs can start with the same separation *S1*, but they will begin to diverge as they propagate. At some point, the particles get extremely far apart. Therefore, the final separation *S2* can be hundreds of times greater than the initial *S1*.

So, how does chaos play a role in the context of CRs arriving on our planet? We can have two particles that seem to come from the same place in the sky, but because they are chaotic, they could come from entirely different places in the Galaxy.

7.5   Conclusions

Cosmic rays are charged particles that travel through the Universe at nearly the speed of light. They serve as cosmic messengers that transport information from far away places to the Earth. Since they are charged particles, they are affected by magnetic fields that distort their trajectories. Therefore, when they arrive on Earth, they may appear to come from one specific direction, but it does not point to their place of origin anymore. The magnetic fields
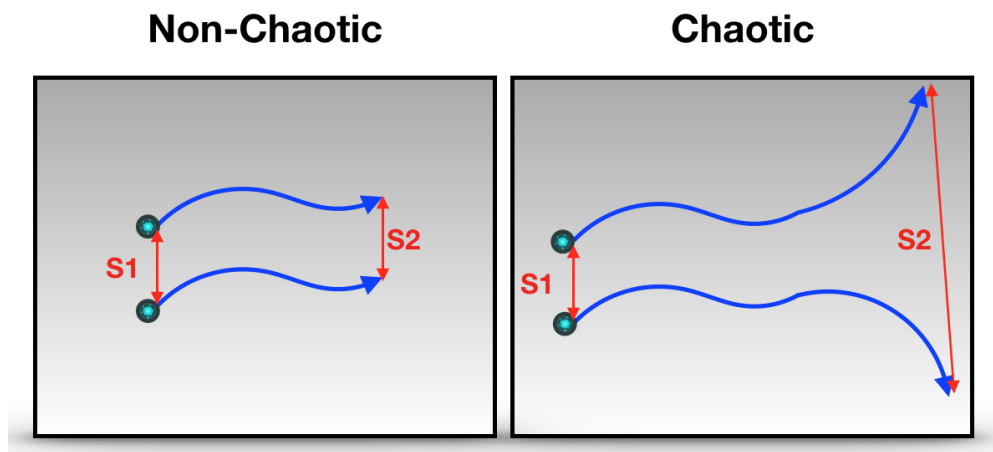
Figure 7.8: *Left:* Non-chaotic cosmic-ray trajectories. *Right*: Chaotic CR trajectories

have deflected them so much that their paths have been scrambled. This poses a difficulty when trying to explain their arrival directions.

Nonetheless, this complication is an advantage in disguise. Given that these particles have traveled the Galaxy and interacted with vastly different environments, they have collected valuable information while doing so. We can decode these messages through the directions in which the CRs are detected on Earth. For example, we can learn about the structure of our local galactic surroundings, such as the interstellar medium. Or closer to us, like the heliosphere.

At the beginning of this chapter, we imagine what it would be like to experience the Universe how a cosmic ray does. Even though humankind does not yet have the technology to travel at almost the speed of light or visit remote places in the Galaxy, it is remarkable that we can have little messengers that can teach us about what is out there. It puts us in perspective that a tiny planet like ours can decipher this information. Humans are curious by nature, so hopefully, this is just the beginning of our journey in exploring the Universe.

Appendix A

Numerical Approach and Accuracy: Particle Integration in Chapter 5

A.1   Numerical Approach and Accuracy

Particle trajectories are calculated by integrating the 6D set of equations of motion, eqs. 1 and 5.2. As stated in section 4.3.2, the integration is performed numerically using the Bulirsch-Stoer method, which is considered one of the best known integration algorithms satisfying both high accuracy and efficiency [68] and widely applied in the literature (e.g., [40] and [78]). The Bulirsch-Stoer integration algorithm, is a known method for numerical calculation of ordinary differential equation solutions, that combines the so-called Richardson extrapolation (to improve the rate of convergence of a sequence) and the modified midpoint method (which advances a vector of dependent variables y(x) from a point x to a point x + H by a sequence of n substeps each of size h). The result is that Bulirsch-Stoer algorithm provides high accuracy with relatively low computational effort. The accuracy of the algorithm is further controlled, during the numerical calculation, by monitoring the local truncation error estimated at each time step. If the relative error is larger than the relative tolerance level of 10^{-6}, the step size is adaptively reduced in order to limit the error accumulation in both momentum and spatial coordinates, across the maximum integration time used in this work (corresponding

to no more than 10,000 gyrations). Such error accumulation needs to be monitored for each specific problem in which the integration algorithm is used. In particular, the accuracy on the spatial and momentum coordinates were studied.

The performance of the Bulirsch-Stoer algorithm on the accuracy of momentum coordinates in our numerical calculation can be seen in Figure A.1, where the particle energy variation (due to loss of accuracy) from that at $t = 0$ is plotted as a function of the number of gyro-orbits $\Omega_0\,t$ (for a single particle and for the average of all particles used in our 30 PeV sample).
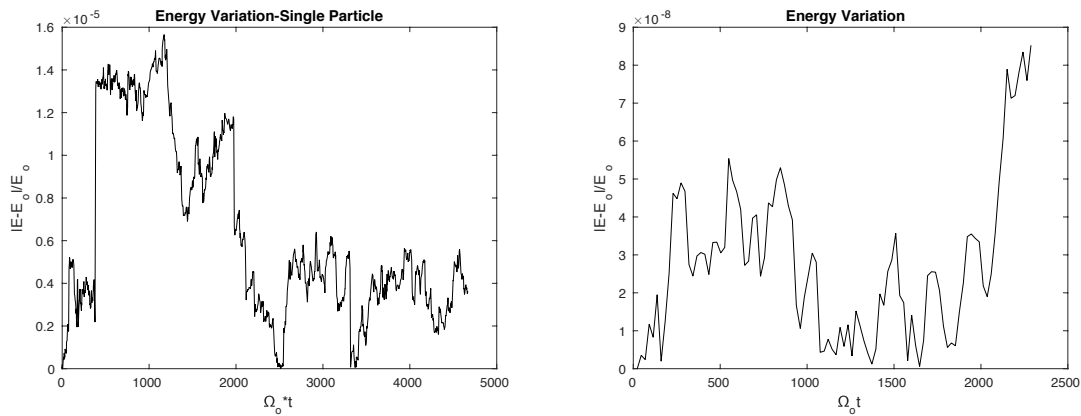

Figure A.1: Accuracy of the conservation of energy for a single particle (on the left) and for the average particle sample (on the right) of the 30 PeV set of Table 4.1.

The maximum relative mean deviation from perfect energy conservation is found to be about 8.5×10^{-8} for the sample used in this work (100,000 particles in the 30 PeV energy set), although a single particle can reach a violation at the 1.6×10^{-5} level. This precision level in the energy conservation guarantees that particle trajectories are not significantly affected by numerical accuracy limitations, which are found to be marginal under the conditions of this study.

Since the adaptive time step algorithm constrains both spatial and momentum coordinates to the same relative error level, the accuracy in spatial coordinates is $\ll r_L$, even after 10,000 gyrations. Numerical diffusion, therefore, is limited to a level much smaller than Bohm

diffusion, which is several orders of magnitude below diffusion induced by the stochastic wandering of magnetic field lines at all scales [56].

The effect on the particle set size was assessed in [78], which used the same integration stepping algorithms as in this work. In that paper, the perpendicular diffusion coefficient becomes stable when the sample size reaches about 1000 particles. The sets used in this study contain 100,000 or more particles (see Table 4.1), thus minimizing statistical accuracy effects on the global behavior of the ensemble of particles.